



Universität zu  
Köln



Forschungszentrum Jülich



Tbilisi State  
University

# Measurement of Nucleon-Nucleon Elastic Scattering at Small Angles using the ANKE spectrometer

PhD Thesis by  
[Zara Bagdasarian](#)

Supervisors: Hans Ströher (Universität zu Köln, FZJ)  
Nodar Lomidze (Tbilisi State University, HEPI)

A thesis submitted in partial fulfillment for the  
PhD Degree in Physics

under the joint supervision (Cotutelle) from University of Cologne  
and Ivane Javakhishvili Tbilisi State University

February 5, 2016



# Measurement of Nucleon-Nucleon Elastic Scattering at Small Angles using the ANKE spectrometer

Inaugural-Disseration

zur

Erlangung des Doktorgrades

der Mathematisch-Naturwissenschaftlichen Fakultät

der Universität zu Köln

(im gemeinsamen Promotionsverfahren (Cotutelle) mit der  
Staatlichen Iwane-Dschawachischwili-Universität Tiflis)

vorgelegt von

**Zara Bagdasarian**

aus Tiflis

Berichterstatter: Prof. Dr. Hans Ströher,  
Dr. Nodar Lomidze

Tag der mündlichen Prüfung: 11.04.2016

ივანე ჯავახიშვილის სახელობის  
თბილისის სახელმწიფო უნივერსიტეტი  
ზუსტ და საბუნებისმეტყველო მეცნიერებათა ფაკულტეტი  
სადოქტორო პროგრამა: “ფიზიკა”

## ზარა ბაღდასარიანი

# მცირე კუთხეებზე ნუკლონ-ნუკლონური დრეკადი გაბნევის შესწავლა ANKE სპექტრომეტრის გამოყენებით

სადოქტორო დისერტაცია შესრულებულია

ფიზიკის დოქტორის  
აკადემიური ხარისხის მოსაპოვებლად

თბილისის სახელმწიფო უნივერსიტეტს და კიოლნის უნივერსიტეტს  
(გერმანია) შორის ერთობლივი ხელმძღვანელობის (Cotutelle) შესახებ  
ხელშეკრულების ფარგლებში

დისერტაციის ხელმძღვანელები:

ჰანს შტროერი – კიოლნის უნივერსიტეტის პროფესორი,  
იულიხის კვლევითი ცენტრის ბირთვული  
ფიზიკის ინსტიტუტის დირექტორი

ნოდარ ლომიძე – ფიზიკა-მათემატიკის მეცნიერებათა დოქტორი,  
თსუ მაღალი ენერგიების ფიზიკის ინსტიტუტის  
უფროსი მეცნიერ თანამშრომელი

სადოქტრო პროგრამის ხელმძღვანელები:

მერაბ ელიაშვილი

მირიან ტაბიძე

## *Abstract*

A fundamental understanding of the nucleon-nucleon interaction (NN) is one of the ultimate goals of nuclear and hadron physics. Apart from its intrinsic importance for the study of nuclear forces, NN elastic scattering data is necessary, for example, in the modeling of meson production and other nuclear reactions at intermediate energies.

Quantum chromodynamics, the theory of strong interactions, is not able to determine the NN interaction from first principles because of the non-perturbative nature at intermediate energies (coupling constant is too strong). Hence, the phenomenological approaches are necessary to describe the NN interaction. The partial wave analyses (PWA), e.g. the ones regularly performed by the SAID group, have proved to be truly invaluable tools over many years for researchers in this area. Such an analysis relies on the quantity and quality of the experimental measurements of various proton-proton ( $pp$ ) and proton-neutron ( $pn$ ) scattering observables at different energies over the full angular range.

The goal of many experiments conducted at Cooler Synchrotron (COSY) has been to provide PWA with the essential precision measurements of NN observables. The experiments, presented in this thesis, have been carried out within the ANKE collaboration at COSY-Jülich, Germany. Data was obtained using polarised or unpolarised proton beam and unpolarised hydrogen or deuterium cluster-jet targets. The ANKE spectrometer detection system is the ideal set-up for the precise measurements at small scattering angles that had not been priorly investigated.

The thesis comprises the measurements of the analysing power  $A_y$  and differential cross section  $d\sigma/d\Omega$  in the  $pp$  elastic scattering, and preliminary results for the analysing power  $A_y$  in the  $pn$  quasi-free elastic scattering. These new precision data close an important gap in the NN database at small scattering angles up to  $30^\circ$  and energies up to 2.8 GeV.

The obtained results are compared to the predictions from the SAID PWA published in 2007 that are based on data from the previous experiments. The impact of the present results is demonstrated by the significant changes in the low partial waves of the updated SAID PWA, which includes the global data along with the new ANKE measurements.



## *Zusammenfassung*



## ანოტაცია

ნუკლონ-ნუკლონური (NN) ურთიერთქმედების ფუნდამენტური შესწავლა არის ბირთვული და ადრონული ფიზიკის ერთერთი მთავარი ამოცანა. ბირთვული ძალების შესწავლის თავისთავადი მნიშვნელობის გარდა, NN დრეკადი გაბნევის მახასიათებლების ცოდნა აუცილებელია, მაგალითად, მეზონების დაბადების და სხვა ბირთვული რეაქციების მოდელირებისთვის შუალედურ ენერგიებზე.

ძლიერი ურთიერთქმედების თეორია - კვანტური ქრომოდინამიკა ძირითად პრინციპებზე დაყრდნობით ვერ აღწერს NN ურთიერთქმედებას შუალედურ ენერგიებზე, რადგან ბმის მუდმივის დიდი მნიშვნელობის გამო შეუძლებელია შეშფოთების თეორიის გამოყენება. ამიტომ, NN ურთიერთქმედება ასეთ ენერგიებზე უნდა აღიწეროს ფენომენოლოგიური მიდგომით, კერძოდ, პროტონ-პროტონული (pp) და პროტონ-ნეიტრონული (pn) გაბნევის ამპლიტუდების პარციალურ ტალღებად გაშლის (ე.წ. ურთიერთქმედების ფაზური ანალიზის - PWA) საშუალებით. SAID (Scattering Analysis Interactive Dialin) მონაცემთა ბაზა და ანალიზი წარმოადგენს ენერჯის ამ არეში ყველაზე სანდო ინფორმაციულ წყაროს, რომელიც იქმნებოდა ბოლო რამდენიმე ათეული წლის განმავლობაში. იგი დაფუძნებულია დღემდე არსებული pp და pn გაბნევის სხვადასხვა დამზერადი სიდიდეების ექსპერიმენტების მონაცემებზე, სრულ კუთხურ ინტერვალში, სხვადასხვა შუალედურ ენერგიებზე.

COSY ამაჩქარებელზე ჩატარებული მრავალი ექსპერიმენტის მიზანს წარმოადგენდა მაღალი სიზუსტის ექსპერიმენტული მონაცემების შეგროვება PWA ანალიზისათვის. დისერტაციაში წარმოდგენილი ექსპერიმენტები ჩატარდა ANKE კოლაბორაციის მიერ არაპოლარიზებული ან პოლარიზებული პროტონული ნაკადისა და არაპოლარიზებული წყალბადის ან დეიტერიუმის ჰავლური სამიზნის გამოყენებით. ANKE სპექტრომეტრის დეტექტორების სისტემა არის იდეალური დანადგარი გაბნევის მცირე კუთხეების არეში დამზერადი სიდიდეების გაზომვებისთვის, სადაც დღემდე არ არსებობდა ექსპერიმენტული მონაცემები.

დისერტაციაში მოყვანილია pp დრეკადი გაბნევის რეაქციის ანალიზური უნარისა და დიფერენციალური კვეთის, pn კვაზიდრეკადი გაბნევის რეაქციის ანალიზური უნარის ექსპერიმენტული გაზომვის შედეგები. მიღებული შედეგები მნიშვნელოვნად ავსებენ NN მონაცემთა ბაზას გაბნევის მცირე ( $30^\circ$ -მდე) კუთხეებსა და 2.8 GeV-მდე ენერჯის ინტერვალში.

დისერტაციაში მიღებული შედეგები შედარებულია SAID ანალიზის შედეგებთან, რომლებიც მიღებულნი იყვნენ 2007 წლამდე არსებულ ექსპერიმენტულ მონაცემებზე დაყრდნობით. ნაჩვენებია, აგრეთვე, ის ცვლილებები, რომლებიც SAID ანალიზზე მოახდინეს ANKE კოლაბორაციის შედეგებმა დაბალი პარციალური ტალღების არეში.



## *Acknowledgements*

*To my wonderful parents,  
Luiza and Amik*





# Contents

<b>Abstract</b>	<b>vii</b>
<b>Zusammenfassung</b>	<b>ix</b>
<b>Acknowledgements</b>	<b>xiii</b>
<b>Contents</b>	<b>xvi</b>
<b>Abbreviations</b>	<b>xxi</b>
<b>1 Introduction</b>	<b>1</b>
1.1 The structure of matter . . . . .	1
1.1.1 The structure of the nucleon: historical overview . . . . .	2
1.2 Nucleon-nucleon scattering . . . . .	4
1.2.1 EDDA’s legacy . . . . .	4
1.3 Synopsis of the thesis work . . . . .	5
<b>2 Formalism in polarised experiments</b>	<b>7</b>
2.1 Polarisation formalism . . . . .	7
2.1.1 Spin structure $1/2 + 1/2 \rightarrow 1/2 + 1/2$ . . . . .	8
2.1.2 Coordinate system . . . . .	9
2.2 Spin observables . . . . .	10
2.3 Cross-ratio method . . . . .	11
<b>3 Experimental Setup</b>	<b>15</b>
3.1 COSY facility . . . . .	15
3.1.1 Polarised ion source at COSY . . . . .	17
3.1.2 Depolarising resonances at COSY . . . . .	18
3.2 EDDA polarimeter . . . . .	20
3.3 ANKE spectrometer . . . . .	21
3.3.1 Unpolarised cluster-jet target . . . . .	22
3.3.2 Forward Detector . . . . .	24
3.3.3 Silicon Tracking Telescopes . . . . .	25
3.4 Experimental conditions . . . . .	26

<b>4</b>	<b>Analysing power in proton-proton elastic scattering</b>	<b>29</b>
4.1	Beam polarisation measurement using EDDA . . . . .	29
4.1.1	Beam polarisation uncertainty . . . . .	31
4.2	Asymmetry measurement using ANKE . . . . .	32
4.2.1	Event selection by STT . . . . .	32
4.2.2	Asymmetry measurement using STT . . . . .	34
4.2.3	Event selection by FD . . . . .	35
4.2.4	Asymmetry measurement using FD . . . . .	36
4.2.5	Sources of the systematic uncertainties . . . . .	37
4.2.5.1	Difference in polarisation values for two polarisation modes . . . . .	38
4.2.5.2	Polar angle . . . . .	38
4.2.5.3	Detector efficiencies stability . . . . .	39
4.2.5.4	Summary on systematic uncertainties . . . . .	41
4.3	Results and discussion . . . . .	42
4.4	Conclusion . . . . .	44
<b>5</b>	<b>Cross section in proton-proton elastic scattering</b>	<b>45</b>
5.1	Luminosity determination . . . . .	46
5.1.1	Beam intensity measurement . . . . .	46
5.1.2	Target density determination . . . . .	48
5.1.2.1	Schottky noise . . . . .	49
5.1.2.2	Frequency shift . . . . .	50
5.1.2.3	Background correction . . . . .	51
5.1.2.4	Momentum compaction factor . . . . .	53
5.1.2.5	Luminosity values . . . . .	53
5.2	Event selection by FD . . . . .	54
5.3	Systematic uncertainties . . . . .	55
5.4	Results and discussion . . . . .	55
5.4.1	Comparison with LNPI results at 1 GeV . . . . .	57
5.4.2	Comparison with ANL results at 2.0 and 2.8 GeV . . . . .	57
5.4.3	Impact on the SAID solution . . . . .	58
5.5	Conclusion . . . . .	62
<b>6</b>	<b>Analysing power in proton-neutron quasi-free elastic scattering</b>	<b>63</b>
6.1	Beam polarisation . . . . .	64
6.2	Event selection . . . . .	64
6.3	Asymmetry determination . . . . .	66
6.3.1	Normalisation via proton-deuteron elastic scattering . . . . .	67
6.4	Background correction . . . . .	69
6.5	Validity of spectator model . . . . .	71
6.5.1	Quasi-free elastic proton-proton scattering . . . . .	71
6.6	Results and Discussion . . . . .	73
6.7	Conclusion . . . . .	75

<i>Contents</i>	xix
<hr/>	
<b>7 Summary and outlook</b>	<b>77</b>
7.1 Impact on partial wave analysis . . . . .	77
<b>Appendices</b>	<b>77</b>
<b>A Angular ranges of EDDA semi-rings</b>	<b>79</b>
<b>B Numerical values of the analysing power in pp elastic scattering</b>	<b>81</b>
<b>C Numerical values of the differential cross section in pp elastic scattering</b>	<b>89</b>
<b>D Numerical values of the analysing power in pd elastic scattering</b>	<b>99</b>
<b>E Numerical values of the analysing power in pn quasi-free elastic scattering</b>	<b>103</b>
<b>List of Figures</b>	<b>105</b>
<b>List of Tables</b>	<b>109</b>
<b>Bibliography</b>	<b>113</b>
<b>Erklärung</b>	<b>125</b>
<b>Lebenslauf</b>	<b>128</b>



# Abbreviations

<b>SM</b>	<b>S</b> tandard <b>M</b> odel
<b>PSA</b>	<b>P</b> hase <b>S</b> hift <b>A</b> nalysis
<b>PWA</b>	<b>P</b> artial <b>W</b> ave <b>A</b> nalysis
<b>QCD</b>	<b>Q</b> uantum <b>C</b> hromo <b>D</b> ynamics
<b>SAID</b>	<b>S</b> cattering <b>A</b> nalysis <b>I</b> nteractive <b>D</b> ialin
<b>COSY</b>	<b>C</b> Ooler <b>S</b> Ynchrotron
<b>ANKE</b>	<b>A</b> pparatus for <b>S</b> tudies of <b>N</b> ucleon and <b>K</b> aon <b>E</b> jectiles
<b>EDDA</b>	<b>E</b> xcitation Function <b>D</b> ata <b>A</b> cquisition Designed for <b>A</b> nalysis of Phase Shifts
<b>STT</b>	<b>S</b> ilicon <b>T</b> racking <b>T</b> elescope
<b>FD</b>	<b>F</b> orward <b>D</b> etector
<b>MWPC</b>	<b>M</b> ulti <b>W</b> ire <b>P</b> roportional <b>C</b> hamber
<b>MWDC</b>	<b>M</b> ulti <b>W</b> ire <b>D</b> rift <b>C</b> hamber
<b>LEP</b>	<b>L</b> ow <b>E</b> nergy <b>P</b> olarimeter
<b>BCT</b>	<b>B</b> eam <b>C</b> urrent <b>T</b> ransformer
<b>RF</b>	<b>R</b> adio <b>F</b> requency
<b>PM</b>	<b>P</b> hoto <b>M</b> ultiplier
<b>ANL</b>	<b>A</b> rgonne <b>N</b> ational <b>L</b> aboratory
<b>LNPI</b>	<b>L</b> eningrad <b>N</b> uclear <b>P</b> hysics <b>I</b> nstitute



# Chapter 1

## Introduction

What is the matter made of? This is one of the most fundamental and ambitious questions that humankind have asked since ages. Nowadays both theoretical and experimental physicists from various fields of studies still try to tackle this questions on various scales. One of the key moments of nuclear physics was the Geiger–Marsden experiment (also known as the Rutherford gold foil experiment) that showed how profoundly our understanding of the matter can be changed via a simple scattering experiment. Since then many scattering experiments have been performed and we have learned a lot about the fundamental particles, but there are still many many questions that we need to seek answer to.

The first two sections of this chapter will provide a short overview of the structure of matter, as we understand it today, and a short historical overview of our insight into the structure of the nucleon. The following sections describe the importance of the nucleon-nucleon scattering in general and the motivation of the experimental investigations, described in this dissertation.

### 1.1 The structure of matter

Our perception of the structure of matter has changed many times during the history and most rapidly since the end of 19<sup>th</sup> century, when atoms were still thought to be the most basic, indivisible building blocks of matter, to the latter half of the 20<sup>th</sup> century, when all known subatomic particles were organised within the Standard Model (SM).

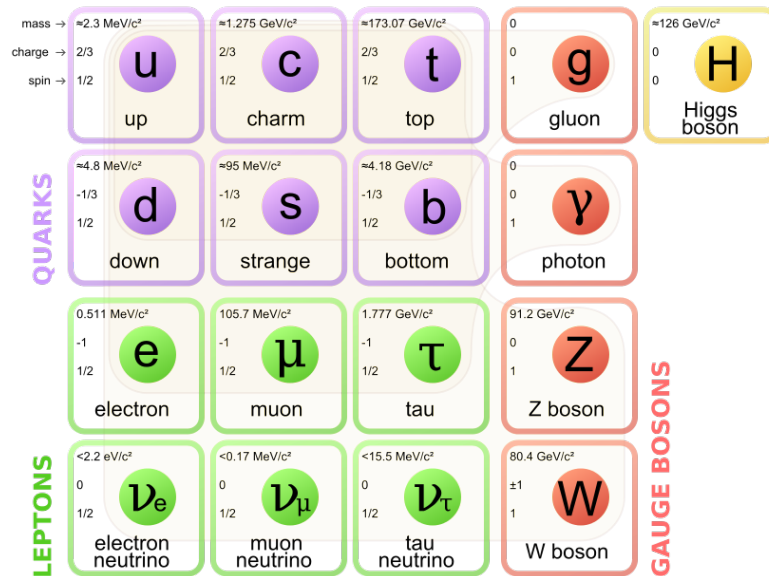


FIGURE 1.1: The Standard Model of elementary particles (more schematic depiction), with the three generations of matter, gauge bosons in the fourth column, and the Higgs boson in the fifth.

The Standard Model is the quantum field theory that describes all different kinds of interactions (except gravity, for which a quantum field theoretical description wasn't yet achieved) and classifies the elementary particles. The elementary particles constituting the ordinary matter are the fundamental fermions (half-integer spin particles), namely quarks and leptons; the gauge bosons (integer-spin particles) mediate forces, while Higgs boson is responsible for the intrinsic mass of particles.

Four fundamental forces are: the gravitational, electromagnetic, weak and strong forces. Even though weak and strong interactions are short ranged and hence were left unnoticed for a long time, nowadays we know their important role in the existence of matter. The strong interaction is responsible for holding quarks together, and consequently binding protons and neutrons into stable nuclei.

### 1.1.1 The structure of the nucleon: historical overview

Nucleons (protons and neutrons) are the lowest-energy bound states of quarks and gluons. They represent the simplest form of observable matter and comprise more than 99% of the mass of the visible universe. Most of these nucleons are in the core of atoms, the same atoms that everything we see on the daily basis is made from, including ourselves. So it comes as no surprise that nucleons have been studied with such a scrutiny during the history of science.

Rutherford has started to use the word “proton” for the hydrogen nuclei after the first reported nuclear reaction  $^{14}\text{N} + \alpha \rightarrow ^{17}\text{O} + p$  was observed and protons were identified as part of all nuclei. However, it was only after the discovery of neutron by James Chadwick in 1932 that the basic structure of nuclei and nuclear isotopes could be understood. Nevertheless the nucleons were thought to be elementary particles not for long: already in 1933 first glimpse of an internal structure of the nucleon was observed, when magnetic moments of protons and neutrons were measured. In 1964 Gell-Mann [1] and independently Zweig [2] proposed a theory that nucleons are composed of point like particles called quarks. These quarks were postulated to have spin  $-1/2$ , a fractional electric charge, and came in different types called flavours. Soon after the electron scattering experiment that showed that nucleons are indeed composed of quarks took place at the Stanford Linear Accelerator Centre (SLAC) [3, 4]. Combinations of different flavours of quarks comprise baryons (built up from three quarks) and mesons (a quark and an anti-quark). These two groups of particles are categorized as hadrons.

The concept of how quarks are bound together via the strong force to form a nucleon, called confinement, is a topic of great interest. Confinement is accounted for by introducing the concept of quarks possessing color charge. There are three different types of color: red, blue and green. The gluons also carry the color charge and therefore can interact with each other. The mathematics of color charge dictates that hadrons, composed of these color-charged quarks, are in fact colorless; that is, hadrons are in color singlet states. This effectively describes how quarks cannot be observed directly. While quarks are bound inside the nucleon, there is a possibility for them to behave like free particles. This is the concept of asymptotic freedom.

Quantum Chromodynamics (QCD), the theory of the strong interaction, is called chromodynamics since it is a field theory that describes the color interactions. QCD follows the formalism of Quantum Electrodynamics (QED), which has a coupling constant  $a$  that describes the strength of the electromagnetic interaction; in QCD, the coupling constant  $a_s$  gives the strength of the strong (color) interaction. The concept of asymptotic freedom can be described in the framework of QCD. Since the strength of the quark interactions are small at large momentum transfer, corresponding to probing the nucleon at small distance scales, this results in  $a_s$  being small. As a result, a perturbative approach can be taken in the mathematical description of the interactions, with  $a_s$  as the expansion parameter. This kinematic regime is called perturbative QCD or just pQCD, and theoretical predictions can be well tested by experiments. However at lower energies the coupling

constant becomes larger, and perturbative calculations no longer work. Therefore experimental data of high quality and precision at low and intermediate energy are necessary for the full understanding of the strong interaction.

## 1.2 Nucleon-nucleon scattering

The nucleon-nucleon (NN) interaction is the prototype for the action of the nuclear forces. Data on NN scattering are necessary ingredients, not only for the understanding of nuclear forces, but also for the description of meson production and other nuclear reactions at intermediate energies.

The scattering amplitudes for the complete description of the NN interaction can be reconstructed from the phase shift analysis (PSA). It has proved to be truly invaluable tool over many years for researchers working in this area. For an interpretation of the results obtained in this work, they will be compared to the most recently published [5] and modified calculations from the SAID (Scattering Analysis Interactive Dial-in) partial wave analysis (PWA) [6, 7]. The SAID facility is based at George Washington University, Washington DC, USA. It maintains a database which contains the world data on  $NN$  scattering among other reactions, and provides predictions from PWA of the data. Such an analysis is based on the measurement of various NN scattering observables at different energies over the full angular range.

Unpolarised experiments provide information only about the averaged spin effects. This means that a certain amount of information is being lost. Since strong interaction is spin-dependent, it is crucial to conduct polarised experiments to separate the spin-specific parts of interaction. The polarised experiments provide additional information on reaction mechanisms, indispensable for the partial wave analysis.

### 1.2.1 EDDA's legacy

It should be pointed out that the COSY-EDDA collaboration (Excitation function Data acquisition Designed for Analysis of phase shifts) have provided a perfect example how polarised data has completely revolutionised partial wave analysis.

The data on the differential cross section in  $pp$  elastic scattering [8] were taken in a continuous ramp of the proton beam energy from 0.24 to 2.58 GeV using the  $CH_2$

fibre target. Prior to the EDDA measurements, SAID solution was only valid up to 1.6 GeV. With more than 2000 points EDDA data completely dominated the SAID database above about 1 GeV.

EDDA collaboration has also made contributions in spin-dependent measurements: The data points were produced for the proton analysing power using the unpolarised beam between 0.44 and 2.49 GeV incident on a polarised hydrogen target [9, 10]. In addition,  $pp$  spin correlations were studied in the same energy range [11]. However, due to the design of the EDDA detector, the experiments only extended over the central region of centre-of-mass (c.m.) angles,  $30^\circ \lesssim \theta_{cm} \lesssim 150^\circ$ .

### 1.3 Synopsis of the thesis work

Many accelerators around the world included the NN study into their research program, however even after many years of studies, there are still many gaps in our knowledge. As one can see in the Figure 1.2, even in the data base of the most basic reaction of proton-proton elastic scattering, there has been a significant gap at the small angles ( $\theta_{cm} < 30^\circ$ ) above 1 GeV. The situation is much worse for the isoscalar  $I = 0$  case of proton-neutron scattering (Figure 1.3).

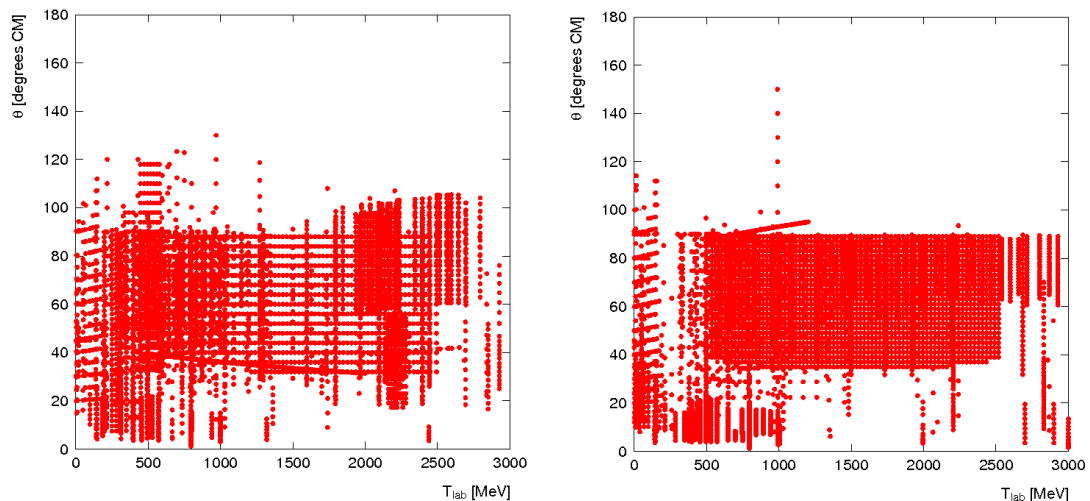


FIGURE 1.2: Abundance plots of c.m. scattering angle ( $\theta_{cm}$ ) versus beam energy ( $T_{lab}$ ) for experiments on the analyzing power  $A_y$  (left) and for cross-section  $d\sigma/d\Omega$  (right) in proton-proton elastic scattering. Source: <http://nn-online.org>.

The precision data at small angles has a potential to significantly influence PSA. Adding to the NN scattering data base was one of the major priorities of the ANKE collaboration. This thesis comprises data gathered over three ANKE experiments, dedicated to the understanding of NN scattering:

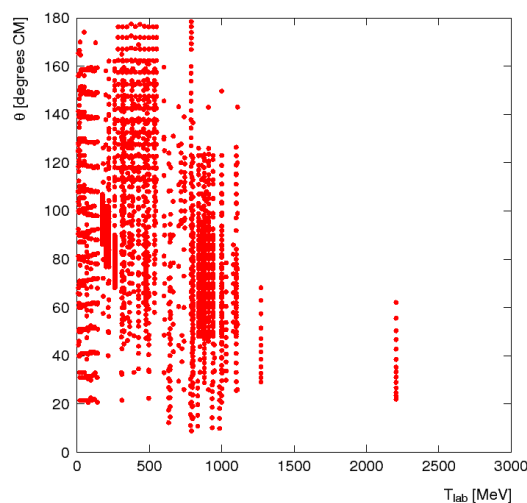


FIGURE 1.3: Abundance plot of c.m. scattering angle ( $\theta_{cm}$ ) versus beam energy ( $T_{lab}$ ) for experiments on the analysing power  $A_y$  in proton-neutron scattering. Source: <http://nn-online.org>.

- the proton-proton elastic scattering studies
  - analysing power  $A_y$  in proton-proton elastic scattering using unpolarised hydrogen cluster target and polarised proton beam at six energies between 0.796 and 2.4 GeV;
  - unpolarised differential cross sections  $d\sigma/d\Omega$  at eight beam kinetic energies between 1.0 and 2.8 GeV;
- the proton-neutron quasi-elastic scattering study
  - analysing power  $A_y$  using unpolarised deuterium cluster target and polarised proton beam at six energies between 0.796 and 2.4 GeV.

While high-quality  $pp$  data from ANKE closes a very important gap at small angles, proton-neutron ( $pn$ ) data is a crucial contribution to the very incomplete  $pn$  data base.

The rest of the thesis is outlined as follows: Chapter 2 describes the common formalism of the polarised experiments, on which the following chapters will be based. In Chapter 3 the experimental setup for the ANKE experiments is introduced. The Chapter 4 gives a detailed description of the data analysis and obtained results for the analysing power in  $\vec{p}p$  elastic scattering. The Chapter 5 concentrates on the specifics of the cross section measurements in  $pp$  elastic scattering. Chapter 6 presents the data analysis performed on proton-neutron quasi elastic scattering and preliminary results. The concluding remarks are presented in Chapter 7.

## Chapter 2

# Formalism in polarised experiments

In this chapter a short overview of the formalism necessary to investigate the spin-specific parts of NN interaction is given. Namely, important aspects of polarised experiments necessary to extract the spin observables, and method reducing the systematic errors. Within this thesis, only interactions of 1/2 spin particles are studied, hence only this simple case of 1/2 spin particle scattering is described in the following.

### 2.1 Polarisation formalism

Quantum mechanics deals with statistical statements about the result of measurements on an ensemble of states (particles, beams, targets). In other words: by giving an expectation value of operators it provides probability amplitudes for the result of a measurement on an ensemble.

There are two limiting cases. One is the pure state, that is our knowledge of the system is complete, e.g. when all members of an ensemble are in the same spin state. A special case is the spin state of a single particle, which is always completely polarised. In general, our knowledge of a system is incomplete and can only be described by superposition of such pure states, weighted with the probability of their occurrence in this superposition. Such a state is called a mixed state. The appropriate and also practical description of such states is by using the density operator  $\rho$ :

$$\rho = \sum_i p_i |\psi^i\rangle \langle \psi^i|, \quad (2.1)$$

where  $p_i$  is the probability of finding the ensemble in a quantum mechanical state characterised by  $|\psi^i\rangle$ . A pure state is represented by the density matrix:

$$\rho = \begin{pmatrix} 1 & 0 \\ 0 & 0 \end{pmatrix}. \quad (2.2)$$

A completely unpolarised beam with all spin substates equally occupied has the density matrix

$$\rho = 1/2 \begin{pmatrix} 1 & 0 \\ 0 & 1 \end{pmatrix} = 1/2 \left[ \begin{pmatrix} 1 & 0 \\ 0 & 0 \end{pmatrix} + \begin{pmatrix} 0 & 0 \\ 0 & 1 \end{pmatrix} \right]. \quad (2.3)$$

This corresponds to superposition of pure states with equal weights of 1/2. A general beam can be interpreted as a superposition of the two pure states defined with respect to the quantization axis with the contributions  $N_+$  and  $N_-$ :

$$\rho = N_+ \begin{pmatrix} 1 & 0 \\ 0 & 0 \end{pmatrix} + N_- \begin{pmatrix} 0 & 0 \\ 0 & 1 \end{pmatrix} = \begin{pmatrix} N_+ & 0 \\ 0 & N_- \end{pmatrix}. \quad (2.4)$$

The vector polarisation of a spin 1/2 system has form:

$$P = \frac{N_+ - N_-}{N_+ + N_-}. \quad (2.5)$$

### 2.1.1 Spin structure $1/2 + 1/2 \rightarrow 1/2 + 1/2$

Formalism of elastic scattering of the systems with spin structure  $1/2 + 1/2 \rightarrow 1/2 + 1/2$ , including the NN scattering, is described in detail in References [12] and [13]. In principle, there are 255 possible polarisation observables for this spin system + unpolarised differential cross section. However, for elastic scattering, parity conservation and time-reversal invariance will reduce this number to 25 for identical particles, for example  $pp$  scattering, and to 36 linearly independent experiments for non-identical particles, such as  $pn$  scattering. Nucleon-nucleon scattering matrix  $M$  is presented as

$$M(k_f, k_i) = \frac{1}{2} \{ (a + b) + (a - b)(\sigma_1, \mathbf{n})(\sigma_2, \mathbf{n}) + (c + d)(\sigma_1, \mathbf{m})(\sigma_2, \mathbf{m}) + (c - d)(\sigma_1, \mathbf{l})(\sigma_2, \mathbf{l}) + \mathbf{e}(\sigma_1 + \sigma_2, \mathbf{n}) \}, \quad (2.6)$$

here the amplitudes  $a, b, c, d,$  and  $e$  are complex functions of two variables: energy in c.m. and the scattering angle.  $\mathbf{l}, \mathbf{m},$  and  $\mathbf{n}$  are the c.m. basis vectors:

$$\mathbf{l} = \frac{\mathbf{k}_f + \mathbf{k}_i}{|\mathbf{k}_f + \mathbf{k}_i|}, \mathbf{m} = \frac{\mathbf{k}_f - \mathbf{k}_i}{|\mathbf{k}_f - \mathbf{k}_i|}, \mathbf{n} = \frac{\mathbf{k}_f \times \mathbf{k}_i}{|\mathbf{k}_f \times \mathbf{k}_i|}. \quad (2.7)$$

whereas  $\sigma_1$  and  $\sigma_2$  are Pauli matrices. In  $pp$  scattering, after considering parity conservation, time-reversal invariance and the Pauli principle there are  $N = 5,$  in  $np$  scattering  $N = 6$  invariant, independent complex amplitudes. Thus in a complete experiment  $2N - 1$  real quantities have to be measured by at least as many independent experiments: 9 for  $pp$  and 11 for  $np$  [14].

### 2.1.2 Coordinate system

For polarised experiments the appropriate definition of coordinate system is very important. In unpolarised reactions incoming and outgoing particle momenta define the scattering plane. A polarisation vector adds another direction thus introducing an azimuthal dependence of observables. Cartesian coordinate system is formed with  $z$  along the incident beam momentum  $\mathbf{k}_i,$   $y$  along  $\mathbf{k}_i \times \mathbf{k}_f$  where  $\mathbf{k}_f$  is scattered particle momentum, and  $x$  such as to define a right-handed coordinate system. Let's define  $\mathbf{i}, \mathbf{j}$  and  $\mathbf{k}$  unit vectors pointing along the  $x, y$  and  $z$  coordinate axes respectively. So,  $\mathbf{k} = \mathbf{k}_i/k_i, \mathbf{j} \parallel (\mathbf{k}_i \times \mathbf{k}_f),$  and  $\mathbf{i} \parallel (\mathbf{k} \times \mathbf{j}).$  The unit vector pointing along the spin quantization axis is denoted by  $\mathbf{s};$  its direction is defined in terms of  $\beta,$  the angle between  $\mathbf{s}$  and beam direction, and  $\phi,$  the angle between its projection on  $xy$  plane and  $y$  axis.

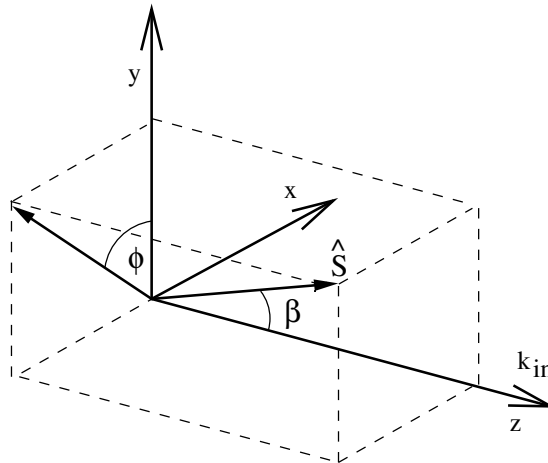


FIGURE 2.1: Madison convention for the definition of the laboratory-coordinate system. The  $z$  axis is along the incident beam momentum. The scattering is in the  $xz$  plane.

In this system, the scattering is always in the  $xz$  plane, and the momentum vector of the scattered particle lies in the  $xz$  half-plane with positive  $x$ . The direction, called “up” is defined by the transverse component of spin quantization axis.  $\mathbf{s}_\perp = \mathbf{s} - (\mathbf{s} \cdot \mathbf{k})\mathbf{k}$ . Hence according to an observer who is looking along the beam direction and is aligned with “up” direction, the scattering (positive  $x$  half-plane of  $xz$  plane) is to the left, if  $y$  axis is along  $\mathbf{s}_\perp$  ( $\phi = 0^\circ$ ). Correspondingly if  $\phi = 180^\circ$ ,  $\phi = 270^\circ$  and  $\phi = 90^\circ$ , then the scattering is to the right, up and down, respectively.

## 2.2 Spin observables

Although the spin observables depend only on a polar angle, the cross section including these observable generally exhibit a dependence on the azimuthal angle. This dependence enters via the need to introduce coordinate systems in which the detector positions, as well as the polarisation direction have to be described. The cross section for a polarised beam of spin 1/2 particles is

$$\sigma(\theta, \phi) = \sigma_0(\theta)[1 + P_y A_y(\theta)], \quad (2.8)$$

where  $\sigma_0(\theta)$  is the cross section for the scattering of an unpolarised beam at the scattering angle  $\theta$ ,  $A_y(\theta)$  is the analysing power of the reaction at the same angle and  $P_y$  is the  $y$  component of the beam polarisation.

$$P_y = \mathbf{P} \cdot \mathbf{j} \equiv \mathbf{P} \sin \beta \cos \phi \equiv \mathbf{P}_\perp \cos \phi, \quad (2.9)$$

where  $\mathbf{P}$  is the beam polarisation,  $\mathbf{j}$  is unit vector along the  $y$  axis, and  $P_\perp$  is the component of beam polarisation perpendicular to its direction of motion. Since in our experiment we have transversely polarised beam, we assume  $\beta \approx 90^\circ$ . Hence the difference between  $P_\perp$  and  $P$  is neglected, and we set  $P_\perp \equiv P$ .

The Madison Convention implies that for spin 1/2 particles the polarisation should be counted positive in the direction  $(\mathbf{k}_i \times \mathbf{k}_f)$ . Assuming a positive analysing power, this positive polarisation yields a positive left-right (L-R) asymmetry.

### 2.3 Cross-ratio method

Many sources of systematic uncertainties in the determination of analysing power  $A_y$  can be neglected in the first order in case of left-right symmetrical arrangement of the detection system. Let us consider symmetric two detector system. The actual number of counts recorded in a detector is

$$N(\theta, \phi) = nN_t\Omega E\sigma(\theta, \phi), \quad (2.10)$$

where  $n$  is the number of particles, incident on the target,  $N_t$  is the number of target nuclei per cubic centimetre,  $\Omega$  is a geometrical factor, defined by the detector, i.e. the solid angle subtended by the detector, and  $E$  is the detector efficiency. It is allowed, that solid angle factor as well as its efficiency of detector 1 to be different from those of detector 2. Therefore, Equation 2.10 for each detector will look like

$$N_1(\theta, \phi) = nN_t\Omega_1 E_1\sigma_0(\theta)[1 + P_y A_y(\theta)\cos\phi], \quad (2.11)$$

$$N_2(\theta, \phi) = nN_t\Omega_2 E_2\sigma_0(\theta)[1 + P_y A_y(\theta)\cos\phi]. \quad (2.12)$$

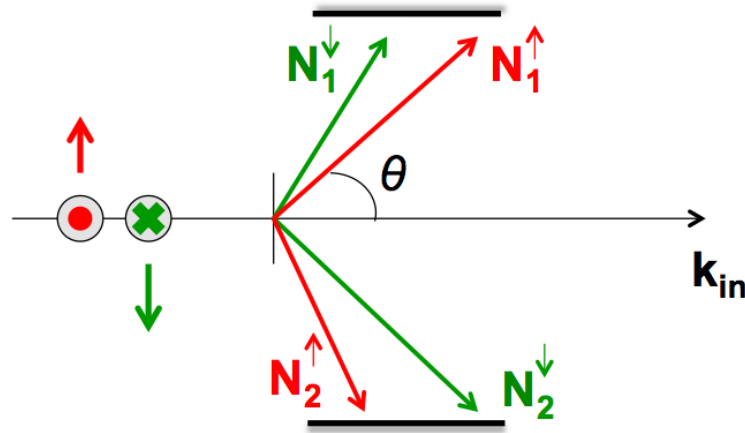


FIGURE 2.2: Two-detector idealistic symmetric arrangement

On Figure 2.2 beam polarisation direction "up" is depicted coming out of paper in red. In this case, detector 1 detects particles, that are scattered to the "left" ( $\phi = 0^\circ$ ) and detector 2 gets particles that are scattered to the "right" ( $\phi = 180^\circ$ ). Therefore,

$$N_1(\theta, 0) \equiv N_1^\uparrow \equiv L_1 = nN_t\Omega_1 E_1\sigma_0(\theta)[1 + P_y A_y(\theta)], \quad (2.13)$$

$$N_2(\theta, \pi) \equiv N_2^\uparrow \equiv R_2 = nN_t\Omega_2 E_2\sigma_0(\theta)[1 - P_y A_y(\theta)]. \quad (2.14)$$

If we now “flip” the polarisation  $\mathbf{P} \rightarrow -\mathbf{P}$ , spin direction will be going into the paper (depicted in green). This is referred to as beam polarisation “down”, and in this case detector 1 will be on the right and detector 2 on the left side.

$$N_1(\theta, \pi) \equiv N_1^\downarrow \equiv R_1 = n'N'_t\Omega_1E_1\sigma_0(\theta)[1 - P_yA_y(\theta)], \quad (2.15)$$

$$N_2(\theta, 0) \equiv N_2^\downarrow \equiv L_2 = n'N'_t\Omega_1E_2\sigma_0(\theta)[1 + P_yA_y(\theta)]. \quad (2.16)$$

Primes are used to indicate that the integrated charge and the effective target thickness may be not the same for the two runs. We can form geometrical means of number of particles scattered to the left  $L \equiv \sqrt{L_1L_2}$  and particles scattered to the right  $R \equiv \sqrt{R_1R_2}$ .

$$L = [nn'NN'\Omega_1\Omega_2E_1E_2]^{\frac{1}{2}}\sigma_0[1 + PA_y(\theta)], \quad (2.17)$$

$$R = [nn'NN'\Omega_1\Omega_2E_1E_2]^{\frac{1}{2}}\sigma_0[1 - PA_y(\theta)]. \quad (2.18)$$

We can solve for  $PA_y(\theta)$  and get left-right assymetry  $\varepsilon$

$$\varepsilon = \frac{L - R}{L + R} = \frac{2PA_y[nn'NN'\Omega_1\Omega_2E_1E_2]^{\frac{1}{2}}\sigma_0}{2[nn'NN'\Omega_1\Omega_2E_1E_2]^{\frac{1}{2}}\sigma_0} = PA_y(\theta), \quad (2.19)$$

which is independent of relative detector efficiencies ( $E_1, E_2$ ), solid angles ( $\Omega_1, \Omega_2$ ), relative integrated charge ( $nn'$ ) and target thickness variations. ( $NN'$ ).  $n$  and  $N$ , quantities common to the two channels, can be averaged over the data acquisition time (in one run)  $E$  and  $\Omega$ , quantities different in two channels, must not vary with time. We can define the geometric mean of the number of particles detected by detector 1 in two runs as  $N_1$

$$N_1 \equiv \sqrt{L_1R_1} = \Omega_1E_1\sigma_0(\theta)NN'nn'[1 - (PA_y)^2]^{\frac{1}{2}}, \quad (2.20)$$

and for particles detected by detector 2 we have

$$N_2 \equiv \sqrt{L_2R_2} = \Omega_2E_2\sigma_0(\theta)NN'nn'[1 - (PA_y)^2]^{\frac{1}{2}}. \quad (2.21)$$

Monitoring on the ratio

$$\frac{N_1}{N_2} = \frac{\Omega_1E_1}{\Omega_2E_2} \quad (2.22)$$

provides the check on the performance of the apparatus; this variable is required to be constant in time if the assymetry determination is to be accurate. The statistical error associated with a measurement of the assymetry  $\varepsilon$  is given by

means of geometrical means  $L$  and  $R$ :

$$\delta\varepsilon = \sqrt{\frac{1 - \varepsilon^2}{L + R}}. \quad (2.23)$$



## Chapter 3

# Experimental Setup

All the results presented in this thesis, have been obtained using the data gathered at the ANKE spectrometer at COSY-Jülich. COSY facility with the polarised ion source are introduced in the Sections 3.1 and 3.1.1. Even though the COSY facility includes many experimental possibilities, this chapter includes the description of only those experimental equipments that have been actively used in the described experiments. Namely, the EDDA polarimeter and ANKE spectrometer are discussed in 3.2 and 3.3 respectively. Finally, an overview of the different experimental conditions, under which the present data have been acquired, is given in Section 3.4.

### 3.1 COSY facility

The COSY accelerator and storage ring (COoler SYnchrotron), shown schematically in Figure 3.1, serves the quests of the fundamental research in the Institute of Nuclear Physics of Jülich research centre (Forschungszentrum Jülich). The acceleration process of the COSY beam consists of several stages. Negative ion sources can produce unpolarised and polarised hydrogen and deuterium ions, which are then accelerated by JULIC cyclotron up to 300 MeV/ $c$  for  $H^-$  and up to 600 MeV/ $c$  for  $D^-$ . These pre-accelerated ions are stripped off their electrons and the remaining protons or deuterons are injected in COSY ring with 183.4 m circumference, here particles can be accelerated and stored at any momentum in the range from 300 MeV/ $c$  to 3.65 GeV/ $c$  [15].

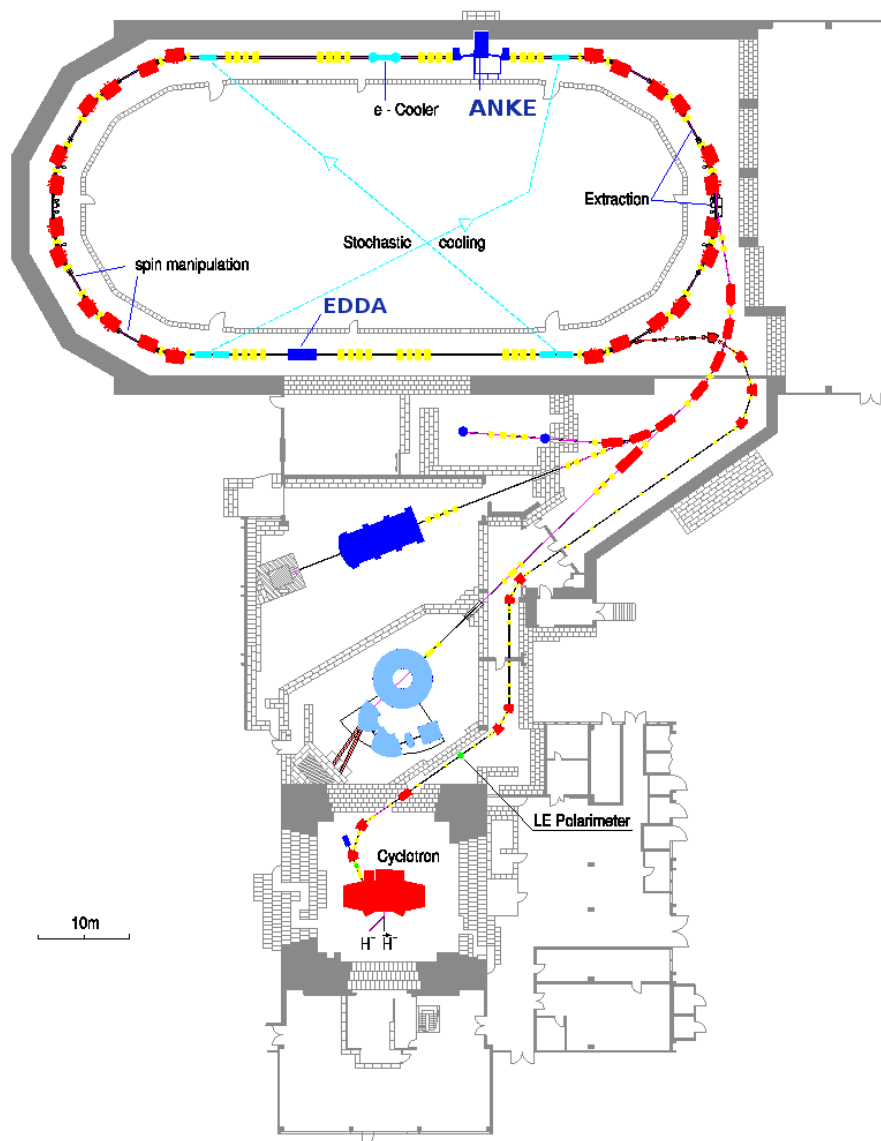


FIGURE 3.1: The COSY accelerator facility. The positions of the ANKE spectrometer and the EDDA polarimeter are shown.

Transversely polarised proton beams are available with intensities up to  $1 \cdot 10^{10}$  particles with a polarisation up to 70%. For deuterons an intensity of  $3 \cdot 10^{10}$  with vector and tensor polarisation of more than 70% and 50% were achieved respectively. The two 40 m long straight sections are designed to serve the internal experiments. Figure 3.1 demonstrates the COSY accelerator facility with the positions of the ANKE spectrometer and the EDDA polarimeter.

### 3.1.1 Polarised ion source at COSY

The polarised ion source at COSY consists of three groups of components: the pulsed atomic beam source, the caesium beam source, and the charge-exchange and extraction region. The schematic layout of the set-up is shown in Figure 3.2 [16]. The use of atomic hydrogen allows one to take advantage of the large magnetic moment of the electron. The nuclear spin, in turn, is affected by its coupling to the electron.

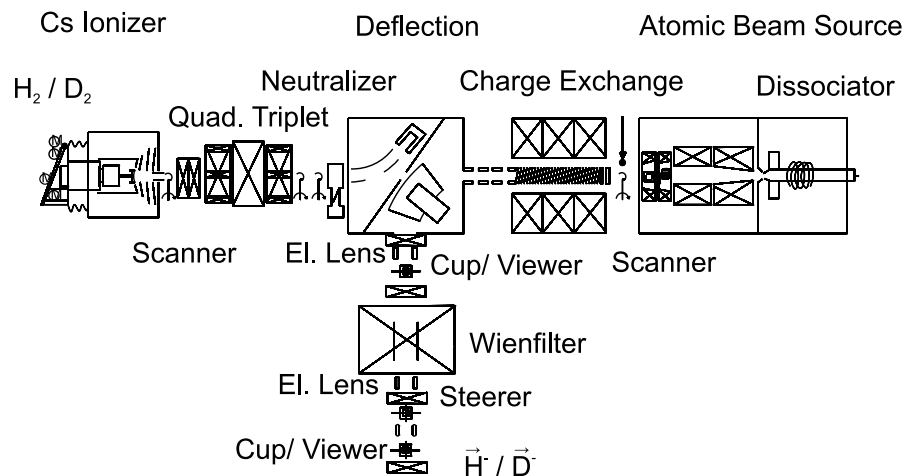


FIGURE 3.2: Set-up of the polarised ion source at COSY.

The neutral polarised hydrogen  $H^0$  beam is produced in the atomic beam source, consisting of RF dissociator and a sextupole separation magnet. First, the gas molecules are dissociated in a RF discharge (300-400 W) and a high degree of dissociation is maintained by adding small amounts of nitrogen and oxygen that reduces surface and volume recombination. The atoms are cooled to about 30 K by passing through an aluminium nozzle of 20 mm length and 3 mm diameter. By slowing down the atoms, the acceptance of the hexapole system and dwell time in the charge-exchange are increased. The first sextupole magnet produces electron state polarisation by defocusing atoms with the electron spin state  $m_j = -1/2$ . Remaining beam of atoms with  $m_j = +1/2$  is then focused by the second sextupole magnet. The nuclear polarisation is provided by two RF transitions switching between the hyperfine substates of the hydrogen atoms.

Afterwards, the atomic  $\vec{H}^0$  beam with now high nuclear polarisation collides with the fast neutral caesium (Cs) beam. Thanks to the significantly higher electro-negativity, a hydrogen atom acquires an additional electron from a caesium atom,

and becomes negatively charged [16].



The fast  $Cs^0$  beam, needed for the abovementioned reaction, is produced in two steps. First, Cs vapor is thermally ionized on a hot ( $1200^\circ$ ) porous tungsten surface at an appropriate beam potential of about 40-60 kV, where the cross section for the charge-exchange reaction has its maximum. Second, the beam is focused by a quadropole triplet to a neutraliser that consists of caesium oven, a cell filled with caesium vapour, and a magnetically driven flapper valve between the oven and the cell. The remaining  $Cs^+$  beam is deflected in front of the solenoid into a Faraday cup, while the fast neutralised caesium atoms enter the charge-exchange region. A neutraliser efficiency is typically over 90%.

In the charge exchange region the nuclear polarisation is preserved by the longitudinal magnetic field. A small electrostatic gradient field guides the very slow  $H^-$  ions to the extraction orifice, where they are deflected by a  $90^\circ$  electrostatic toroidal deflector into the injection beamline of the cyclotron. In the final stage, a Wien filter separates the  $H^-$  ions from electrons and other background. The Wien filter is rotatable around the beam axis, providing any orientation of the polarisation vector. In order to avoid the polarisation loss during the acceleration, spin orientation parallel to that of cyclotron magnetic field is chosen.

### 3.1.2 Depolarising resonances at COSY

This section is dedicated to the description of the difficulties in the acceleration of the polarised proton beam. For an ideal planar closed-loop accelerator with a vertical guide field, the particle spin vector precesses around the vertical axis. In this way the vertical beam polarisation is preserved. The spin motion in an external electromagnetic field is governed by the Thomas-BMT equation, leading to a spin tune  $\nu_{sp} = \gamma G$ , which describes the number of spin precessions of the central beam per revolution in the ring.  $G$  is the anomalous magnetic moment of the particle ( $G = 1.7928$  for protons,  $-0.1423$  for deuterons), and  $\gamma = E/m$  is the Lorentz factor. During the acceleration of a vertically polarised beam, depolarising resonances are crossed if the precession frequency of the spin  $\gamma G$  is equal to the frequency of the encountered spin-perturbing magnetic fields. In a strong-focusing synchrotron like COSY, two different types of strong depolarising resonances are

excited, namely imperfection resonances caused by magnetic field errors and misalignments of the magnets, and intrinsic resonances excited by horizontal fields due to the vertical focusing.

In the momentum range of COSY, five imperfection resonances have to be crossed for protons. The existing correction dipoles of COSY are utilised to overcome all imperfection resonances by exciting adiabatic spin flips without polarisation losses. The number of intrinsic resonances depends on the superperiodicity of the lattice. The magnetic structure of COSY allows one to choose a superperiodicity of  $P = 2$  or  $6$ . A tune-jump system consisting of two fast quadrupoles has been developed especially to handle intrinsic resonances at COSY.

The imperfection resonances for protons in the momentum range of COSY are listed in Table 3.1. They are crossed during acceleration, if the number of spin precessions per revolution of the particles in the ring is an integer ( $\gamma G = k, k$  is integer). The resonance strength depends on the vertical closed orbit deviation.

$\gamma G$	$T_p$ GeV	$p$ GeV/ $c$	$y_{co}^{rms}$ mm	$\epsilon_r$ $10^{-3}$	$P_f/P_i$
2	0.1084	0.4638	2.3	0.95	-1.00
3	0.6318	1.2587	1.8	0.61	-0.88
4	1.1551	1.8712	1.6	0.96	-1.00
5	1.6785	2.4426	1.6	0.90	-1.00
6	2.2018	2.9964	1.4	0.46	-0.58

TABLE 3.1: Resonance strength  $\epsilon_r$  and the ratio of preserved polarisation  $P_f/P_i$  at imperfection resonances for a typical vertical orbit deviation  $y_{co}^{rms}$ , without considering synchrotron oscillation.

A spin flip occurs at all resonances if synchrotron oscillations are not considered. However, the influence of synchrotron oscillation during resonance crossing cannot be neglected. After the first imperfection resonance, the calculated polarisation with a momentum spread of  $\Delta p/p = 1 \times 10^{-3}$  and a synchrotron frequency of  $f_{syn} = \text{Hz}$  is about  $P_f/P_i \approx -0.85$ . The resonance strength of the first imperfection resonance has to be enhanced to  $\epsilon_r = 1.6 \times 10^{-3}$  to excite spin flips with polarisation losses of less than 1%. At the other imperfection resonances the effect of synchrotron oscillation is smaller, due to the lower momentum spread at higher energies. Vertical correction dipoles or a partial Siberian snake could be used to preserve polarisation at imperfection resonances by exciting adiabatic spin flips. Simulations indicate that an excitation of the vertical orbit with existing correction dipoles by 1 mrad is sufficient to adiabatically flip the spin at all imperfection

resonances. In addition, the solenoids of the electron-cooler system inside COSY are available for use as a partial snake. They are able to rotate the spin around the longitudinal axis by about  $8^\circ$  at the maximum momentum of COSY. A rotation angle of less than  $1^\circ$  of the spin around the longitudinal axis already leads to a spin flip without polarisation losses at all five imperfection resonances. The number of intrinsic resonances depends on the superperiodicity  $P$  of the lattice, which is given by the number of identical periods in the accelerator. The COSY ring consists of two  $180^\circ$  arc sections connected by straight sections. The straight sections can be tuned as telescopes with 1:1 imaging, giving a  $2\pi$  betatron phase advance. In this case the straight sections are optically transparent and the arcs contribute to the strength of intrinsic resonances. One then obtains for the resonance condition  $\gamma G = k \times P \pm (Q_y - 2)$ , where  $k$  is an integer and  $Q_y$  is the vertical betatron tune. The magnetic structure in the arcs allows adjustment of the superperiodicity to  $P = 2$  or  $6$ . The corresponding intrinsic resonances in the momentum range of COSY are listed in Table 3.2.

$P$	$\gamma G$	$T_p$ MeV	$p$ MeV/ $c$	$\epsilon_r$ $10^{-3}$
2	$6 - Q_y$	312.4	826.9	0.26
2	$0 + Q_y$	950.7	1639.3	0.21
2,6	$8 - Q_y$	1358.8	2096.5	1.57
2	$2 + Q_y$	1997.1	2781.2	0.53
2	$10 - Q_y$	2405.2	3208.9	0.25

TABLE 3.2: Resonance strength  $\epsilon_r$  of intrinsic resonances for a normalized emittance of  $1\pi$  mm mrad and vertical betatron tune of  $Q_y = 3.61$  for different superperiodicities  $P$ .

## 3.2 EDDA polarimeter

Even though the polarisation of the beam is measured at the injection via Low Energy Polarimeter (LEP), it is important to control the polarisation of the beam after it goes through all the depolarisation resonances and reaches the flattop (constant kinetic energy). This was achieved via EDDA measurements during the last 20 seconds at the end of the every cycle.

The EDDA experiment was initially conceived to provide high precision  $pp$  elastic scattering data in the COSY energy range (0.5 - 2.5 GeV), but later has been modified to be used as the internal polarimeter. The EDDA-polarimeter is comprised

of the  $7\ \mu\text{m}$  diameter carbon fibre target and  $2 \times 29$  semi-ring scintillators that intercept protons within the polar angle range from  $11.1^\circ$  to  $42.7^\circ$  in the laboratory coordinate system (Appendix A) [9].

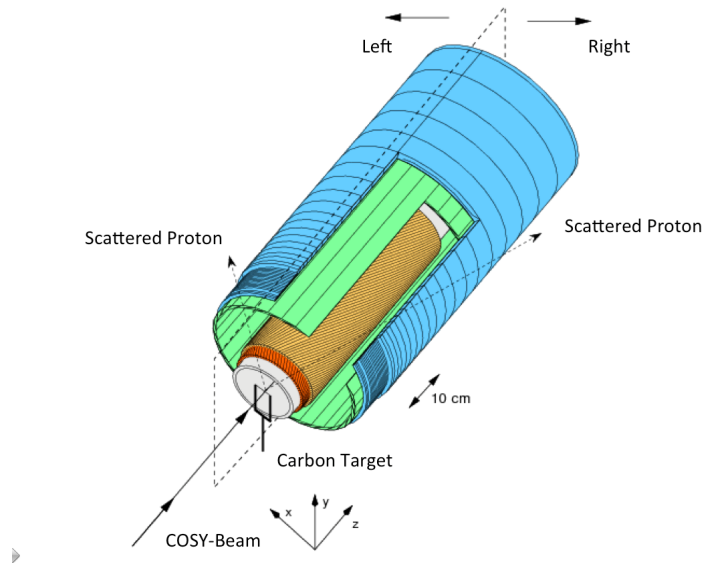


FIGURE 3.3: Schematic diagram of the EDDA detector.

The outside layer consists of a series of rings that wrap around the bars and each intercepts a narrow range of scattering angles from the target. The rings are split into left and right halves. Each half is connected to a light guide and single photomultiplier tube. The triggers are generated for each of the solid semiring-shaped scintillators, signal from which were counted in the so-called scalers. The time-marking system uses a precise clock to provide time for each event trigger. These times are stored and passed to the event processing software. The scaler rates are then read out separately for each ring and the two spin directions, and making use of cross-ratio method, and known ring effective analysing powers [17], beam polarisation is calculated.

### 3.3 ANKE spectrometer

The Apparatus for Studies of Nucleon and Kaon Ejectiles (ANKE) is an internal experiment in one of the straight section of COSY. It consists of the magnetic system (three dipole magnets), unpolarised hydrogen or deuteron cluster-jet target, and different detection systems, from which we have mostly used for this experiment only Forward Detector(FD) and Silicon Tracking Telescopes (STTs).

In Figure 3.4 only those parts of the spectrometer are shown that are relevant for this experiment.

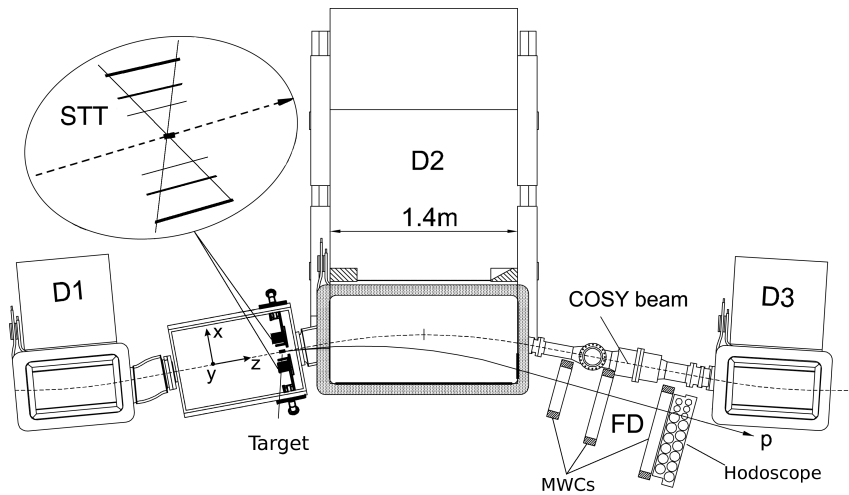


FIGURE 3.4: The ANKE spectrometer setup (top view), showing the positions of the hydrogen cluster-jet target, the silicon tracking telescopes (STT), and the forward detector (FD).

The first dipole magnet D1 deflects the circulating beam by an angle  $\alpha$  off its straight path onto the target; the spectrometer dipole magnet D2 (beam deflection  $-2\alpha$ ) separates the produced particles from the beam for momentum analysis; finally D3, identical to D1, leads the unscattered beam particles back onto the normal orbit [18]. The deflection angle of the beam can be adjusted to optimise the magnetic field up to 1.56 T independent of the COSY beam momentum.

### 3.3.1 Unpolarised cluster-jet target

For the ANKE experiments target with thickness of  $10^{13}$  to  $10^{15}$  *atoms/cm*<sup>2</sup> is typically used. For experiments that require unpolarised targets, it is provided by cluster-jet target device. It consists of three main parts: the cluster-jet source, the scattering chamber, and the cluster-jet beam dump [19].

The hydrogen or deuterium gas at pressures of 18 bar is cooled down to temperatures of 20-30 K and pressed through a Laval nozzle. Adiabatic expansion of the cooled beam further cools down the beam and the oversaturated gas spontaneously condensates to clusters with typical size of  $10^3 - 10^4$  atoms. Even though the chosen temperature, pressure and nozzle geometry have already been optimized, only a small part of used gas forms clusters. Hence the skimmer (an opening of 700  $\mu$ m) is used to separate the cluster jet from the surrounding gas. The final shape

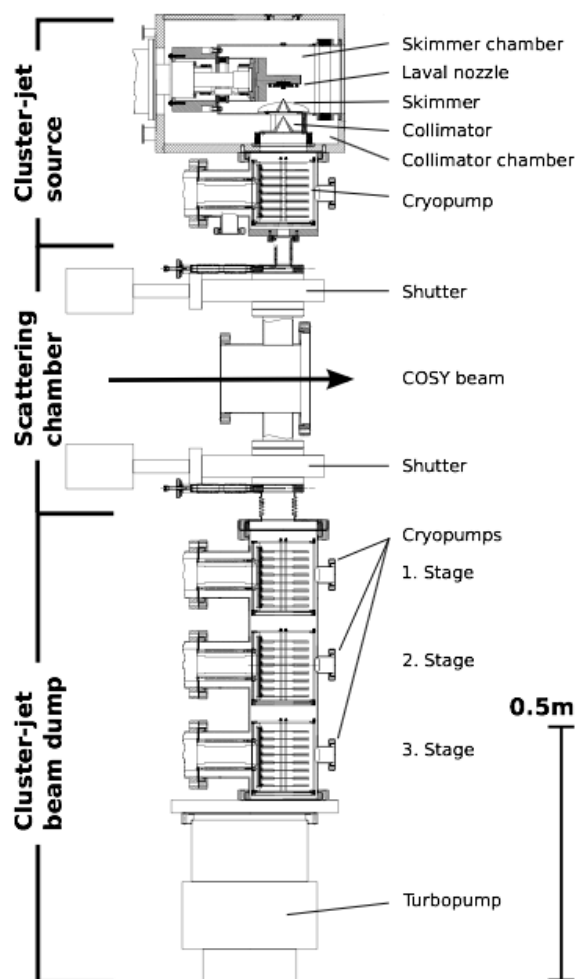


FIGURE 3.5: The cluster-jet target installed at ANKE.

of the cluster jet is defined by a second opening, collimator. Finally the cluster beam is separated from the residual gas by a skimmer.

The scattering (analysing) chamber is equipped with a scanning rod with a thickness of  $1.0\text{ mm}$  which is controlled by a stepper-motor and can be positioned in units of  $1/24\text{ mm}$ . When the rod is placed inside the cluster beam, a part of the beam is stopped and converted into a gas load which can be recorded by an ionization vacuum meter. In that way information on the cluster beam size and position can be obtained. Furthermore, if the rod is placed at a fixed position inside the cluster beam, this system allows the density of the beam to be monitored.

The part of the cluster-jet beam, which does not interact with the COSY beam, is collected in the beam dump. It consists of three cryopumps and one turbo molecular pump mounted at the end.

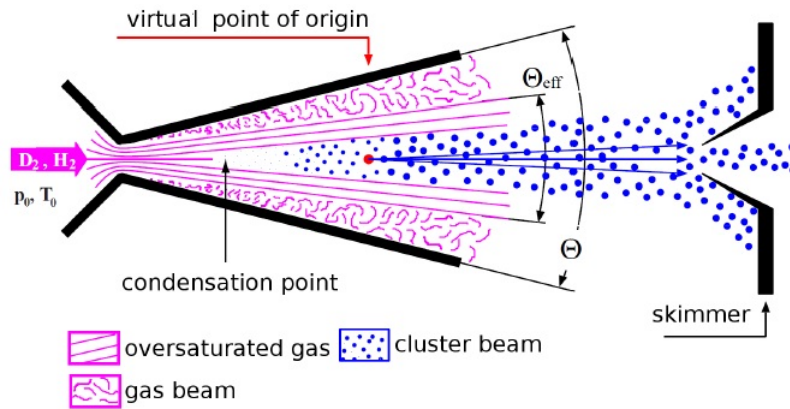


FIGURE 3.6: Cluster production at the Laval-nozzle.

### 3.3.2 Forward Detector

Forward Detector (FD) is located in the gap of 1.6 m between the D2 and D3 dipole magnets. The closeness of the FD part to the COSY beam pipe introduces the requirement for the system to operate at rather high counting rates of  $10^5 \text{ s}^{-1}$  and more.

The FD comprises two multiwire proportional (MWPC) and one drift chamber (MWDC) as well as a two-plane scintillation hodoscope. The information from MWPC and MWDC chambers are used for track reconstruction at ANKE. The existence of the strong magnetic field of the D2 ensures a good spatial separation of tracks with different mass-to-charge ( $m/q$ ) ratio. Using the hit information from different layers of the MWPC and MWDC and the geometrical position of the target, tracks are found from the overall fit procedure. Details on the track-finding algorithm and the track-reconstruction software can be found in [20] [21].

The MWPCs have four wire planes each, with two horizontally (X) and two vertically (Y) aligned wires as well as two-strip planes, which are inclined by  $\pm 30^\circ$  with respect to the wires. High spatial resolution of less than 1 mm is required from the Multiwire Proportional Chambers (MWPCs), in order to achieve momentum resolution of about 1%, which is essential for distinguishing proton-proton pairs with low excitation energy.

The forward hodoscope is composed of two planes of vertically aligned scintillators from polystyrene. The first and second planes contain 8 and 9 scintillators, respectively. In each plane, counters that are placed close to the COSY beam pipe, have smaller thickness (15 mm) and width (varying between 40 and 60 mm), compared to those responsible for lower momentum region (20 mm thick, 80 mm

wide). The height of all scintillators is 360 mm. Each of the scintillators is read out by two photomultiplier tubes placed on both ends. They provide timing as well as the amplitude signal. The timing signal can be used to form a trigger and also to measure the differences of the arrival times of particle pairs. A typical time resolution for events with two registered particles is around 0.5 ns. The amplitude signal from photomultipliers provides information about the energy loss in the scintillator, which can be measured with 10% accuracy.

### 3.3.3 Silicon Tracking Telescopes

Two Silicon Tracking Telescopes are placed inside the vacuum chamber in a  $\phi$ -symmetric (left-right) arrangement close to the beam-target overlap. Each STT consists of three individual double-sided silicon strip detectors of different thickness. The basic configuration has a 65  $\mu\text{m}$  first layer, a 300  $\mu\text{m}$  second layer and to ensure stopping of protons with kinetic energy up to 40 MeV, a third layer of 5100  $\mu\text{m}$  thickness. The first layer is placed 28 mm from the centre of the beam pipe. The distance between the two first layers is set to 20 mm.

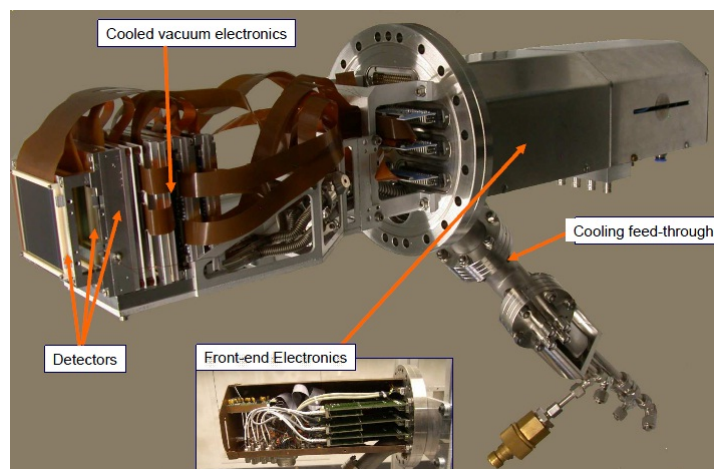


FIGURE 3.7: Silicon Tracking Telescope.

Measuring the energy losses in the individual layers of the telescope allows the identification of stopped particle by the  $\Delta E/E$  method. From the Bethe-Bloch formula, it can be seen that the energy loss in matter depends on the charge  $ze$  and the velocity of the incident particle  $v = \beta c$ .

$$-\frac{dE}{dx} = \frac{4\pi}{m_e c^2} \frac{nz^2}{\beta^2} \left(\frac{e^2}{4\pi\epsilon_0}\right)^2 \left[ \ln\left(\frac{2m_e c^2 \beta^2}{I(1-\beta^2)}\right) - \beta^2 \right], \quad (3.2)$$

where  $E$  is energy of the particle;  $x$  is the distance travelled by the particle; and  $m_e$  is mass of the electron;  $n$  is electron density of the target;  $I$  is the mean ionisation energy of the target; while  $\varepsilon_0$  is the vacuum permittivity.

Therefore, these energy losses in the layers are specific to the particle type. Ratio of energy losses with the total energy of the particle is used to identify the particles. The minimum energy of a reconstructed particle is given by the thickness of the most inner layer. It will be detected as soon as it passes through the inner layer and in the second layer [22]. This corresponds to minimum energy of 2.5 MeV for protons. The setup was built in a  $\phi$ -symmetric (left-right) arrangement to make use of the cross-ratio method. This configuration fulfils the requirement of particle identification together with a precise energy determination (1-5%) and tracking with vertex resolution of 1 mm over a wide range. The time resolution of the set-up is less than 1 ns.

### 3.4 Experimental conditions

This thesis comprises data gathered over three dedicated experiments.

- Objective: analysing power  $A_y(\theta)$  in proton-proton elastic scattering
  - Beam: polarised proton beam;
  - Target: unpolarised hydrogen cluster target;
  - Data gathered by: EDDA, ANKE STT, ANKE FD;
  - Beam Energies:  $T_p = 0.796, 1.6, 1.8, 1.965, 2.157, \text{ and } 2.368$  GeV;
  - Angular range:  $4^\circ - 30^\circ$ .
- Objective: unpolarised differential cross section in proton-proton elastic scattering  $d\sigma/d\Omega$ 
  - Beam: unpolarised proton beam;
  - Target: unpolarised hydrogen cluster target;
  - Data gathered by: ANKE FD, Schottky spectrum analyser;
  - Beam Energies:  $T_p = 1.0, 1.6, 1.8, 2.0, 2.2, 2.4, 2.6, \text{ and } 2.8$  GeV;
  - Angular range:  $12^\circ - 30^\circ$ .

- Objective: analysing power  $A_y(\theta)$  in proton-neutron quasi-free elastic scattering
  - Beam: polarised proton beam;
  - Target: unpolarised deuterium cluster target;
  - Data gathered by: EDDA, ANKE STT, ANKE FD;
  - Beam Energies:  $T_p = 0.796, 1.6, 1.8, 1.965, 2.157, \text{ and } 2.368$  GeV;
  - Angular range:  $13^\circ - 30^\circ$ .



## Chapter 4

# Analysing power in proton-proton elastic scattering

The  $\vec{p}p$  experiment at ANKE was carried out using polarised proton beam at six energies,  $T_p = 0.796, 1.6, 1.8, 1.965, 2.157,$  and  $2.368$  GeV. The calculation of the analysing power  $A_y(\theta)$  as the function of the scattering polar angle requires the measurement of the scattered particles asymmetry  $\varepsilon(\theta)$  and the beam polarisation value  $P$ .

$$\varepsilon(\theta) \propto PA_y(\theta) \quad (4.1)$$

While asymmetry  $\varepsilon(\theta)$  was calculated using ANKE detection systems (STT and FD), the beam polarisation  $P$  was measured using EDDA detector. The beam polarisation mode was changed every subsequent cycle to take the maximum advantage of the cross-ratio method, described in Section 2.3. Cycles of 180 s or 300 s duration were used for each spin mode, with the last 20 s of each cycle being reserved for the measurement of the beam polarisation with the EDDA detector. The details on beam polarisation measurement are provided in Section 4.1, while the asymmetry determination using STT and FD are given in Section 4.2. Finally, the results of the analysing power in  $\vec{p}p$  elastic scattering are discussed in Section 4.3.

### 4.1 Beam polarisation measurement using EDDA

The absolute values of the beam polarisations were measured by the EDDA polarimeter for the first time in the ANKE beam time in 2013. The EDDA carbon

fibre target was moved into the beam for the last 20 seconds of every cycle, and scaler counts were recorded. The carbon target effectively consumes all the beam, hence it could not be used before an ANKE measurement of asymmetry in a cycle.

Originally EDDA detector was equipped with a polarised atomic hydrogen target, and had been used to measure the  $pp$  analysing power over almost the whole COSY energy range [9] [10]. By studying further the scattering of polarised protons on C and CH<sub>2</sub> targets, it was possible to deduce the quasi-free analysing power of the carbon, where the necessary calibration standard was provided by the EDDA  $\vec{p}p$  data. The stripped-down version of the EDDA detector used as a polarimeter at COSY was calibrated during the EDDA data-taking periods against the full detector setup.

The beam polarisation in our experiment has been determined based on the asymmetry  $\varepsilon(\theta_{lab})$  and effective carbon analysing powers  $A_n^{eff}(C)$  in quasi-elastic scattering of the protons on carbon-bound nuclear protons. These effective analysing power values were taken from the dedicated studies in 2000 at EDDA-COSY [17].

The asymmetry term  $\varepsilon(\theta_{lab})$  was calculated via cross-ratio method Equation 2.19, using the rates in the half-rings placed to the left and right of the beam. It was possible to compare left and right count rates for each polar angle  $\theta_{lab}$  range, corresponding to the semiring (Appendix A), while averaging over azimuthal angle  $\phi$  range. Thus, the asymmetry term for each polar angle range has form:

$$\langle \varepsilon(\theta_{lab}) \rangle = \langle PA_y(\theta_{lab}) \cos \phi \rangle \approx \frac{2}{\pi} PA_y(\theta_{lab}). \quad (4.2)$$

We can deduce the beam polarisation  $P$  from  $\varepsilon(\theta_{lab})$  in an EDDA ring:

$$P_{\theta_{lab}} \approx \frac{\varepsilon(\theta_{lab})}{A_{eff}(\theta_{lab})}, \quad (4.3)$$

where  $A_{eff}$  is the effective analysing power, values for which are taken from [17]

$$A_{eff}(\theta_{lab}) = \frac{2}{\pi} A_y(\theta_{lab}). \quad (4.4)$$

The beam polarisation  $P$  does not depend of the scattering angle  $\theta_{lab}$ . In order to decrease the statistical uncertainty of  $P$  we take the advantage of this independence and form the weighted average of all  $P_{\theta_{lab}}$  as a final result for  $P$ .

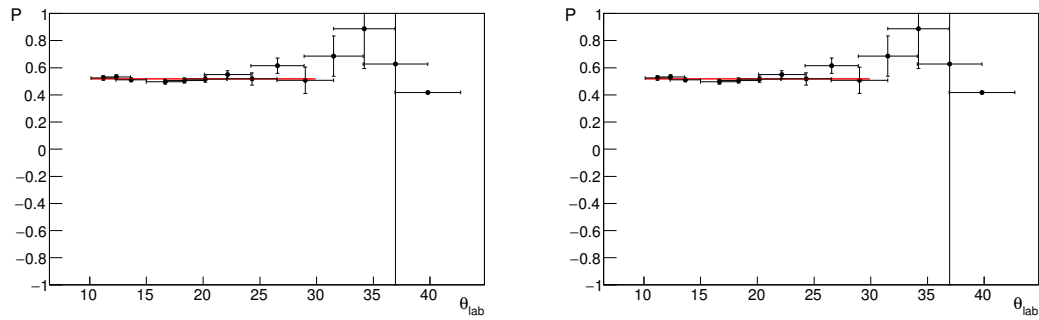


FIGURE 4.1: The polarisation values, calculated ring by ring, are shown versus corresponding laboratory polar angles (according to Appendix A). The sample plots are shown for beam kinetic energy  $T_p = 1.8$  GeV and  $T_p = 2.2$  GeV.

The weighted averages over time and polar angle of the beam polarisations determined at the six energies are given in Table 4.1. The changes in sign reflect the number of spin flips required to pass through the imperfection resonances, described in detail in Section 3.1.2. It should be noted that each of the six beams was prepared independently and, for this reason, the magnitude of the polarisation may not decrease monotonically as more resonances are crossed.

$T_p$ (GeV)	0.796	1.6	1.8	1.965	2.157	2.368
$P$	0.554	0.504	-0.508	-0.429	-0.501	0.435
$\Delta P$	$\pm 0.008$	$\pm 0.003$	$\pm 0.011$	$\pm 0.008$	$\pm 0.010$	$\pm 0.015$

TABLE 4.1: The values of the mean polarisations  $P$  determined with the EDDA polarimeter averaged over all the data at the beam energy  $T_p$ . Only statistical errors are given in the table.

Consistent results were achieved with EDDA polarimeter after the short (180 s) and long (300 s) cycles. As expected, it implies that beam polarisation is not lost at flattop (constant beam energy) over a COSY cycle. However, due to the non-zero dispersion combined with the energy loss of the beam caused by its passage through the target, the settings at the three lowest energies gradually degrade slightly. This effect was taken into account in the analysis.

#### 4.1.1 Beam polarisation uncertainty

The variation of the beam polarisation values among the cycles at any given energy was checked using EDDA with various selections and combinations of the cycles. All the studies yield the consistent results within the uncertainties at every given energy. The variation of the beam polarisation values was also checked with the

asymmetry of the counts in STT in various cycles and found to be around 0.04 (RMS).

Besides the statistical errors, shown in Table 4.1, the uncertainty of the effective carbon analysing powers should be taken into account. In the studies of the CH<sub>2</sub> and C targets for the fast beam polarisation, the systematic error for the  $A_{eff}$ , unfortunately, could be estimated only very roughly from the change of polarisation values during the calibration procedure. Unlike CH<sub>2</sub> target, C target is free of additional systematic errors occurring due to the aging of the target (loss of hydrogen ions in the interaction with beam protons). The value for the systematic uncertainty of the carbon effective analysing powers was estimated in [17] to be 3%.

## 4.2 Asymmetry measurement using ANKE

### 4.2.1 Event selection by STT

The analysis of the scattered particles, detected in STT, is based on the software, developed mainly by G. Macharshvili. It includes the codes for reconstructing tracks, using energy deposited in the layers of STT as well as the neural network method, and is described in detail in Reference [23].

Tracks were reconstructed starting from the hits in the second layer. STT trigger requested a minimum energy deposit in the second layer of either telescope. Combinations of these hits with the hits in the first layer have been considered. If the reconstructed track hits the inside the ellipse of beam-target overlay in ZOY plane (at  $x = 0$ ), then it is stored.

In general, the hit from the third layer is also added to the reconstructed track in case it is inside the 20° cone along the track with the apex at the second layer hit. The cone opening angle corresponds to the maximum angle of multiple scattering. The third layer hit does not change a track geometry, it is used only to fulfil the energy deposit information [23].

The further steps have been applied to increase the efficiency of the track reconstruction, in cases when a possible track was missing a hit in the first or second layer due to possible vicinity to the energy threshold or inactive segments. In

these cases energy deposits for the first or second layers were added to the energy loss sum in the correspondence to the missing hit, assuming  $\Delta E_2 = 5\Delta E_1$  or  $\Delta E_1 = 0.2\Delta E_2$ .

The greater precision in the angle of the recoiling proton is achieved by deducing it from the energy measured in the telescope rather than from a direct angular measurement. The Figure 4.2 demonstrates the difference between the angle reconstructed from the energy of the scattered particle and directly measured scattering angle of the track. Even though it is not possible to judge directly from Figure 4.2 the contribution of each angle to the distribution, the simulation shows that about 80% of the width of the distribution directly measured scattering angle of the track.

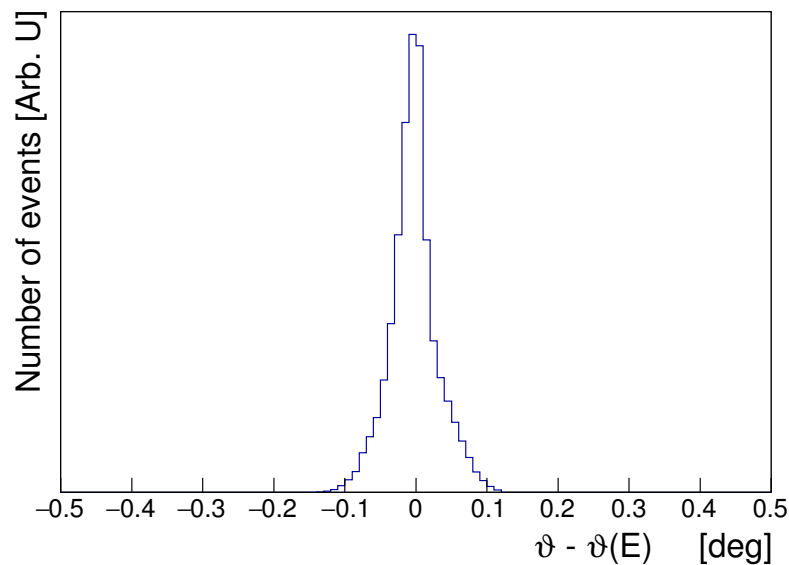


FIGURE 4.2: Difference between the angle reconstructed from the energy  $\theta(E)$  and directly reconstructed angle of the track  $\theta$ . The example plot is shown at  $T_p = 2.368$  GeV.

The protons with energies below 30 MeV were completely stopped in three layers of STT. Furthermore, it is also possible to deduce the energy of punch-through protons up to 90 MeV, Thus expanding considerably the angular coverage of the telescope. For this purpose the kinetic energy of these energetic protons was defined through a comparison of the angles and energy deposits in all three layers with simulated data using a neural network approach. The relative uncertainty was defined during the network training procedure [24] and is equal to 2% at 30 MeV and 4% at 90 MeV.

There is very little ambiguity in the isolation of the proton peak in the missing mass spectra of selected STT events (Figure 4.3).

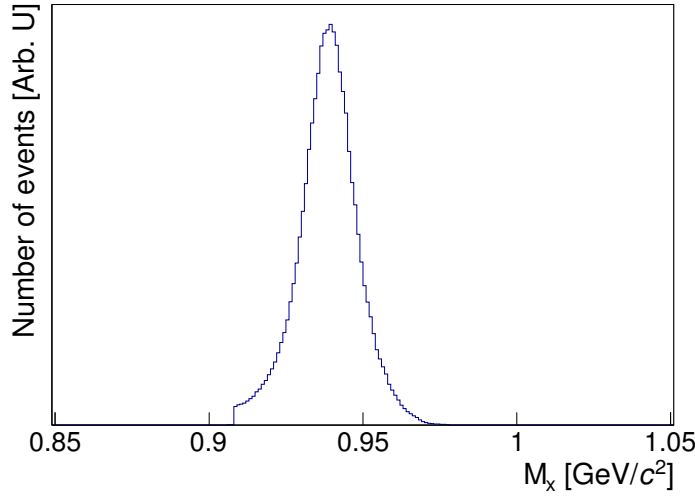


FIGURE 4.3: Missing mass  $M_X(pp \rightarrow pX)$  spectrum obtained for a beam energy of 1.6 GeV showing the clear proton peak when detecting one proton in the STT.

## 4.2.2 Asymmetry measurement using STT

The left-right symmetry of ANKE STTs, along with the reversal of the beam polarisation every subsequent cycle allowed us to use the cross-ratio method, described in the Section 2.3. The left-right asymmetry of the protons scattered to STTs in each polar angle interval is calculated as

$$\varepsilon(\theta) = \frac{L(\theta) - R(\theta)}{L(\theta) + R(\theta)}, \quad (4.5)$$

where  $L(\theta)$  and  $R(\theta)$  are the geometrical means of number of particles scattered in the given polar angle interval to the left  $L = \sqrt{N_1^\uparrow N_2^\downarrow}$  and to the right  $R = \sqrt{N_1^\downarrow N_2^\uparrow}$  in respect to the beam polarisation. As was shown previously, the scattering asymmetry is related to the analysing power  $A_y(\theta)$  for each value of the scattering angle  $\theta$  through

$$\varepsilon(\theta) = A_y(\theta)P\langle \cos\phi \rangle \quad (4.6)$$

The  $\phi$  acceptances for the left and right STTs differ only slightly:  $\langle \cos\phi \rangle_1 = 0.9663 \pm 0.0005$  and  $\langle \cos\phi \rangle_2 = 0.9670 \pm 0.0003$ . The simulation showed that even larger difference between  $\langle \cos\phi \rangle_1$  and  $\langle \cos\phi \rangle_2$  would not affect the measured asymmetry. Therefore, we assume that  $\phi$  acceptances of the detectors are the same and in our calculations  $\langle \cos\phi \rangle \approx 0.9666$  can be used.

### 4.2.3 Event selection by FD

Scattered particles, which pass through the vacuum chamber of the D2 magnet and leave it through the forward exit window, are detected in FD. The analysis is based on the software, developed mainly by S. Dymov. It includes the codes for finding tracks and reconstructing particle momenta and is described in detail in Reference [20].

The precision of the momentum and angle reconstruction is directly related to the accuracy of the ANKE geometry measurement. Positions and sizes of various parts of the ANKE spectrometer are well defined and fixed, but there are some parameters in the track reconstruction software that change from one beam time to another and it is not possible to measure them directly with enough precision. Uncertainties in these parameters shift the reconstructed particle momenta and consequently result in shifts in missing mass spectra. Therefore, these parameters should be calibrated for every beamtime individually.

The setup parameters are adjusted using the kinematics of different reactions. For every iteration of the fitted parameters, the program reconstructs tracks from scratch and looks at the displacement of the missing masses from their nominal values for every reaction. After the geometry adjustment, the hit coordinates and the time of flight are used for the final track reconstruction. The energy loss cut for elastic proton identification is relevant only at the 0.796 GeV beam energy, where the forward going deuterons from the  $pp \rightarrow d\pi^+$  have the momenta close to that of the  $pp$  elastic protons. After the applied cuts the admixture of those deuterons does not exceed 0.02%.

The number of elastic protons was determined from the missing mass spectra after subtracting a linear background from the peak in each angular bin. Typical missing mass spectrum is shown in Figure 4.4.

The setup acceptance was defined from GEANT simulation, followed by the same track and momentum reconstruction procedures that were applied to the data. Although the final results were obtained without further restriction on the  $\phi$  range, estimations done with several  $\phi$  cuts showed no change beyond the statistical fluctuations. The angular acceptance at 1.6 GeV is shown in Fig. 4.5 and it looks rather similar at the other energies.

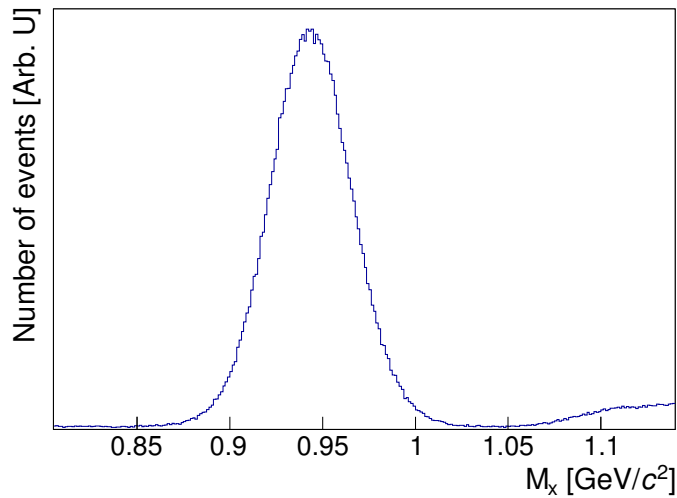


FIGURE 4.4: Missing mass  $M_X(pp \rightarrow pX)$  spectrum obtained from the particles detected in forward detector at the beam kinetic energy of 1.6 GeV.

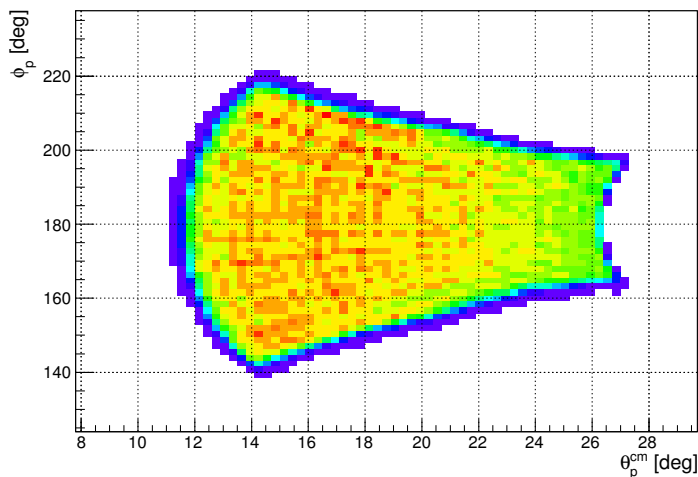


FIGURE 4.5: Forward detector angular acceptance for  $pp \rightarrow pp$  at the beam kinetic energy of 1.6 GeV.

#### 4.2.4 Asymmetry measurement using FD

The absence of the left-right symmetry in the forward detector does not permit the use of the cross-ratio method to determine the asymmetry. Therefore, the analysing power can only be defined from the asymmetry of the count rates for the two states of the beam polarisation. In this case the asymmetry is introduced as

$$\varepsilon(\theta) = \frac{N_{\uparrow}(\theta)/L_{\uparrow} - N_{\downarrow}(\theta)/L_{\downarrow}}{N_{\uparrow}(\theta)/L_{\uparrow} + N_{\downarrow}(\theta)/L_{\downarrow}} \quad (4.7)$$

in terms of luminosity-normalised numbers of counts for the two orientations of the beam polarisation  $N_{\uparrow}(\theta)/L_{\uparrow}$  and  $N_{\downarrow}(\theta)/L_{\downarrow}$ , or

$$\varepsilon(\theta) = \frac{N_{\uparrow}(\theta) - N_{\downarrow}(\theta)/L_{rel}}{N_{\uparrow}(\theta) + N_{\downarrow}(\theta)/L_{rel}} \quad (4.8)$$

in terms of the relative luminosity factors  $L_{rel} = L_{\uparrow}/L_{\downarrow}$ . These factors were fixed by comparing the rates of charged particle production in angular regions where the beam polarisation could play no part [25].

The luminosity calibration data, which corresponded generally to inelastic events involving pion production, were selected by putting cuts either on small polar angles  $\theta$  or on the azimuthal angle  $\phi$  near  $\pm 90^\circ$ . In Figure. 4.6 three groups of events with decreasing level of cut tightness are shown:

- i)  $\theta < 0.5^\circ, ||\phi - 90| < 5^\circ$
- ii)  $\theta < 1^\circ, ||\phi - 90| < 10^\circ$
- iii)  $\theta < 2^\circ, ||\phi - 90| < 20^\circ$ .

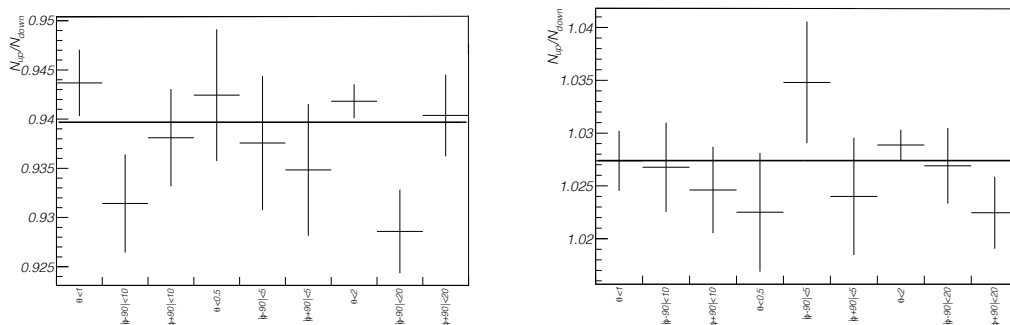


FIGURE 4.6: Luminosity ratios with different angular cuts. Example plots are shown for  $T_p = 1.8$  GeV (left panel) and 2.368 GeV (right panel).

Luminosity ratios in the three group of cuts are consistent within the statistical uncertainty. For the calculation of the asymmetry, the average value of the relative luminosity factors, gained from the abovementioned cuts, was used as the normalisation factor in Equation 4.8.

#### 4.2.5 Sources of the systematic uncertainties

The cross-ratio method allows one to eliminate first order systematic errors that arise from misalignments between the left and right STTs. Other systematic errors

for the asymmetry obtained at STT, such as those arising from differences in the magnitudes of the up and down polarisations, also cancel in the first order. Nevertheless, the systematic uncertainties of STT data were investigated further to the higher order by varying all the inputs to the reasonable levels, and observing the change in the asymmetry. The data gained using FD lacks these advantages and relies on the correct normalisation with the relative luminosities. The three groups of angular cuts, described previously, yielded consistent results within statistical errors. As a result, it is estimated the systematic uncertainty of  $A_y$  due to the normalisation procedure does not exceed 0.3%.

#### 4.2.5.1 Difference in polarisation values for two polarisation modes

Low Energy Polarimeter (LEP) measurements showed that at the injection into the COSY ring, the polarisation magnitudes for polarisation modes “up” and “down” are less than statistical uncertainty of 1%. After the acceleration the difference between the values for two modes may be larger. However, even assuming  $|P_{\uparrow} - P_{\downarrow}| = 0.1$ , the correction term for the asymmetry measured at STT is less than  $5 \cdot 10^{-4}$  and can be ignored. The difference between the polarisation magnitudes is potentially more serious for the FD analysis, the same assumption of  $|P_{\uparrow} - P_{\downarrow}| = 0.1$  could induce fractional errors in  $A_y$  of up to 2.5%. It should, however, be remarked that in the overlap regions of the STT and FD data any disagreements between the determinations of the asymmetries in the two systems are on the 1% level and this puts a much tighter constraint on possible  $|P_{\uparrow} - P_{\downarrow}|$  differences.

#### 4.2.5.2 Polar angle

Misalignment of the left and right STT detectors, i.e. the angles  $\theta_1$  and  $\theta_2$  measured at two telescopes are different, may raise the fake asymmetry. Assuming  $|\theta_1 - \theta_2| \simeq (0.5 \pm 1.0)^\circ$  for each  $\theta$  bin, estimated from  $\theta - \theta(E)$  distribution variance (Figure 4.2), the upper limit for the systematic error induced by STT detectors misalignment is  $1.5 \cdot 10^{-3}$  at the beam kinetic energy of 0.796 GeV and by factor of 2 smaller at the higher energies.

One can estimate the precision of the measured scattering angle at FD indirectly from the  $pp \rightarrow d\pi^+$  reaction. The simultaneous measurement of the deuteron and pion in FD showed that the precision of the horizontal transverse momentum  $\Delta P_x$  is less than 1.5 MeV/c. This corresponds to the systematic deviation in the

laboratory angles from those expected for these kinematics  $\Delta\theta_{lab} < 0.07^\circ$ . If this is valid also for  $pp$  elastic scattering it would suggest that the c.m. scattering angles were defined with a precision of better than  $0.15^\circ$ .

In cases where one of the protons from an elastic scattering event is detected in the FD and the other in the STT it is possible to compare directly the scattering angle measured in the two systems. Figure 4.7 shows the difference of the results from the two detectors. The STT angle is calculated from the energy deposited, and the different curves show the tracks reconstructed with the corresponding STT layers.

In general, the STT angle is larger than the FD one, with the difference being typically  $\approx 0.3^\circ$ . It is not possible to judge which detector is responsible for this difference which is, however, small compared with the bin widths of  $1.0^\circ$  (FD) and  $1.2^\circ$  (STT).

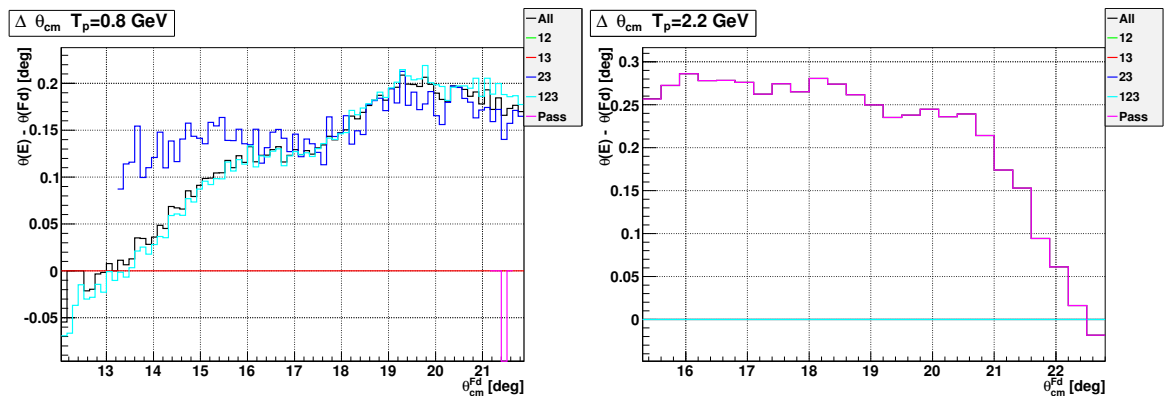


FIGURE 4.7: Difference of scattering angle reconstructed in FD and STT. Example plots are shown for  $T_p = 0.796$  GeV (left panel) and  $2.157$  GeV (right panel).

To estimate the impact of the angular deviation onto  $A_y$ , for each energy we approximated the reconstructed  $A_y$  dependence with a parabola. Then, one can calculate the relative change of  $A_y$  occurring due to the constant shift in angle  $\delta A_y = (A_y(\theta) - A_y(\theta + \delta\theta))/A_y(\theta)$  (Figure 4.8). The maximal error of 2.5% is obtained at 0.796 GeV.

#### 4.2.5.3 Detector efficiencies stability

Another factor that could affect the asymmetry measured using STTs is an instability of two detectors efficiencies in time. To be more precise, the ratio of the efficiencies of the two telescopes  $r = E_1/E_2$  should be constant to avoid the fake

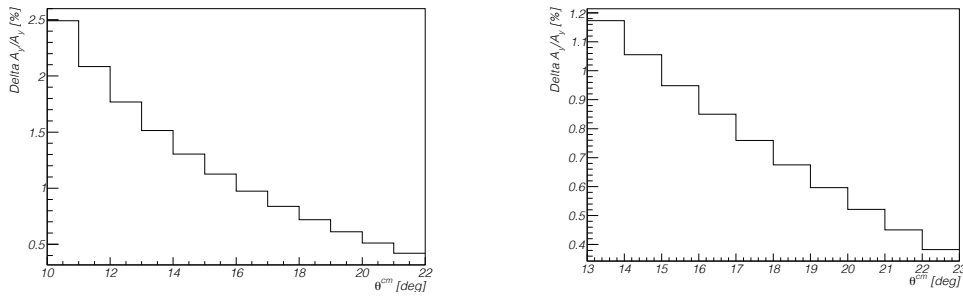


FIGURE 4.8: Systematic error due to the shift of the scattering angle. Example plots are shown for the beam kinetic energies  $T_p = 0.796$  GeV (left panel) and  $2.368$  GeV (right panel).

asymmetry. Let us introduce the instability factor  $r_{\uparrow}/r_{\downarrow}$  that should be equal to 1, in case the efficiencies ratios are the same for the both beam polarisation modes.

The angular dependence of typical average ratio  $r_{\uparrow}/r_{\downarrow}$  at the beam energies of  $0.796$  and  $1.8$  GeV are shown in Figure 4.9. In almost all cases the fitted constants are indeed close to 1 (with  $\chi^2/ndf \simeq 1$ ).

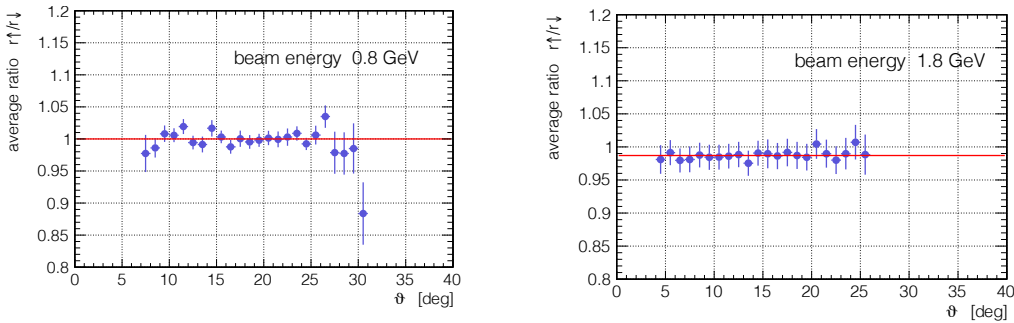


FIGURE 4.9: The instability factor  $r_{\uparrow}/r_{\downarrow}$  angular dependences at the beam energies of  $0.796$  GeV (left panel) and  $1.8$  GeV (right panel).

The uncertainty of the fitted constant can be interpreted as the systematic uncertainty induced by the detector instability, i.e.

$$\Delta A_y(\theta) \approx (1 - r_{\uparrow}/r_{\downarrow})A_y(\theta) \equiv c(\theta)A_y(\theta). \quad (4.9)$$

The STT detector efficiency instability correction, which was studied at all energies, does not exceed the  $|c| = 1.3\%$  that was found at  $1.8$  GeV. The relevant corrections of the analysing power  $c(\theta)A_y(\theta)$  were added for each angular bin of the analysing power, obtained from STT data set.

In order to simulate the maximum possible systematic error, induced by STT detectors inefficiencies,  $c = 1 - r_{\uparrow}/r_{\downarrow} = 0.2$  was introduced into the simulation. After the correction factor was applied, the angular dependence of the systematic uncertainty has been simulated once more, and the obtained systematic uncertainties were typically of the order  $10^{-3}$  that is one order smaller than prior to the correction.

The efficiency for registering events in FD were studied by using events where both the fast and recoil protons were measured in the FD and STT, respectively. The efficiencies obtained per cycle are shown in Figure 4.10, summarised separately for the two beam polarisation modes. This value is expected to be lower than 100% due to a small fraction of misidentified protons in STT as well as the possibility of multiple particles recorded in STT or FD within single trigger. There is also a small inefficiency of the FD trigger ( $\lesssim 1\%$ ) and a loss of particles due to the large angle scattering or interaction with the detector material.

Most importantly, the difference of the efficiencies between the two polarisation modes is of less than  $10^{-3}$  that is within the statistical uncertainties.

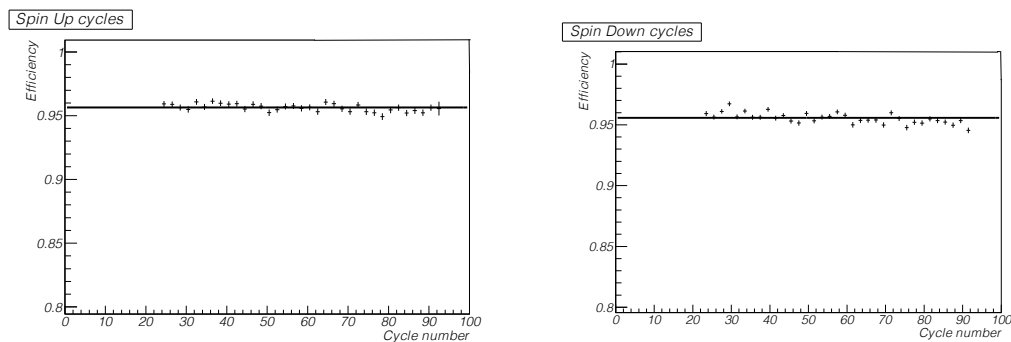


FIGURE 4.10: Efficiency of the elastic event reconstruction in FD in the cycles with the beam polarisation mode up (left panel) and beam polarisation mode down (right panel).

#### 4.2.5.4 Summary on systematic uncertainties

The overall systematic uncertainty in  $A_y$  arising from asymmetry measurement with STT does not exceed 0.3%. The dominant systematic error is, hence, that arising from the determination of the beam polarisation in the EDDA polarimeter, which was estimated to be 3% [17]. For the FD data there is, in addition, a possible contribution associated with the assumption of equal up and down polarisations so that in this case we would cautiously assume a 5% systematic uncertainty. To

these figures must be added the statistical uncertainty in the determinations of the beam polarisations at the six energies shown in Table 4.1.

### 4.3 Results and discussion

The results of all the ANKE measurements of  $A_y$  for  $pp$  elastic scattering are shown for the six energies in Figure 4.11. For the final results, only those cycles were used that contained good quality data in all detectors: FD and STT, as well as EDDA polarimeter.

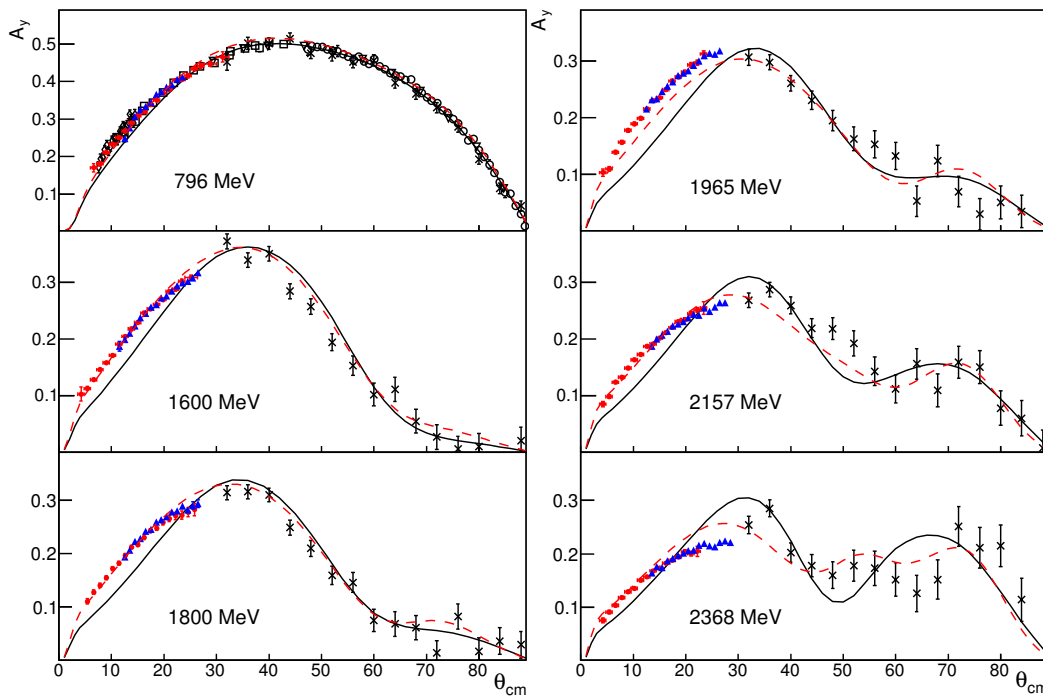


FIGURE 4.11: Comparison of the ANKE measurements of the proton analysing power in  $pp$  elastic scattering using the STT (red filled circles) and FD (blue filled triangles) systems with the curves corresponding to the SAID 2007 (solid black line) [5] and the revised fit (dashed red) solutions. Only statistical errors are shown so that the systematic uncertainties arising, for example, from the calibration of the EDDA polarimeter have not been included. Also shown are selected results from EDDA (black crosses) [10] at the energies different by no more than 7 MeV and, at 0.796 GeV, LAMPF [26–28], and SATURNE [29] (black open symbols).

The agreement between the STT and FD data, which involved completely independent measurements of the final state, is remarkably good. The individual deviations generally lie within the statistical uncertainties and the average Over the angular overlap regions is  $A_y(FD)/A_y(STT) = 1.00 \pm 0.01$ . At beam energies

close to 0.796 GeV there are many measurements of the  $pp$  analysing power and, in general, they are in good mutual agreement, as they are with the new ANKE data. This reinforces the confidence in the use of the EDDA polarimeter. At 1.6 GeV and above there are far fewer experimental measurements and, for clarity, we only show the EDDA data at neighbouring energies though, at the highest energy, the statistical fluctuations are significant [10].

The SAID 2007 solution [5], shown by the solid black line in Figure 4.11, describes the bulk of the  $\approx 0.796$  GeV data very well indeed. However, at higher energies the ANKE data deviate significantly from the predictions of the 2007 solution. Moreover, the shapes of the ANKE data seem very different from these predictions, rising much more steeply at small angles. Therefore, these discrepancies cannot be due to a simple miscalibration of the EDDA polarimeter, for example, which would change the overall magnitude of  $A_y(\theta)$  but not its angular dependence.

The ANKE analysing power data have been added to the world data set and searches made for an updated partial wave solution. To allow for possible systematic effects, the SAID fitting procedure introduces a scale factor  $N$  into any data set and determines its value, as well as the  $pp$  phases and inelasticities, by minimising an overall  $\chi^2$  for the complete data set. When this is done, the average value of  $\chi^2$  per degree of freedom found for the ANKE STT data is 1.6 and slightly larger for the FD results. The new fits, which lead to the red dashed curves in Figure 4.11, correspond to relatively modest changes to the parameters of the lower partial waves, with the biggest changes in  ${}^3F_2$  and  ${}^3F_4$  (Figure 4.12).

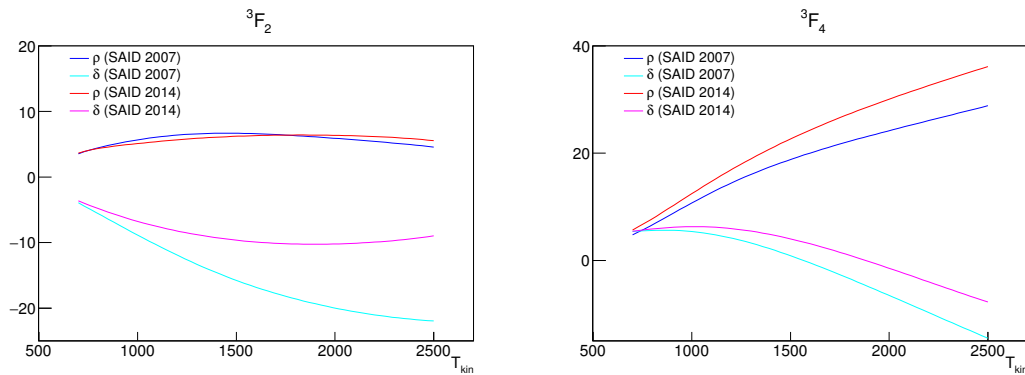


FIGURE 4.12: Phase shift parameters for  ${}^3F_2$  and  ${}^3F_4$  partial waves from the 2014 SAID solution, in comparison with the older solution from 2007.

The values of the normalisation factors  $N$  reported in Table 4.2 have an average of  $\langle N \rangle = 1.00 \pm 0.02$  for the STT data. These factors, which would effectively multiply the beam polarisations, have not been applied in Figure 4.11. The deviations of the individual values of  $N$  from unity might seem to be greater at the higher

energies. They are somewhat larger than what one would expect on the basis of the quoted uncertainties in the EDDA polarimeter, being around 5% rather than the 3% estimate [17]. It should be stressed that the introduction of the scale factor  $N$  does not change the shape of a distribution and, even in cases where a value close to one is found, this does not mean that the fit reproduces perfectly the data. A clear example of this is to be found in the larger angle data at 1.6 GeV shown in Figure 4.11.

$T_p$ (GeV)	0.796	1.6	1.8	1.965	2.157	2.368
$N$	1.00	1.00	0.99	1.09	1.01	0.93

TABLE 4.2: The normalisation factors  $N$  obtained in a partial wave fit [30] to the current STT data.

## 4.4 Conclusion

We have measured the analysing power in  $pp$  elastic scattering at 0.796 GeV and at five energies from 1.6 GeV up to 2.4 GeV using both the silicon tracking telescopes and the forward detector. The consistency between these two independent measurements of the final protons is striking so that the only major systematic uncertainty is the few percent associated with the calibration of the EDDA polarimeter. Though the overall uncertainties are slightly larger for the FD data, these results are important because they extend the coverage to slightly larger scattering angles.

In the small angle range accessible to ANKE, the new data are consistent with older measurements around 0.796 GeV and also with the 2007 SAID predictions at this energy [6]. At higher energies the ANKE results lie significantly above the 2007 solution near the forward direction and also display a different angular dependence. By adjusting some of the phases and inelasticities in the low partial waves by up to 60%, the new SAID solution [30] was obtained that provides a much better description of the new ANKE  $A_y$  data.

## Chapter 5

# Cross section in proton-proton elastic scattering

As was shown in the introduction (Figure 1.2), there are relatively few measurements of  $pp$  elastic scattering for beam energies above about 1 GeV in the angular range between  $10^\circ$  and  $30^\circ$ . This falls between the region of major Coulomb effects and the larger angles where the EDDA collaboration has contributed extensively. This lack of information on the differential cross section and analysing power inevitably leads to ambiguities in any  $pp$  PWA at high energies. To address this gap in our knowledge, ANKE collaboration has carried out the studies of the  $pp$  analysing power, presented in the previous chapter, and differential cross section, which is discussed in this chapter.

The differential cross section  $d\sigma/d\Omega$  measurements were performed using the ANKE unpolarised hydrogen cluster-jet target and the unpolarised proton beam at eight kinetic energies  $T_p = 1.0, 1.6, 1.8, 2.0, 2.2, 2.4, 2.6, 2.8$  GeV for center-of-mass angles in the range from  $12^\circ$ - $16^\circ$  to  $25^\circ$ - $30^\circ$ , depending on the energy. As was the case for the analysing power  $A_y$ , the present studies of  $d\sigma/d\Omega$  were carried out using the ANKE spectrometer. However, for  $d\sigma/d\Omega$  investigations only forward detection system was used to detect fast protons from elastic  $pp$  scattering.

In general, the cross section  $\sigma$  for a given physical process is given in terms of the corresponding counting rate  $R$  and the luminosity  $L$  through:

$$\sigma = \frac{R}{L}. \quad (5.1)$$

The biggest challenge is to establish the beam-target luminosity at the few percent level, because the overlap of the beam and target can not be deduced with such precision from macroscopic measurements. The details on the luminosity determination are provided in Section 5.1, while the count rate analysis using FD is shortly described in Section 5.2. Finally, the results of the differential cross section in  $pp$  elastic scattering are discussed in Section 5.4.

## 5.1 Luminosity determination

The knowledge of the luminosity is the crucial element of cross section measurement. The ANKE collaboration and the COSY machine crew have jointly developed a very accurate method for determining the absolute luminosity in an experiment at an internal target position. The technique relies on measuring the energy losses due to the electromagnetic interactions of the beam as it passes repeatedly through the thin target and measuring the shift of the revolution frequency by studying the Schottky spectrum [31]. In order to extract the cross section of any reaction, the absolute value of the luminosity must be determined. For the fixed target experiments, luminosity is completely defined by:

$$L = n_B \times n_T, \quad (5.2)$$

where  $n_B$  is the particle current of the incident beam and  $n_T$  is the effective target thickness, expressed as an areal density. The measurement of the beam intensity  $n_B$  is performed via the high precision Beam Current Transformer (BCT) devices (Section 5.1.1). The effective target density  $n_T$  is determined via the measurement of the beam revolution frequency shift caused by the electromagnetic interaction of the beam and target particles (Section 5.1.2).

### 5.1.1 Beam intensity measurement

For the given experiment, the BCT signal was introduced directly in the data stream. The amplitude of the BCT signal is proportional to the current, created by beam particles,  $I_b = Nfe$ , where  $N$  is number of particles,  $f$  is revolution frequency, and  $e$  is particle charge. In Figure 5.1 typical raw signal from BCT is shown.

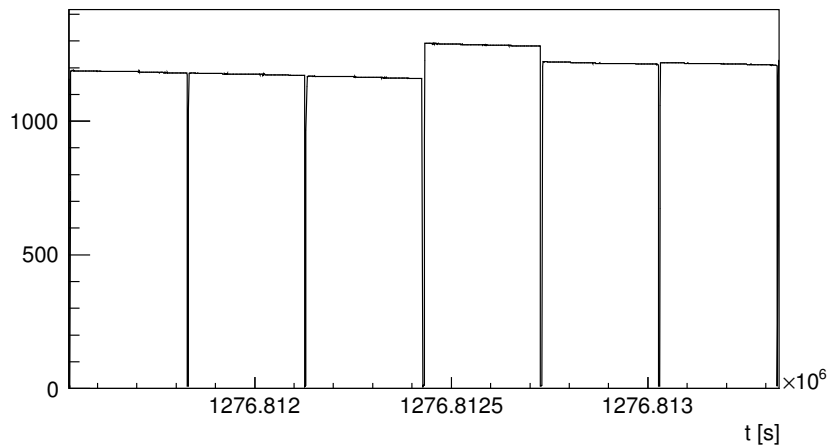


FIGURE 5.1: Beam Current Transformer (BCT) typical raw signal, recorded during the experiment.

The BCT signal has been calibrated via inserting the wire inside the beamline, and taking measurement of the BCT signal, while changing the current in the wire. The result of this calibration is given in Figure 5.2 and it does not depend on the energy of the beam.

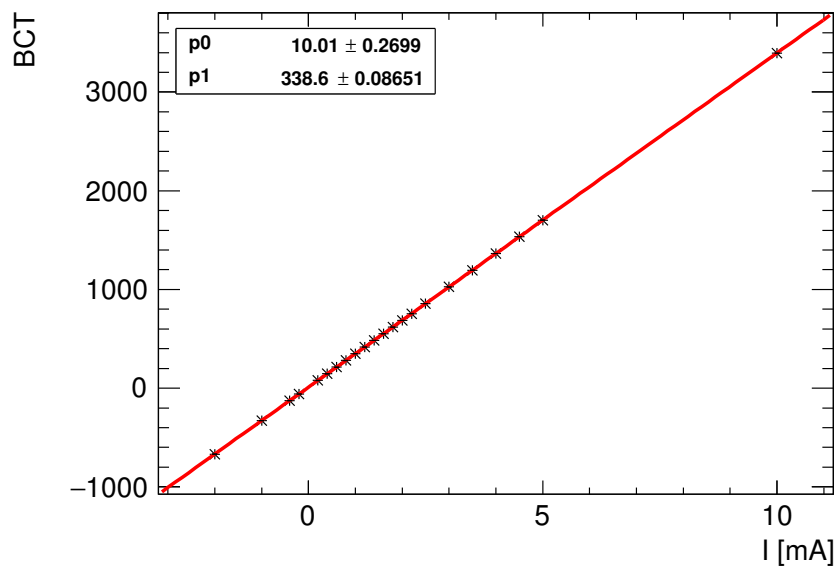


FIGURE 5.2: Calibration of Beam Current Transformer signal via applying different current  $I$  to the wire inserted into the beamline.

The particle current of the incident beam  $n_B$  was deduced from the calibrated BCT signal. These measurements were carried out every second over the 300 s cycle and then averaged. The final results are accurate to better than  $10^{-3}$ .

### 5.1.2 Target density determination

When a charged particle passes through the matter, it loses energy through electromagnetic interaction. Inside the storage ring an uncooled beam goes through a thin target a very large number of times. The energy loss, which is proportional to the target thickness, builds up steadily in time and causes a shift in the revolution frequency  $f_0$ . This shift can be determined by studying the Schottky power spectrum of the beam [32].

The energy loss  $\delta T$  per single passage through the target, divided by the stopping power  $dE/dx$  and the mass  $m$  of the target atom, yields the number of target atoms per unit area that interact with the beam:

$$n_T = \frac{\delta T}{(dE/dx)m}. \quad (5.3)$$

Over a small period of time the beam makes  $f_0 \Delta t$  traversals with the corresponding energy loss  $\Delta T$ . Hence, Equation 5.3 maybe written in terms of energy loss, as

$$n_T = \frac{\Delta T}{f_0(dE/dx)m\Delta t}, \quad (5.4)$$

or applying logarithmic differentiation, in terms of change in the beam momentum as

$$n_T = \frac{1 + \gamma}{\gamma} \frac{T_0 \Delta p}{f_0(dE/dx)m p_0 \Delta t}. \quad (5.5)$$

$T_0$  and  $p_0$  are the initial values of the beam kinetic energy and momentum and  $\gamma$  is the Lorentz factor.

The fractional change in the revolution frequency is proportional to that in the momentum through the so-called frequency-slip parameter  $\eta$ :

$$\frac{\Delta f}{f_0} = \eta \frac{\Delta p}{p_0}. \quad (5.6)$$

Putting the expressions 5.5 and 5.6 together, we obtain

$$n_T = \left( \frac{1 + \gamma}{\gamma} \right) \frac{1}{\eta} \frac{1}{(dE/dx)m} \frac{T_0}{f_0^2} \frac{df}{dt}. \quad (5.7)$$

The stopping power  $dE/dx$  and mass of the target atoms are well known and easily accessible at NIST-PML data base [33]. The initial values of frequency and energy of the beam, as well as the Lorenz factor are routinely measured for every

experiment at COSY. Therefore, the only missing parameters are frequency-slip parameter  $\eta$  and beam revolution frequency shift during the data taking  $df/dt$ .

The frequency-slip parameter  $\eta$  can be expressed in terms of  $\alpha$ , the so-called momentum compaction factor, which is constant for a given lattice setting:

$$\eta = \frac{1}{\gamma^2} - \alpha. \quad (5.8)$$

The revolution frequency depends on the particle speed  $\beta c$  and orbit length  $L$  through  $f = \beta c/L$ , where due to dispersion,  $L$  is also a function of the momentum.

$$\frac{df}{f} = \left( \frac{1}{\gamma^2} - \alpha \right) \frac{dp}{p}. \quad (5.9)$$

An estimate of  $\alpha$ , which is constant for a given lattice setting, may be done by a computer simulation of the accelerator, but greater precision is achieved by a direct measurement.

### 5.1.2.1 Schottky noise

The beam in the synchrotron consists of a finite number of charged particles. A current created by these charge carriers has some statistical fluctuation, that were investigated first by W. Schottky [34].

The current fluctuations induce a voltage signal at a beam pick-up. The Fourier analysis of this voltage signal by a spectrum analyser delivers frequency distribution around the harmonics of the revolution frequency. The frequencies of COSY were measured with the existing Schottky pick-up of stochastic cooling system, which is optimized to operate in GHz region. The harmonic number 1000 of COSY revolution frequency was measured with a more precise analyser than the one used in previous measurements [31]. Schottky noise current is proportional to the square root of number of particles in ring. The amplitudes of the measured distributions are therefore squared to give the Schottky power spectra, which are representative of the momentum spread of the beam.

The Schottky signals were recorded every 10 s with a 189 ms sweep time, resulting in effectively instantaneous spectra. For ease of representation, only the results from every 60 seconds are shown in Figure 5.3.

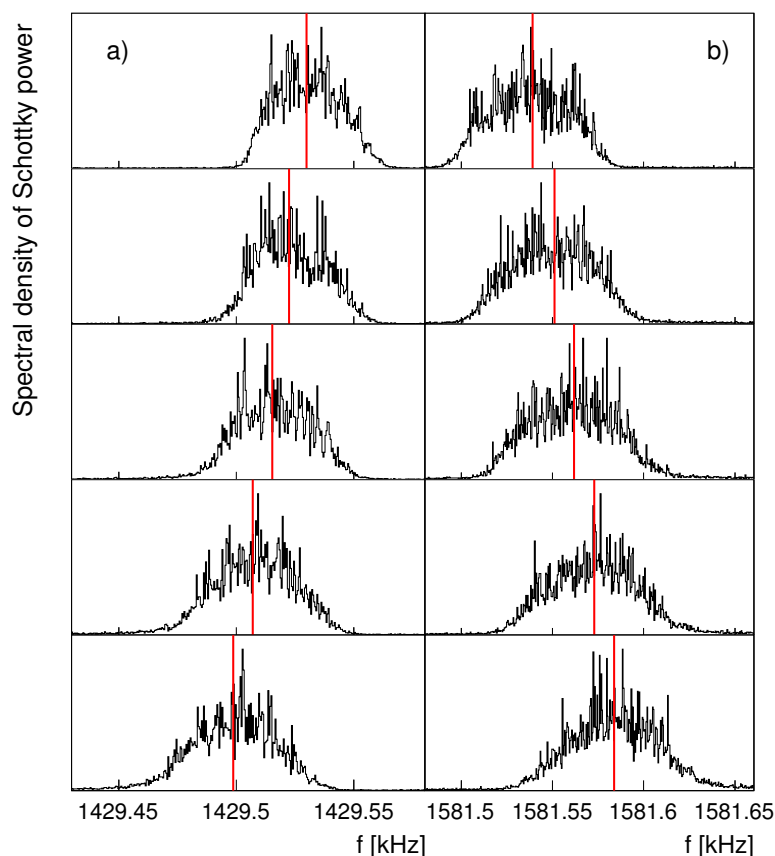


FIGURE 5.3: Schottky power spectra obtained during one 300 s cycle and scaled to harmonic number 1 for 1.0 GeV (a) and 2.0 GeV (b). The mean frequencies are indicated by the vertical (red) lines.

The background is estimated by excluding data within  $3\sigma$  on the side of no tail in the Schottky spectrum, and  $5\sigma$  in case the tail is present. The background estimates from both sides of the spectra are averaged in order to obtain the final background estimation, which is used for subtraction from the original spectrum.

### 5.1.2.2 Frequency shift

The frequency  $f$  of the beam at each instantaneous measurement was evaluated from the centroid of the Schottky power spectra distribution after subtracting the background noise. These mean frequencies are indicated by the vertical red lines in Figure 5.3.

The point of transition, where  $df$  changes its sign, occurs when  $\alpha = 1/\gamma_{tr}^2$ . Near the transition point  $\eta$  is small and this is the principal restriction on the applicability of the method. For COSY the transition occurs for  $T \approx 1.3$  GeV, for this reason the experiments were not conducted between 1.0 GeV and 1.6 GeV. As one can

see, the overall frequency shift in the cycle, which is comparable to the spectra width, is negative for 1.0 GeV and positive for 2.0 GeV. The example energies in Figures 5.3 and 5.4 were chosen, because 1.0 GeV is below and 2.0 GeV is above the transition point.

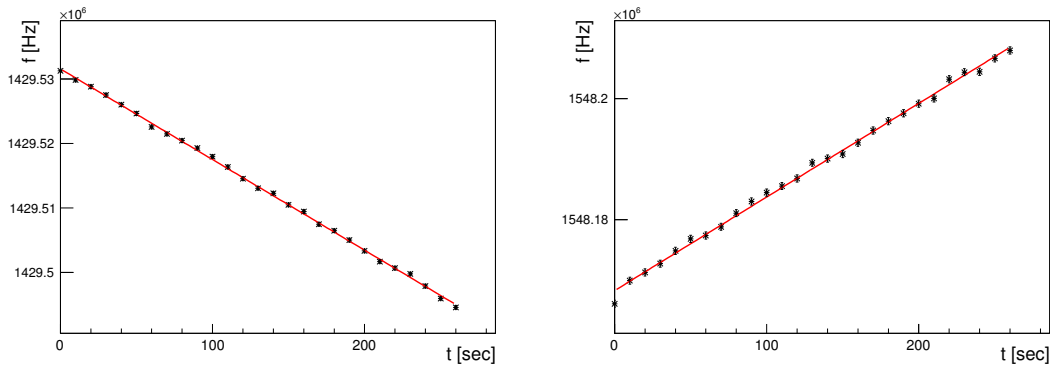


FIGURE 5.4: Typical mean frequency shift derived from the Schottky power spectra of the type illustrated in Figure 5.3 for 1.0 GeV (left panel) and 2.0 GeV (right panel)

The frequency change  $df/dt$  shouldn't be dependent on time in cycle. Hence, by checking  $df/dt$  dependence on time within the cycle via averaging many cycles, one can check the stability of target effective density, which also accounts for beam-target overlap change during the cycle.

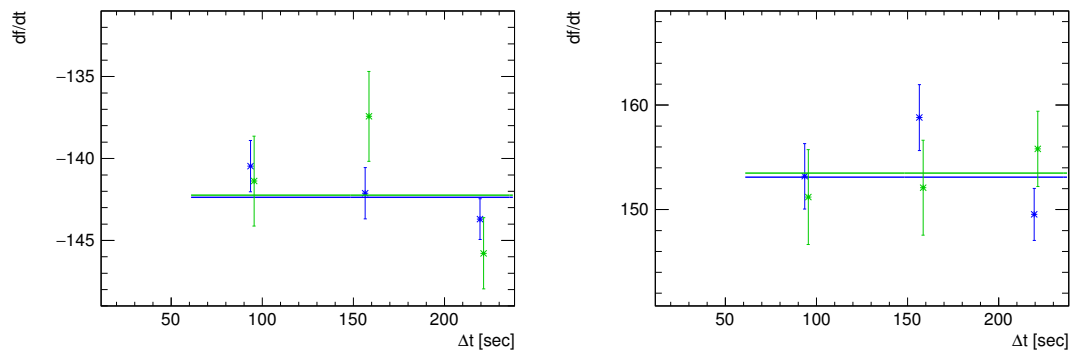


FIGURE 5.5: Average frequency shifts within the cycle duration, measured by new (blue) and old (green) spectrum analysers at 1.0 and 2.0 GeV.

### 5.1.2.3 Background correction

A small frequency shift is produced by the interaction of the beam with the residual gas in the COSY ring. Besides, the target produces additional background in the ANKE chamber. In order to account for these systematic effects, dedicated cycles

were developed, where the ANKE cluster target was switched on, but the beam was steered away from it.

Even though these measurements already account for both effects, the separate cycles with target switched off, were performed, to estimate the pure effect of the residual gas, and to check that the beam was successfully steered away from the target. Figure 5.6 shows an example of these measurements at 1 GeV. As one can see, the effects from the ANKE target and residual gas together, as well as residual gas only are small, but distinguishable. The corresponding uncertainties of the background measurement have been accounted for in the systematic errors summary (see details in Table 5.1).

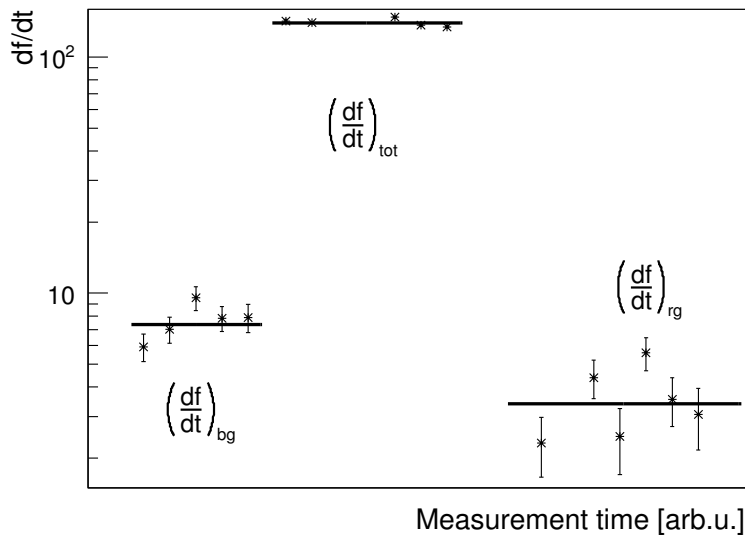


FIGURE 5.6: Example of frequency shift caused by the background when the target is on  $(\frac{df}{dt})_{bg}$  (left) and when the target is off  $(\frac{df}{dt})_{rg}$  (right) compared to the total frequency shift  $(\frac{df}{dt})_{tot}$  with the beam incident on the target (middle).

Finally, the frequency shift caused purely by beam-target interaction is calculated as:

$$\left(\frac{df}{dt}\right)_{tar} = \left(\frac{df}{dt}\right)_{tot} - \left(\frac{df}{dt}\right)_{bg} \quad (5.10)$$

where  $(\frac{df}{dt})_{tot}$  is the total frequency shift during the measurement discussed in the previous section, and  $(\frac{df}{dt})_{bg}$  is the frequency shift caused by the residual gas of the COSY ring and effect from the ANKE cluster target.

### 5.1.2.4 Momentum compaction factor

After determining  $df/dt$ , only momentum compaction factor  $\alpha$  is needed to finalise the calculation of the target density  $n_t$  at all the beam energies, according to Equation 5.7 and 5.8. The  $\alpha$  studies at COSY were performed in the dedicated cycles with the target switched off by adjusting the strength of the COSY bending magnets by few parts per thousand.

If the changes are not very large there is a linear relationship between the relative revolution frequency shift  $\Delta f/f_0$  and the relative change in the field  $\Delta B/B_0$ , expressed as following:

$$\frac{\Delta f}{f_0} = \alpha \frac{\Delta B}{B_0}. \quad (5.11)$$

Larger values of  $\Delta B/B_0$  and  $\Delta f/f_0$  require higher orders term in Equation 5.11.

For the purposes of this experiment,  $|\Delta B/B_0| < 1\text{‰}$  range was fitted with polynomial of second order. Results of these measurements are shown on Figure 5.7 for 2.0 GeV and summarised for all energies in the Table ??

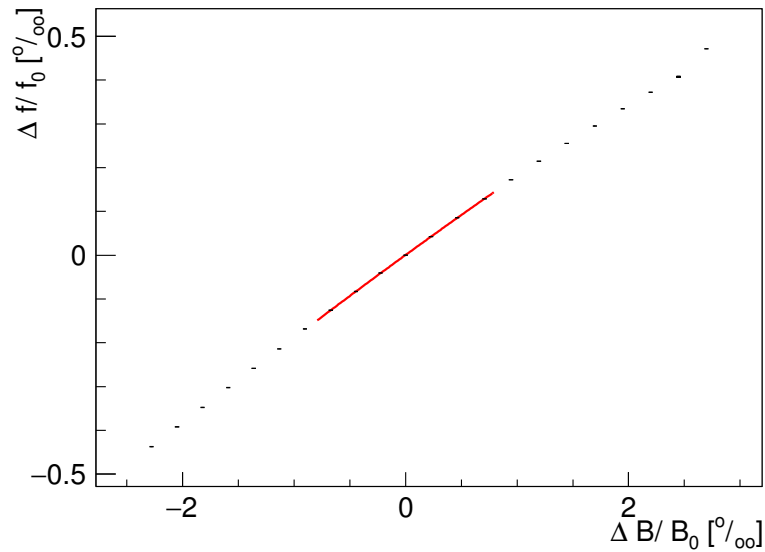


FIGURE 5.7: Variation of the mean revolution frequency with the field strength in the bending magnets for 2.0 GeV

### 5.1.2.5 Luminosity values

Summarise the average values of  $\alpha$ ,  $df/dt$ , BCT, L.

## 5.2 Event selection by FD

In order to determine cross section, besides luminosity counting rate  $R$  (Equation 5.2) of  $pp$  elastic scattering events must be measured. The events were selected by detecting a single fast proton in Forward Detector. The analysis of  $pp$  elastic scattering data from FD has been already discussed in the previous chapter. Therefore, in this section only the specifics of the cross section analysis will be discussed.

The trigger for the data acquisition system was initiated by a signal produced by the proton in either of two hodoscopes, placed one behind the other. This, together with a high efficiency of scintillation counter, reduced the trigger inefficiency to the  $10^{-4}$ .

The counter efficiency was studied by analysing the amplitude as a function of the vertical hit coordinate for the selected  $pp$  elastic events. Two kinds of angular acceptance cuts were applied: the equal  $|\phi| < 10^\circ$  cut for all polar angles, and  $|Y_{track}| < 10$  cm cut on the vertical coordinate in the D2 exit window. No sign of the amplitude falling below the threshold was observed, except for the first (closest to the beam pipe) counters in each hodoscope wall. The efficiency of each of MWPC's planes exceeds 97% [59].

The selected events produced a prominent peak in the missing mass spectrum, with a background of only 1-2%. A small contribution from the  $pp \rightarrow d\pi^+$  reaction to the peak region at 1 GeV was subtracted on the basis of the energy-loss information.

The setup parameters were adjusted in a geometry tuning procedure, with the use of the exclusive  $pp \rightarrow pp$ ,  $pp \rightarrow pn\pi^+$ ,  $pp \rightarrow pp\pi^0$ , and  $pp \rightarrow d\pi^+$  reactions. In the last case, both the  $d$  and  $\pi^+$  were detected in the FD and this gave valuable information on the systematic uncertainty of the transverse momentum reconstruction. These showed that any systematic shift in the determination of the c.m. angle in  $pp$  elastic scattering was less than  $0.15^\circ$ , which would correspond to a 0.5% change in the differential cross section.

Due to an apparent problem with the ramping of the COSY magnets, it was decided to cut off the data from first 60 seconds of data taking in every cycle. In this way, target density and event count rate were determined within the same time frame.

### 5.3 Systematic uncertainties

Table 5.1 lists identified contributions to the total systematic uncertainty of cross section at different proton beam energies  $T_p$ .  $E_1$  reflects the statistical and systematic effects in the determination of the Schottky  $\eta$  parameter.  $E_2$  arises from the rest gas effect (including direct measurement errors as well as possible instabilities).  $E_3$  is a measure of the density instability through the 300 s cycle. In addition, the 1.5 % accuracy of the stopping powers (taken from the NIST database [33]) and an estimate of the 1.5 % precision of the analysis of data taken with the FD have to be taken into account. These contributions have been added in quadrature to give the total percentage uncertainty, shown in the last column of Table 5.1. No single contribution is dominant, which means that it would be hard to reduce the systematic error to much below the 2.5–3.5% total uncertainty quoted in the table.

$T_p$ GeV	$E_1$ frequency-slip parameter [%]	$E_2$ residual gas [%]	$E_3$ target density instability [%]	Total [%]
1.0	1.6	0.7	0.7	2.8
1.6	1.2	1.9	1.4	3.4
1.8	1.3	1.6	1.6	3.4
2.0	0.8	1.9	1.8	3.5
2.2	0.3	1.0	1.0	2.6
2.4	0.4	1.5	1.6	3.1
2.6	0.4	1.5	1.5	3.0
2.8	0.9	1.2	0.5	2.6

TABLE 5.1: Percentage contributions to the total systematic uncertainty at different proton beam energies  $T_p$ .  $E_1$  reflects the statistical and systematic effects in the determination of the Schottky  $\eta$  parameter.  $E_2$  arises from the rest gas effect (including direct measurement errors as well as possible instabilities).  $E_3$  is a measure of the density instability through the 300 s cycle. These contributions have been added in quadrature with the accuracy of the stopping powers and the precision of the FD analysis to give the total percentage uncertainty in the last column.

### 5.4 Results and discussion

The results of the measured cross section as the function of the polar angle and the function of the four-momentum transfer  $t$  are summarised in Table C.1.

The variation of the obtained ANKE data can be seen most clearly in the differential cross section with respect to the four-momentum transfer  $t$  and these results

are shown in Figure 5.8. Also shown are exponential fits to the measured data made on the basis of

$$\frac{d\sigma}{dt} = A \exp(-B|t| + C|t|^2), \quad (5.12)$$

where the values of the resulting parameters are given in Table 5.2.

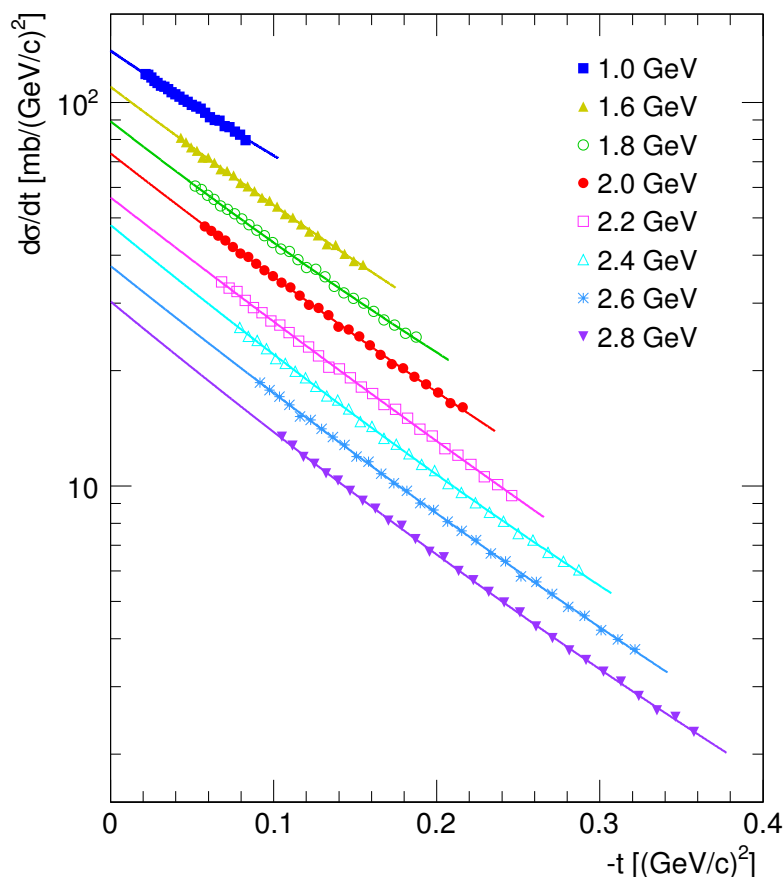


FIGURE 5.8: Combined ANKE data set of differential cross sections with respect to the four-momentum transfer  $t$  compared to fits made on the basis of Equation 5.12. Systematic errors are not shown. The correct values are shown at 1.0 GeV but, for clarity of presentation, the other data are scaled down sequentially in energy by factors of 1.2. The true numerical values of the cross section and fit parameters are given in Appendix C and Table 5.2, accordingly.

Taking  $C = 0$  at 1 GeV would change the value extracted from the fit by less than 1%, though this parameter becomes more important at higher energies where the  $t$  range is larger. This empirical representation of the measured data may prove helpful when the results are used in the normalisation of other experimental measurements.

### 5.4.1 Comparison with LNPI results at 1 GeV

There are very few data sets of absolute cross sections at small angles to which the ANKE results can be compared. In the vicinity of 1 GeV there are two measurements that were made with the IKAR recoil detector in the Leningrad Nuclear Physics Institute (LNPI). In the first of these at 992 MeV, IKAR used a hydrogen target [35]. In the second at 991 MeV a methane target was used, though the prime purpose of this experiment was to show that such a target gave consistent results and so could be used with a neutron beam [36].

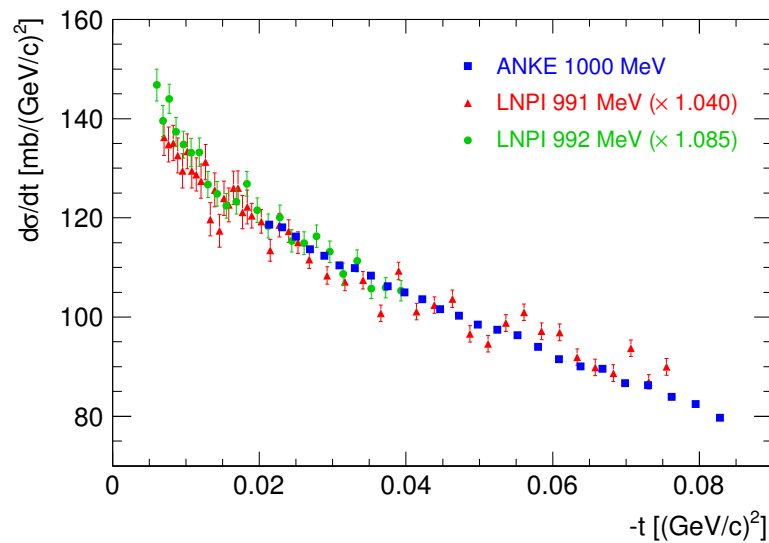


FIGURE 5.9: Invariant differential cross section for  $pp$  elastic scattering. The ANKE data at 1 GeV with statistical errors (blue squares) are compared to the IKAR (LNPI) hydrogen data at 992 MeV (green circles) [35] scaled by a factor of 1.085 and methane results at 991 MeV (red triangles) [37] scaled by a factor of 1.04. At very small values of  $|t|$  there is a rise caused mainly by Coulomb-nuclear interference.

The ratio of the IKAR hydrogen values [35] to the fit of the ANKE 1 GeV data over the common range of angles is  $0.920 \pm 0.005$ . In order to compare the shapes of these data sets, the LNPI results have been scaled by a factor of 1.085 before being plotted in Figure 5.9. The scaling factor is significant in view of the 2% and 2.8% absolute normalisations reported for the IKAR and ANKE experiments, respectively.

### 5.4.2 Comparison with ANL results at 2.0 and 2.8 GeV

Data are also available from the Argonne National Laboratory (ANL) in our angular range at 2.2 and 2.83 GeV [38] and these values are plotted together with our

measurements in Figure 5.10. The ANL data sets agree with our 2.2 and 2.8 GeV results to within 1%. However, the absolute normalisation claimed for these data was 4% [38] so that it is not possible to draw completely firm conclusions from this comparison.

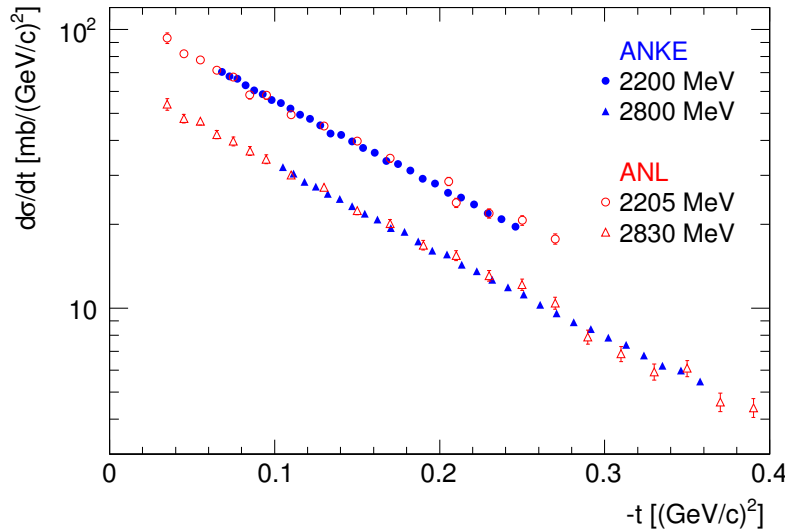


FIGURE 5.10: The ANKE  $pp$  differential cross section data at 2.2 GeV (closed blue circles) and 2.8 GeV (closed blue triangles) compared to the ANL results [38] at 2.2 GeV (open red circles) and 2.83 GeV (open red triangles). Systematic errors are not shown. For presentational purposes, both higher energy data sets have been scaled downwards by a common factor of 1.5.

### 5.4.3 Impact on the SAID solution

The results obtained at ANKE could clearly have an impact on the current partial wave solutions. This is demonstrated in Figure 5.11, where the ANKE cross sections at 1.0, 2.0, and 2.8 GeV are compared to both the SAID 2007 solution [6] and a modified one [30] that takes the present data at all eight energies into account. Scaling factors in the partial wave analysis, consistent with the overall uncertainties given in Table 5.1, have been included in the figure. The major changes introduced by the new partial wave solution are in the  $^1S_0$  and  $^1D_2$  waves.

The precise EDDA measurements were undertaken for c.m. angles of  $35^\circ$  and above whereas the ANKE data finish well below this and the gap looks even bigger in terms of the momentum-transfer variable  $t$ . Nevertheless, the modified SAID solution shown in Figure 5.11 fits the ANKE 1 GeV cross section reduced by 3% and describes also the EDDA data at 1.0144 GeV [39]. Such a 3% reduction in the

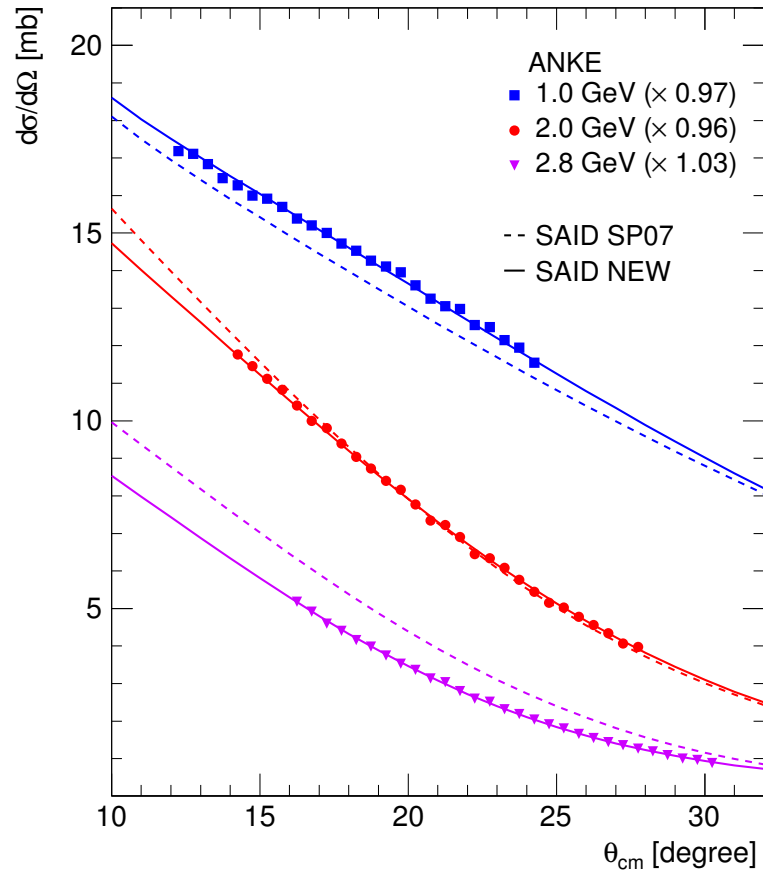


FIGURE 5.11: Scaled ANKE proton-proton elastic differential cross sections at 1.0, 2.0, and 2.8 GeV with statistical errors compared to the SAID 2007 solution [6] and a modified (“new”) partial wave solution where the ANKE data have been taken into account. For presentational reasons the 2.0 and 2.8 GeV data and curves have been reduced by factors of 0.5 and 0.25, respectively. The best agreement with the new partial wave data was achieved by scaling the ANKE data with factors 0.97, 0.96, and 1.03 at the three energies. Such factors are within the uncertainties given in Table 5.1.

ANKE normalisation at this energy is consistent with the results of a combined fit of (Equation 5.12) to the EDDA and the Coulomb-corrected ANKE data.

In the forward direction the number of proton-proton elastic scattering amplitude reduces from five to three and the imaginary parts of these amplitudes are determined completely by the spin-averaged and spin-dependent total cross sections with the help of the generalised optical theorem. The corresponding real parts have been estimated from forward dispersion relations, where these total cross sections provide the necessary input [40]. All the terms contribute positively to the value of  $A(GK)$  and, using the optical theorem, the lower bound,

$$A \geq (\sigma_{tot})^2/16\pi, \quad (5.13)$$

is obtained by taking the  $pp$  spin-averaged total cross section  $\sigma_{\text{tot}}$ . This lower bound and the full Grein and Kroll estimates for  $A$  [40] are both shown in Figure 5.12 where, for consistency, the same values of  $\sigma_{\text{tot}}$  were used in the two calculations.

$T_p$ GeV	$A$ $\frac{\text{mb}}{(\text{GeV}/c)^2}$	$B$ $(\text{GeV}/c)^{-2}$	$C$ $(\text{GeV}/c)^{-4}$	$A(\text{Corr.})$ $\frac{\text{mb}}{(\text{GeV}/c)^2}$	$A(\text{GK})$ $\frac{\text{mb}}{(\text{GeV}/c)^2}$
1.0	$136.4 \pm 1.3 \pm 3.8$	$6.7 \pm 0.4$	$4.0 \pm 3.8$	$136.7 \pm 3.8$	135.2
1.6	$131.7 \pm 1.9 \pm 4.5$	$7.4 \pm 0.3$	$2.7 \pm 1.7$	$131.1 \pm 4.5$	128.9
1.8	$128.6 \pm 1.7 \pm 4.4$	$7.6 \pm 0.2$	$3.4 \pm 1.0$	$127.6 \pm 4.3$	125.7
2.0	$127.3 \pm 1.7 \pm 4.5$	$7.7 \pm 0.2$	$2.5 \pm 0.8$	$124.0 \pm 4.3$	123.1
2.2	$117.2 \pm 1.8 \pm 3.0$	$7.6 \pm 0.2$	$1.4 \pm 0.7$	$113.1 \pm 2.9$	120.9
2.4	$119.2 \pm 1.8 \pm 3.7$	$8.0 \pm 0.2$	$2.7 \pm 0.5$	$112.8 \pm 3.5$	118.5
2.6	$111.9 \pm 1.7 \pm 3.4$	$7.8 \pm 0.2$	$2.0 \pm 0.4$	$108.8 \pm 3.3$	116.0
2.8	$108.5 \pm 1.8 \pm 2.8$	$8.1 \pm 0.2$	$2.4 \pm 0.4$	$105.0 \pm 2.7$	113.6

TABLE 5.2: Parameters of the fits of (Equation 5.12) to the differential cross sections measured in this experiment. In addition to the statistical errors shown, the second uncertainty in the value of  $A$  in the second column represents the combined systematic effects summarised in Table 5.1. The corrected values of the forward cross section,  $A(\text{Corr.})$ , were obtained using the SAID fit discussed in the text, the associated error bars being purely the systematic ones listed in Table 5.1. These values, which were not subjected to the SAID normalisation factors applied in Figure 5.11, may be compared with those of  $A(\text{GK})$ , which were determined using the Grein and Kroll forward amplitudes [40].

The 992 MeV IKAR data of Figure 5.9 show a significant rise at small  $|t|$  that is a reflection of Coulomb distortion of the strong interaction cross section and this was taken into account through the introduction of explicit corrections [35]. The corrected data were then extrapolated to the forward direction ( $t = 0$ ), using a simple exponential function, which would correspond (Equation 5.12) with  $C = 0$ . The resulting points at all the energies studied are generally about 10% below the Grein and Kroll predictions [40] and would therefore correspond to smaller real parts of the spin-dependent amplitudes. The extrapolation does, of course, depend upon the Coulomb-corrected data following the exponential fit down to  $t = 0$ .

Though the ANKE data do not probe such small  $|t|$  values as IKAR LNPI [35], and are therefore less sensitive to Coulomb distortions, these effects cannot be neglected since they contribute between about 1.5% and 4.5% at 1.0 GeV though less at higher energies.

It is seen in Figure 5.11 that modified SAID solutions describe well the ANKE measurements at three typical energies and the same is true also at the energies not shown. After fitting the ANKE measurements, there is a facility in the SAID

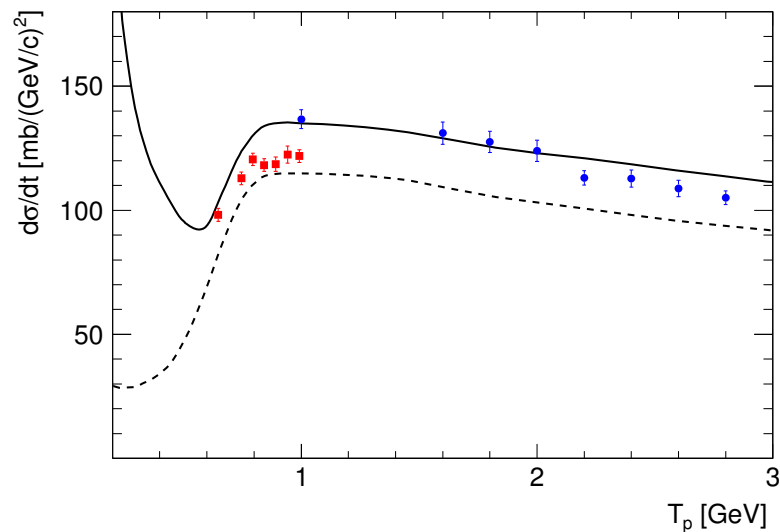


FIGURE 5.12: The predictions of Grein and Kroll [40] for the values of the forward  $pp$  elastic differential cross section (solid line), the corresponding lower limit provided by the spin-independent optical theorem of (Equation 5.13) being indicated by the broken line. The extrapolated ANKE data, corresponding to the  $A(\text{Corr.})$  parameter of Table 5.2, are shown with their quoted errors by the (blue) circles, whereas the (red) squares are the published IKAR values [35].

program for switching off the Coulomb interaction without adjusting the partial wave amplitudes [6] and this allows a robust extrapolation of the Coulomb-free cross section to the forward direction. The approach has the advantage that it includes some of the minor Coulomb effects that are contained in the SAID program [41][42]. It takes into account the phase variations present in the partial wave analysis and also the deviations from exponential behaviour for very small momentum transfers,  $|t| \lesssim m_{\pi^0}^2 = 0.018 \text{ (GeV}/c)^2$ , that are linked to pion exchange. The values for  $A(\text{Corr.})$  at  $t = 0$  produced in this way are given in Table 5.2 and shown in Figure 5.12. The error bars are purely the systematic uncertainties listed in Table 5.1 and any errors in the angular dependence of the SAID predictions are neglected.

The corrections obtained using the SAID program with and without the Coulomb interaction at 1 GeV are a little larger than those found by the LNPI group using an explicit Coulomb formula [35], in part due to the different relative real parts of the  $pp$  amplitude in the two calculations.

The agreement of the ANKE data with the theoretical curve in Figure 5.12 is encouraging and would be even slightly better if the normalisation factors found in the fits to the cross sections in Figure 5.11 were implemented. Nevertheless,

the extrapolated values generally fall a little below the predictions at the higher energies.

## 5.5 Conclusion

In summary, we have measured the differential cross sections for proton-proton elastic scattering at eight energies between 1.0 and 2.8 GeV in a c.m. angular domain between about  $12^\circ$ – $16^\circ$  to  $25^\circ$ – $30^\circ$ , depending on the energy. Absolute normalisation of typically 3% were achieved by measuring the energy loss of the beam as it traversed the target. After taking the Coulomb distortions into account, the extrapolations to the forward direction, are broadly compatible with the predictions of forward dispersion relations.

Although our results are completely consistent with ANL measurements at 2.2 and 2.83 GeV [38], the published IKAR values [35] are lower than ours at 1 GeV by about 8%, though this would be reduced to about 5% if one accepts the renormalisation factor from the SAID fit shown in Figure 5.11.

The new ANKE data have a significant influence on a partial wave analysis of the  $pp$  elastics scattering. In the modified SAID solution, the  $^1S_0$  and  $^1D_2$  waves in particular significantly change at high energies (Figure 5.13). On a more practical level, the measurements will also be a valuable tool in the normalisation of other experiments.

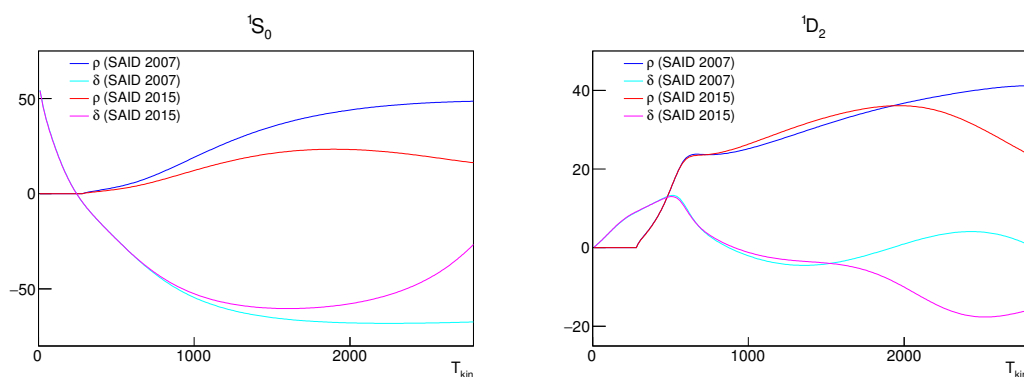


FIGURE 5.13: Phase shifts for  $^1S_0$  and  $^1D_2$  partial waves from the 2015 SAID solution [30], in comparison with the older solution from 2007 [5].

## Chapter 6

# Analysing power in proton-neutron quasi-free elastic scattering

The analysing power in  $\vec{p}n$  quasi-free elastic scattering has been measured at small angles at COSY-ANKE using polarised proton beam at 0.796 GeV and five other beam energies between 1.6 and 2.4 GeV incident on the unpolarised deuteron cluster-jet target. The use of deuterium as an effective neutron target is possible because of the small binding energy of the deuteron (about 2.2 MeV). Consideration of the quasi-free elastic scattering is based on the assumption that the incoming particle is being scattered by only one of two nucleons in the deuteron, while no momentum is transferred to the second nucleon (this nucleon acts as a spectator). In general, the quasi-free scattering is considered to be realized when the momentum transfer from a beam particle to a scattered one ( $P_t$ ) is large enough as compared with the spectator particle momentum ( $P_{sp}$ ). Unfortunately, no neutron detection system is available at ANKE-COSY, and hence, no direct measurement of the scattered neutron is possible. The asymmetries of  $\vec{p}n$  quasi-free elastic scattering were obtained from the coincidence events, where the fast proton is detected in the ANKE Forward Detector (FD) and the slow spectator proton in a silicon tracking telescope (STT).

This chapter will describe the details of the analysis, unique for the quasi-free elastic scattering studies at ANKE.

## 6.1 Beam polarisation

Similar to  $\vec{p}p$  elastic scattering experiment, in  $\vec{p}d$  measurements the beam polarisation was reversed every subsequent cycle. For each polarisation mode cycles of 180 s or 300 s duration were used, with the last 20 s of each cycle being reserved for the measurement of the beam polarisation with the EDDA detector. The measurement of the proton beam polarisation for the runs with deuteron target followed the same steps as for  $\vec{p}p$  ANKE experiment, discussed in Section 4.1.

The weighted averages of the beam polarisations determined over all data at six beam energies are given in Table 6.1. The changes in sign reflect the number of spin flips required to pass through the imperfection resonances, described in detail in Section 3.1.2. The COSY settings for each of the six kinetic energies of the beam were prepared independently and, for this reason, the magnitude of the polarisation may not decrease monotonically with increasing value of the beam energy.

$T_p$ (GeV)	0.796	1.6	1.8	1.965	2.157	2.368
$P$	0.511	0.378	-0.508	-0.476	-0.513	0.501
$\Delta P$	$\pm 0.001$	$\pm 0.001$	$\pm 0.003$	$\pm 0.005$	$\pm 0.005$	$\pm 0.004$

TABLE 6.1: The values of the mean polarisations  $P$  determined with the EDDA polarimeter averaged over all the data at the beam energy  $T_p$ .

The variation of the beam polarisation values among the cycles at any given energy was checked using EDDA with various selections and combinations of the cycles. All the studies yield the consistent results within the uncertainties at any given energy.

## 6.2 Event selection

Neutron detection is not possible using the ANKE detection system. Therefore, in order to select quasi-free elastic scattering events in the ANKE experiment one proton is measured in STT in coincidence with the fast proton detected in FD. The simulation has been performed to estimate the rate of  $pp$  and  $pn$  quasi-free scattering within the layout of the ANKE detectors. Figure 6.1 shows the simulated acceptance of  $pd \rightarrow ppn_{sp}$  and  $pd \rightarrow pnp_{sp}$  reactions. The example is shown for beam kinetic energy  $T_p = 0.796$  GeV.

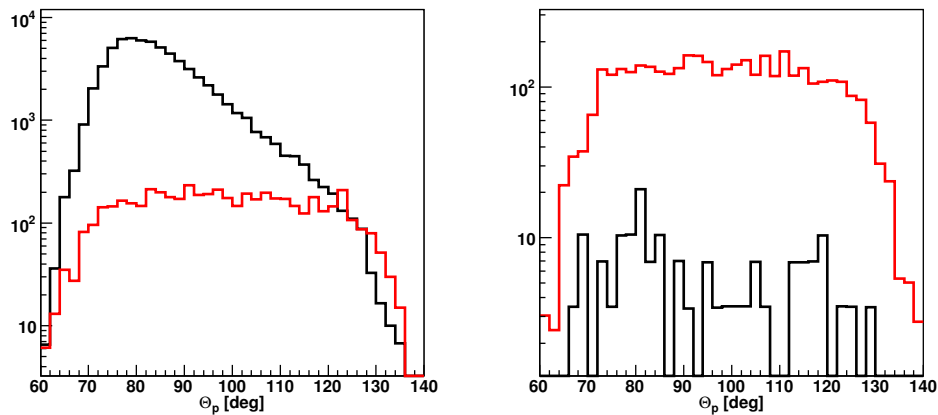


FIGURE 6.1: The acceptance  $pd \rightarrow ppn_{sp}$  (black histograms) and  $pd \rightarrow pnp_{sp}$  (red histograms) reactions simulated in the framework of spectator model at  $T_p = 0.796$  GeV. One proton is detected in the FD and other one in the STT1 (left panel) or in the STT2 (right panel).

The simulation has demonstrated that the  $pp$  quasi-elastic scattering is kinematically suppressed in STT2 due to FD being an one-arm detector. Therefore, all the coincidence events of proton detected in STT2 and FD are assumed to belong to  $pn$  quasi-free elastic scattering. Namely, the proton detected in the STT2 is assumed to be “spectator” one, whereas the particle detected in the FD is regarded as a proton, scattered elastically on a quasi-free neutron.

The proton momentum reconstruction in STT and FD followed the same steps as described in Chapter 4. The STTs detect protons with energy threshold of 2 MeV, corresponding to the momentum  $P_p > 70 MeV/c$ . This momentum of spectator proton should be smaller than momentum transfer for the spectator model to be applicable. The careful handling of the data within the spectator model scenario is discussed in greater detail in Section 6.5.

The quasi-free  $pn$  elastic scattering events are identified through the evaluation of the missing mass in the  $pd \rightarrow ppX$  reaction. As can be seen from the typical example shown in Figure 6.2 at a beam energy of 2.157 GeV, the missing mass peak is well positioned at the neutron mass. The upper limit of the background estimation (details in Section. 6.4) is small compared with the statistical errors of the analysing power.

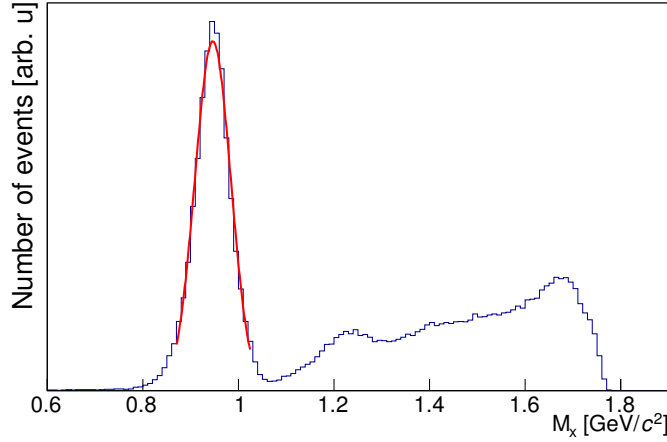


FIGURE 6.2: Missing-mass  $M_X(pp \rightarrow ppX)$  spectra obtained for a beam energy of 2.157 GeV. The peak is consistent with the neutron mass value.

### 6.3 Asymmetry determination

Since the FD is a single-arm detector, the analysing power for the quasi-free elastic scattering has to be calculated from the simple asymmetries of counts corresponding to different orientations of the beam polarisation. The deuterium cluster target was unfortunately not very stable during this experiment causing large variation of the luminosity (beam-target overlap). Hence, the dedicated normalisation procedure had to be prepared.

In this case the asymmetry is introduced as

$$\varepsilon(\theta) = \frac{N^\uparrow(\theta)/N_{norm}^\uparrow - N^\downarrow(\theta)/N_{norm}^\downarrow}{N^\uparrow(\theta)/N_{norm}^\uparrow + N^\downarrow(\theta)/N_{norm}^\downarrow} \quad (6.1)$$

in terms of normalised numbers of counts for the two orientations of the beam polarisation. As was discussed in Chapter 5, the normalisation factor must be chosen in such a way, that it does not depend on the beam polarisation. For the given analysis, normalisation factor  $N_{norm} = kN_{d1} + N_{d2}$  was constructed from the number of deuterons detected in the STT1 ( $N_{d1}$ ) and the STT2 ( $N_{d2}$ ). The polarisation influence can be cancelled in the  $N_{norm}$ , if one requires

$$\frac{kN_{d1}^\uparrow - N_{d2}^\uparrow}{kN_{d1}^\uparrow + N_{d2}^\uparrow} = \frac{N_{d2}^\downarrow - kN_{d1}^\downarrow}{N_{d2}^\downarrow + kN_{d1}^\downarrow}. \quad (6.2)$$

The equalising coefficient  $k$  is, hence, determined as

$$k = \sqrt{\frac{1}{(N_{d1}^\uparrow/N_{d2}^\uparrow)(N_{d1}^\downarrow/N_{d2}^\downarrow)}} = \sqrt{\frac{N_{d2}^\downarrow N_{d2}^\uparrow}{N_{d1}^\uparrow N_{d1}^\downarrow}} = \frac{N_2}{N_1}. \quad (6.3)$$

This approach is based on the several assumptions, including acceptance stability, equality of polarisation values for two modes  $|P_\uparrow| = |P_\downarrow|$ , and constant ratio of dead times for the different triggers.

### 6.3.1 Normalisation via proton-deuteron elastic scattering

It was possible to check the proposed normalisation procedure by comparison with proton-deuteron elastic scattering asymmetry obtained via the cross-ratio method. As was explained in Chapters 2 and 4, the cross-ratio method provides precision results without the first order systematic uncertainties. The cross-ratio asymmetry was measured using stopped deuterons that were identified in STTs. Similar to  $\vec{p}p$  analysis, the angles of the stopped deuterons were deduced from the energy deposits measured in the three layers of the STT rather than from a direct angular measurement.

We have calculated the left-right asymmetry of the deuterons scattered to STTs in each polar angular interval as

$$\varepsilon(\theta) = \frac{L(\theta) - R(\theta)}{L(\theta) + R(\theta)} \quad (6.4)$$

from the geometrical means of number of particles scattered in the given polar angle interval to the left  $L$  and particles scattered in the same angle interval, but to the right  $R$  in respect to the beam polarisation. The results for the asymmetry calculated via the cross-ratio method are compared to the simple left-right asymmetry calculated using the new normalisation procedure in Figure 6.3. The good agreement of the asymmetries shown in Figure 6.3 confirms the validity of the proposed normalisation procedure.

Using the polarisation values from Table 6.1, the proton analysing power  $A_y^p$  in proton-deuteron elastic scattering was obtained at all six energies. The ANKE data at 0.796 GeV agree with SATURN measurements [43] within the systematic error bars. Besides providing the normalisation check, these data, summarised in the Figure 6.4 and Appendix D, can be used independently in other polarised experiments or as an input to theoretical models.

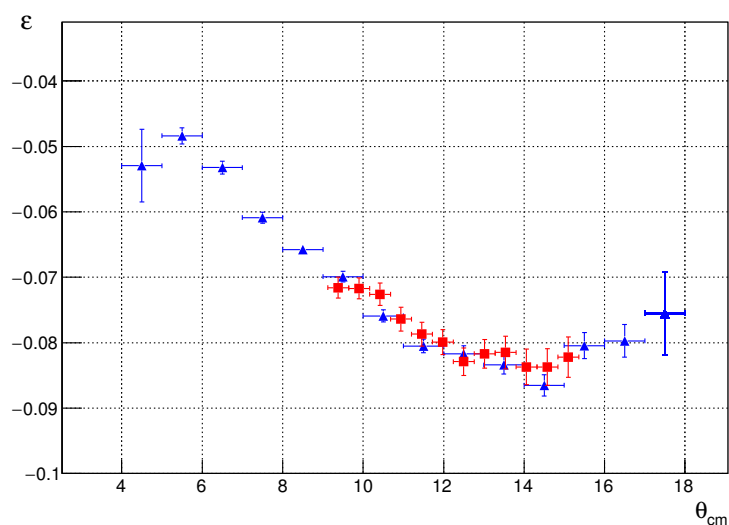


FIGURE 6.3: Comparison of the  $pd$  elastic scattering asymmetries at  $T_p = 1.965$  GeV obtained in two different ways: blue triangles stand for the cross-ratio method; red squares correspond to the simple left-right asymmetry, using the normalisation procedure described in the text.

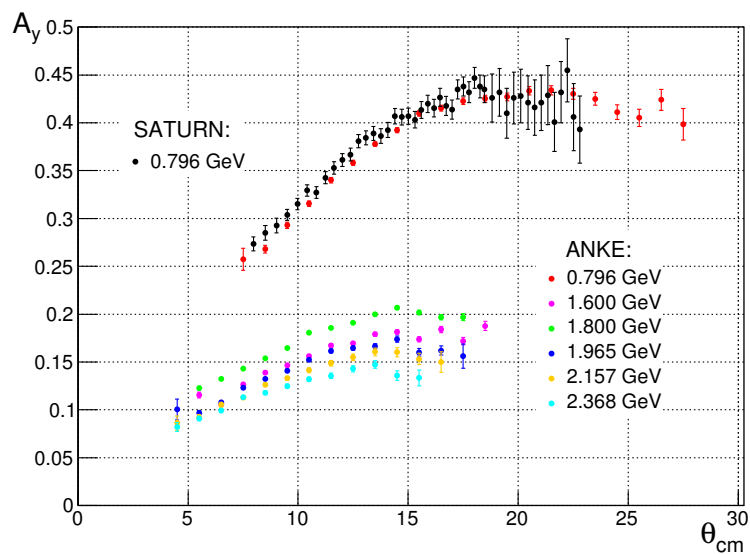


FIGURE 6.4: Analysing power in  $pd$  elastic scattering, along with the existing experimental data from SATURN at 0.796 GeV [43]. ANKE results include statistical errors only.

## 6.4 Background correction

As seen in Figure 6.2, there is some background under neutron peak in the missing mass distribution. In case the background does not depend on the beam polarisation, the true value of the asymmetry  $\varepsilon_{true}$  can be calculated as

$$\varepsilon_{true} = \varepsilon_{meas}(1 + N_{bg}/N_0) \equiv \varepsilon_{meas}(1 + k_{bg}) \quad (6.5)$$

where  $N_{bg}$  is the background count within the chosen range of kinematic variables, and  $N_0$  is the count related to the unpolarised cross section within the same range.

To check the validity of the background correction via Equation 6.5, the difference of missing mass distributions for different beam polarisation orientations was studied. The missing mass spectra for every cycle were normalised by number of elastic deuterons ( $N_{norm}$ ). Then all normalised distributions obtained at the same beam polarisation mode were summed up with the proper error recalculation. The number of the selected cycles with the beam polarisation up ( $\uparrow$ ) and the beam polarisation down ( $\downarrow$ ) may not necessary be the same. Hence, the further correction for the number of cycles should be undertaken for the final difference of missing mass spectra. As seen in Figure 6.5, contributions of the unpolarised counts are indeed cancelled in such a distribution. The difference of neutron peaks can be fitted by Gaussian, with no background in the vicinity. Similar figures at other energies prove that there is no polarised background and Equation 6.5 can be used for the asymmetry correction.

The true asymmetry should not change among various  $M_x$  ranges within the neutron peak, hence it should be possible to roughly estimate the background effect from comparison of the measured asymmetry for different  $M_x$  ranges. The large statistical errors, however, do not allow to estimate only very roughly the upper limit of  $k_{bg}$  to be 0.05-0.07 within the  $\pm 2\sigma$  range.

For more precise estimation on  $k_{bg}$ , two background shape hypotheses were investigated: polynomial (Figure 6.6 upper panel) and polynomial + Gaussian (Figure 6.6 lower panel). The sum of normalised missing mass spectra at 1.8 GeV, fit with Gaussian (centered at neutron mass) and background of different shapes, are shown in Figure 6.6 by black curve. Red dashed curves represent the polynomial approximation for the background, the green dashed curve represents the polynomial + Gaussian with  $m_x \approx 0.86 \text{ GeV}/c^2$ . The polynomial background does not describe well the tail on the left side of the neutron peak, but the central part of

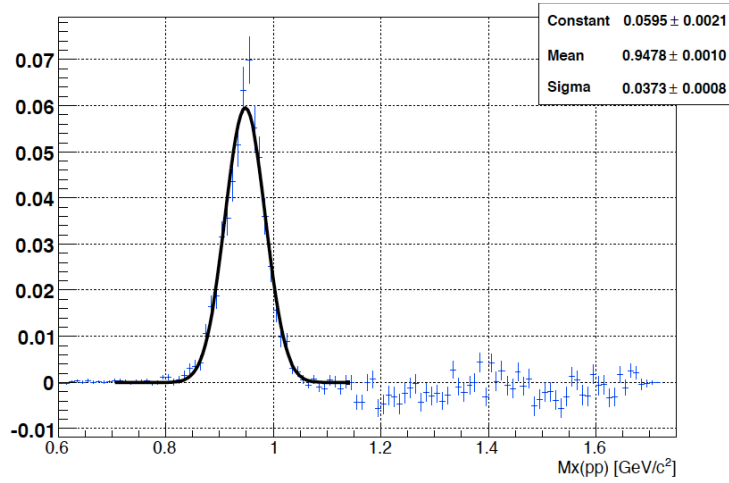


FIGURE 6.5: The difference of normalised missing mass distributions for two polarisation modes at 1.8 GeV.

the n-peak is described very well within the  $1.5 - 2 \sigma$ . Hence, even if we consider an additional Gaussian, that helps to describe the left side of the peak, the contribution to the central part is negligible. As a result, both background shapes would give close values of  $k_{bg}$  of 0.03 for polynomial, and 0.026 for polynomial + Gaussian shapes.

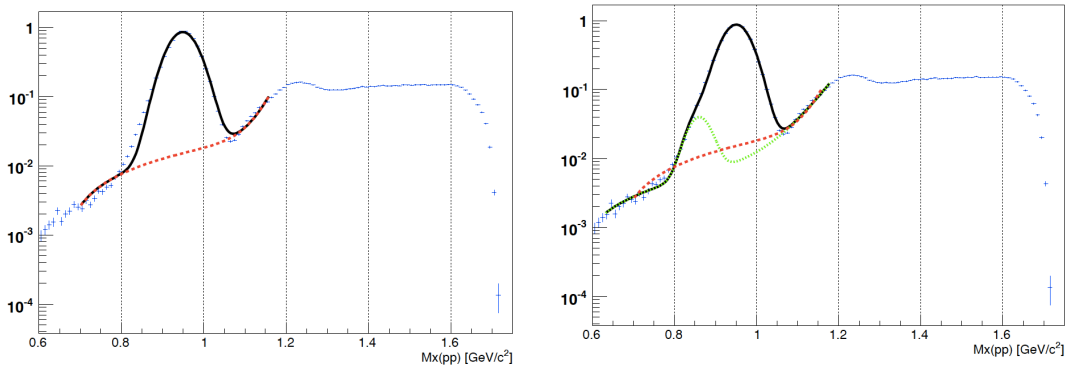


FIGURE 6.6: The sum of normalised missing mass spectra at 1.8 GeV (blue points), fit with Gaussian and background of different shapes (black curve). Red dashed curves represent the polynomial approximation for the background, the green dashed curve represents the polynomial + Gaussian with  $m_x \approx 0.86 \text{ GeV}/c^2$ .

## 6.5 Validity of spectator model

The analysis in the first approximation, when all the coincidence events of protons detected in FD and in STT2 are assumed to belong to  $pn$  quasi-free elastic scattering, yields the results that are consistent with the existing SAID solution and experimental data at 0.796 GeV. However, the Figure 6.7 shows that the acceptance of the ANKE detection systems in terms of the  $P_{sp}/P_t$  ratio spans from 0.3 up to 1.6, where spectator model is not supposed to be valid. Indeed, the

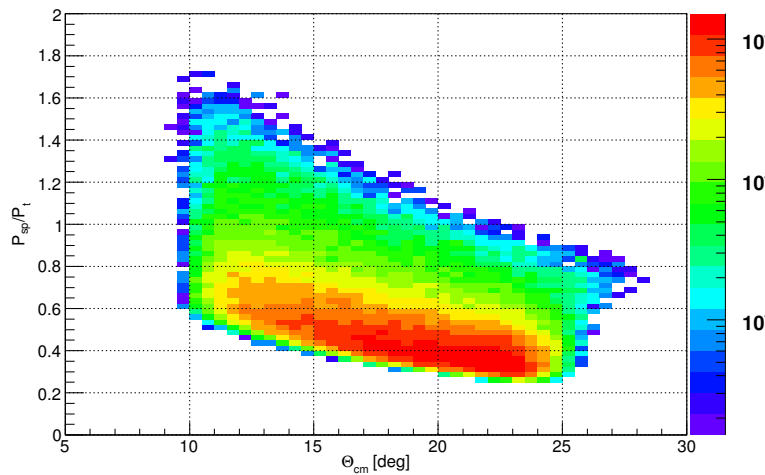


FIGURE 6.7: The ANKE acceptance in terms of the  $P_{sp}/P_t$  ratio dependence on c.m. the scattering angle at the beam energy of  $T_p = 796$  GeV.

more careful analysis showed the dependence of the analysing power on the  $P_{sp}/P_t$  ratio. It is seen from Figure 6.8 that at least  $P_{sp}/P_t < 0.6$  cut is necessary for the analysis at  $T_p = 0.796$  GeV. Therefore, the careful handling of the data within the spectator model scenario is necessary.

The following studies on this matter have shown that to separate quasi-free scattering another cut of  $P_t < 200$  MeV/ $c$  is necessary. The underlying reasons are not entirely clear yet and the investigations are undergoing.

### 6.5.1 Quasi-free elastic proton-proton scattering

The analysing power in proton-proton elastic scattering offers an interesting possibility for the study of the applicability of the spectator model cuts applied for proton-neutron quasi-free elastic scattering. Namely, we can identify the quasi-free  $pp$  elastic scattering via detecting slow proton in STT and fast proton in FD.

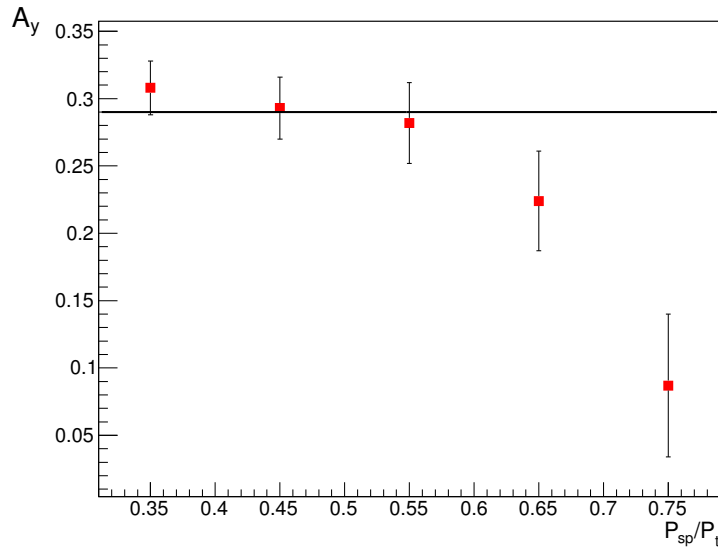


FIGURE 6.8: Analysing power dependence on the  $P_{sp}/P_t$  ratio at the kinetic beam energy  $T_p = 0.796$  GeV.

Applying the same cuts as towards  $pn$  quasi-free elastic scattering, we can compare the analysing power  $A_y$  in quasi-free  $pp$  to the  $A_y$  obtained in free  $pp$  elastic scattering (Chapter 4). The results are shown in Figure 6.9 at 0.796 GeV (upper panel) and 1.6 GeV (lower panel). The results at the higher energies could not be retrieved in the acceptance of the ANKE setup. First of all, detecting both scattered protons in STT and FD allows to get closer to the spectator model, because there is no  $P_{sp} < 70$  MeV/ $c$  limit anymore. The points in red depict the result of the analysis without any cuts on the  $P_{sp}/P_t$  ratio. The green triangles are the result of the same cut procedure ( $P_{sp}/P_t < 0.5$  and  $P_t > 200$  MeV/ $c$ ) as for  $pn$  analysis. Finally, blue empty symbols show the  $pp$  elastic data: circles stand for data obtained from STT and squares - from FD.

The analysis of the quasi-free  $pp$  elastic events proves the justification of the applied cuts within this work. However, the reasons underneath the cuts are not completely understood and are still to be studied in detail. This demonstrates that  $pn$  data at 0.796 GeV in the angular range between  $18^\circ$  and  $23^\circ$  indeed corresponds to the quasi-free scattering within the applied cuts. The higher energies are influenced much less by the applied cuts, because already for 1.6 GeV the transfer momentum is higher than 180 MeV/ $c$ .

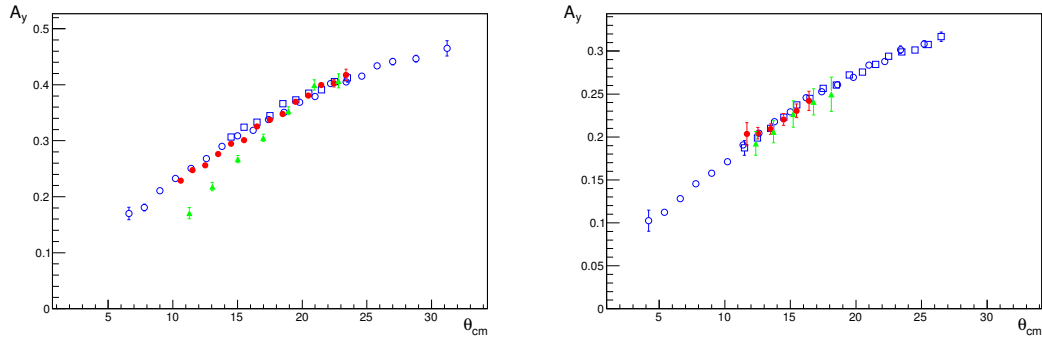


FIGURE 6.9: Analysing power in  $pp$  quasi-free elastic scattering without any cuts (red points), with the same cuts as for  $pn$  quasi-free elastic scattering (green triangles), compared to the analysing power obtained from free proton-proton elastic scattering at ANKE: FD (blue empty squares) and STT (blue empty circles). The results are shown at 0.796 GeV (upper panel) and 1.6 GeV (lower panel).

## 6.6 Results and Discussion

The results of the  $A_y$  measurements at ANKE for  $pn$  quasi-elastic scattering are shown in Figure 6.10. The SAID SP07 solution [5], which is only valid up to 1.3 GeV kinetic energy, is shown by the solid black line at the  $T_p = 0.796$  GeV in Figure 6.10. This energy was specifically chosen for the comparison with the existing data [44–47] and SAID solution [5]. After the appropriate cuts, that ensure the quasi-free scattering, the analysing power in proton-neutron quasi-free elastic scattering could have been obtained. The agreement between the new ANKE data and other existing data at 0.796 GeV and also with the SAID 2007 prediction is very good.

The higher energies, which were the main purpose of this experiment, has even better acceptance towards the proton-neutron quasi-free elastic scattering, resulting in the precision data in the non-explored angular and energy region. Results for the higher energies presented in Figure 6.10 were obtained using the data with the cut of  $P_{sp}/P_t < 0.4$ . This cut does not drastically decrease the available statistics because the FD acceptance for larger  $P_{sp}/P_t$  ratio is small. At 1.6 GeV the loss of statistics due to the limit on the  $P_{sp}/P_t$  is about 25 %, and it goes down with increasing of beam energy. Excluding the 1.6 GeV beam energy, presented results involve more than 95% of the total available statistics we have collected.

Another confirmation of the high quality of the obtained data is an overlap with the existing data from ANL is at 2.2 GeV [48, 49]. The ANKE data points are

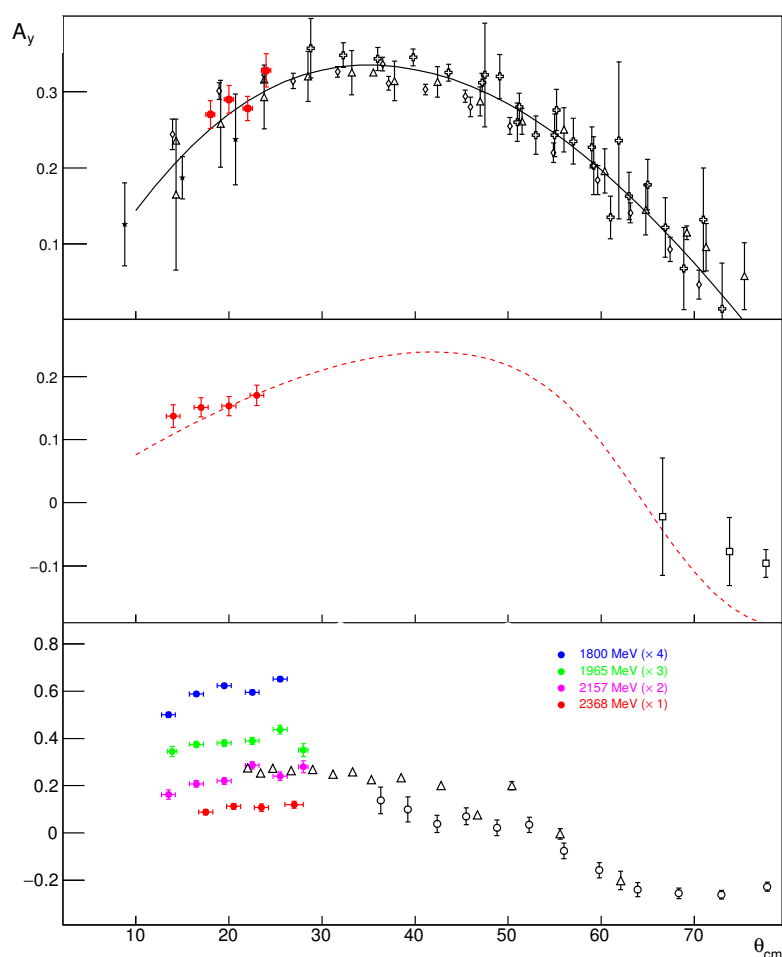


FIGURE 6.10: ANKE measurements of the analysing power in  $pn$  quasi-elastic scattering (filled circles). The results at 0.796 GeV (upper panel) are compared with the curves corresponding to the SAID 2007 prediction (solid black line) [6] and other existing measurements (black open symbols) [44–47]. The preliminary SAID solution for analysing power in  $pn$  quasi-free elastic scattering at beam kinetic energy  $T_p = 1.6$  GeV is shown in the middle panel in red dashed curve along with the ANKE and SATURN measurements at this energy. For the ease of presentation, the scaled ANKE data at other 4 energies are given in the lower panel. Also shown are the results from Argonne National Laboratory at 2.2 GeV energy [48, 49] (black open symbols). Only statistical errors are shown.

in a good agreement with ANL data in the overlapping region, and reasonably continue the angular dependence at the smaller angles.

In Figure 6.10 (lower panel) all the results obtained at ANKE at higher energies are summarised. The absolute values are shown at 2.368 GeV, but for clarity of presentation, the other data are scaled up sequentially with the decreasing energy. The scaling factors are given in the legend. The systematic errors, not shown in the figure, include the uncertainties of the determination of the beam polarisation in the EDDA polarimeter.

Using our and other recent data (including WASA-COSY experimental measurements at 1.3 GeV) the SAID group was able to provide the preliminary solution for  $pn$  quasi-elastic scattering at 1.6 GeV (shown in black in Figure 6.10 middle panel), extending the PWA range from previously published 1.3 GeV.

## 6.7 Conclusion

We have measured the analysing power in the proton-neutron quasi-free elastic scattering using proton polarised beam at six energies  $T_p = 0.796, 1.6, 1.8, 1.965, 2.157, 2.368$  GeV and deuteron unpolarised target. It was possible to show that spectator model could be used in the given experiment.

The ANKE measurements of the analysing power in the proton-neutron quasi-free elastic scattering at beam kinetic energy of 0.796 GeV are consistent with the older experimental data and SAID solution. Furthermore, it was possible to compare the new ANKE measurements with the ANL data at 2.157 GeV, resulting in a good agreement. This further proves the quality of the data at small angles at 5 new energies in the range from 1.6 to 2.4 GeV. This is an important input in the very scarce  $pn$  quasi-free elastic scattering data base. Increasing of the energy range of PWA for  $pn$  up to 1.6 GeV has been performed by the SAID group. The shown curve is still only preliminary, the corresponding publication is being prepared for the submission [30].



## Chapter 7

### Summary and outlook

#### 7.1 Impact on partial wave analysis

The presented measurements have an important impact on the phase shift analysis since they represent a precise and consistent data set.



## Appendix A

### Angular ranges of EDDA semi-rings

Ring Number	$\Delta\theta_{lab}$
14	42.7° ... 36.9°
15	39.8° ... 34.1°
16	36.9° ... 31.5°
17	34.1° ... 28.9°
18	31.5° ... 26.5°
19	28.9° ... 24.2°
20	26.5° ... 22.1°
21	24.2° ... 20.1°
22	22.1° ... 18.3°
23	20.1° ... 16.6°
24	18.3° ... 15.0°
25	16.6° ... 13.6°
26	15.0° ... 12.3°
27	13.6° ... 11.1°
28	12.3° ... 10.1°
29	11.1° ... 9.9°

TABLE A.1: Laboratory angle ranges, corresponding to EDDA rings, in the coordinate system, associated with the detector.



## Appendix B

### Numerical values of the analysing power in pp elastic scattering

$T_p$ [GeV]	$\theta_{cm}$ [°]	$A_y(\theta_{cm})$	$\Delta A_y(\theta_{cm})$
0.796	6.6	0.1701	0.0112
0.796	7.8	0.1806	0.006
0.796	9	0.2108	0.0047
0.796	10.2	0.2326	0.0042
0.796	11.4	0.2505	0.0042
0.796	12.6	0.2682	0.004
0.796	13.8	0.2897	0.004
0.796	15	0.3088	0.0038
0.796	16.2	0.3188	0.0038
0.796	17.4	0.3377	0.0038
0.796	18.6	0.3506	0.0038
0.796	19.8	0.3688	0.004
0.796	21	0.3789	0.0042
0.796	22.2	0.4022	0.0042
0.796	23.4	0.4049	0.0045
0.796	24.6	0.4152	0.0054
0.796	25.8	0.4336	0.0052
0.796	27	0.4414	0.0058
0.796	28.8	0.4466	0.0059
0.796	31.2	0.4651	0.0137

TABLE B.1: Analysing power in  $\vec{p}p$  elastic scattering at  $T_p = 0.796$  GeV, calculated from STT data.

$T_p$ [GeV]	$\theta_{cm}$ [°]	$A_y(\theta_{cm})$	$\Delta A_y(\theta_{cm})$
1.6	4.2	0.1025	0.0124
1.6	5.4	0.1124	0.0034
1.6	6.6	0.1282	0.0028
1.6	7.8	0.1456	0.0024
1.6	9	0.1578	0.0022
1.6	10.2	0.1711	0.002
1.6	11.4	0.1908	0.002
1.6	12.6	0.2044	0.002
1.6	13.8	0.2179	0.002
1.6	15	0.2291	0.002
1.6	16.2	0.2457	0.0018
1.6	17.4	0.2528	0.002
1.6	18.6	0.2609	0.002
1.6	19.8	0.2694	0.002
1.6	21	0.2836	0.0026
1.6	22.2	0.2878	0.0034
1.6	23.4	0.3016	0.0043
1.6	25.2	0.3081	0.0041

TABLE B.2: Analysing power in  $\vec{p}p$  elastic scattering at  $T_p = 1.6$  GeV, calculated from STT data.

$T_p$ [GeV]	$\theta_{cm}$ [°]	$A_y(\theta_{cm})$	$\Delta A_y(\theta_{cm})$
1.8	5.4	0.1106	0.0052
1.8	6.6	0.1278	0.0042
1.8	7.8	0.1405	0.004
1.8	9	0.1544	0.0036
1.8	10.2	0.172	0.0034
1.8	11.4	0.182	0.0034
1.8	12.6	0.1964	0.0034
1.8	13.8	0.2122	0.0034
1.8	15	0.2166	0.0034
1.8	16.2	0.2297	0.0031
1.8	17.4	0.2426	0.0035
1.8	18.6	0.2473	0.004
1.8	19.8	0.2584	0.0048
1.8	21	0.2656	0.0057
1.8	22.2	0.2707	0.0067
1.8	23.4	0.2719	0.0076
1.8	24.6	0.2776	0.0086
1.8	25.8	0.2822	0.0113

TABLE B.3: Analysing power in  $\vec{p}p$  elastic scattering at  $T_p = 1.8$  GeV, calculated from STT data.

$T_p$ [GeV]	$\theta_{cm}$ [°]	$A_y(\theta_{cm})$	$\Delta A_y(\theta_{cm})$
1.965	4.2	0.1034	0.0068
1.965	5.4	0.1102	0.0037
1.965	6.6	0.1393	0.0033
1.965	7.8	0.1571	0.0033
1.965	9	0.1781	0.003
1.965	10.2	0.1895	0.0028
1.965	11.4	0.1991	0.0028
1.965	12.6	0.2156	0.0028
1.965	13.8	0.2299	0.0026
1.965	15	0.2357	0.0026
1.965	16.2	0.2499	0.0026
1.965	17.4	0.2649	0.0026
1.965	18.6	0.2723	0.0028
1.965	19.8	0.2805	0.0035
1.965	21	0.2933	0.0042
1.965	22.2	0.2973	0.0047
1.965	23.4	0.3127	0.0056

TABLE B.4: Analysing power in  $\vec{p}p$  elastic scattering at  $T_p = 1.965$  GeV, calculated from STT data.

$T_p$ [GeV]	$\theta_{cm}$ [°]	$A_y(\theta_{cm})$	$\Delta A_y(\theta_{cm})$
2.157	4.2	0.085	0.0044
2.157	5.4	0.0984	0.0028
2.157	6.6	0.1235	0.0026
2.157	7.8	0.1325	0.0024
2.157	9	0.1484	0.0024
2.157	10.2	0.1632	0.0022
2.157	11.4	0.1726	0.0022
2.157	12.6	0.1868	0.002
2.157	13.8	0.1913	0.002
2.157	15	0.2011	0.0022
2.157	16.2	0.2113	0.002
2.157	17.4	0.2201	0.0022
2.157	18.6	0.2304	0.0026
2.157	19.8	0.2342	0.0032
2.157	21	0.2446	0.0036
2.157	22.2	0.2508	0.0042
2.157	23.4	0.2544	0.0112

TABLE B.5: Analysing power in  $\vec{p}p$  elastic scattering at  $T_p = 2.157$  GeV, calculated from STT data.

$T_p$ [GeV]	$\theta_{cm}$ [°]	$A_y(\theta_{cm})$	$\Delta A_y(\theta_{cm})$
2.368	4.2	0.0757	0.0044
2.368	5.4	0.0911	0.003
2.368	6.6	0.1036	0.0028
2.368	7.8	0.1183	0.0028
2.368	9	0.1289	0.0028
2.368	10.2	0.1353	0.0025
2.368	11.4	0.1507	0.0025
2.368	12.6	0.157	0.0023
2.368	13.8	0.1682	0.0025
2.368	15	0.1733	0.0023
2.368	16.2	0.1825	0.0023
2.368	17.4	0.1878	0.0028
2.368	18.6	0.1945	0.0035
2.368	19.8	0.2037	0.0039
2.368	21	0.2007	0.0044
2.368	22.2	0.2046	0.0099

TABLE B.6: Analysing power in  $\vec{p}p$  elastic scattering at  $T_p = 2.368$  GeV, calculated from STT data.

$T_p$ [GeV]	$\theta_{cm}$ [°]	$A_y(\theta_{cm})$	$\Delta A_y(\theta_{cm})$
0.796	14.5	0.3065	0.0045
0.796	15.5	0.3241	0.0046
0.796	16.5	0.3331	0.0047
0.796	17.5	0.3445	0.0048
0.796	18.5	0.3659	0.0048
0.796	19.5	0.373	0.0049
0.796	20.5	0.385	0.0051
0.796	21.5	0.3908	0.0052
0.796	22.5	0.4055	0.0056
0.796	23.5	0.4124	0.0078

TABLE B.7: Analysing power in  $\vec{p}p$  elastic scattering at  $T_p = 0.796$  GeV, calculated from FD data.

$T_p$ [GeV]	$\theta_{cm}$ [°]	$A_y(\theta_{cm})$	$\Delta A_y(\theta_{cm})$
1.6	11.5	0.1873	0.0085
1.6	12.5	0.1988	0.0031
1.6	13.5	0.2101	0.0026
1.6	14.5	0.223	0.0024
1.6	15.5	0.2373	0.0025
1.6	16.5	0.2448	0.0025
1.6	17.5	0.2566	0.0026
1.6	18.5	0.2604	0.0027
1.6	19.5	0.2723	0.0028
1.6	20.5	0.2756	0.003
1.6	21.5	0.2844	0.003
1.6	22.5	0.2941	0.0031
1.6	23.5	0.2991	0.0033
1.6	24.5	0.3012	0.0034
1.6	25.5	0.3076	0.0036
1.6	26.5	0.3168	0.0054

TABLE B.8: Analysing power in  $\vec{p}\vec{p}$  elastic scattering at  $T_p = 1.6$  GeV, calculated from FD data.

$T_p$ [GeV]	$\theta_{cm}$ [°]	$A_y(\theta_{cm})$	$\Delta A_y(\theta_{cm})$
1.8	12.5	0.194	0.006
1.8	13.5	0.2067	0.0048
1.8	14.5	0.2231	0.0045
1.8	15.5	0.2281	0.0045
1.8	16.5	0.2418	0.0045
1.8	17.5	0.2451	0.0046
1.8	18.5	0.2591	0.0047
1.8	19.5	0.2634	0.0048
1.8	20.5	0.269	0.005
1.8	21.5	0.2784	0.0053
1.8	22.5	0.28	0.0057
1.8	23.5	0.2889	0.0063
1.8	24.5	0.2822	0.0068
1.8	25.5	0.2902	0.0069
1.8	26.5	0.2935	0.0072

TABLE B.9: Analysing power in  $\vec{p}\vec{p}$  elastic scattering at  $T_p = 1.8$  GeV, calculated from FD data.

$T_p$ [GeV]	$\theta_{cm}$ [°]	$A_y(\theta_{cm})$	$\Delta A_y(\theta_{cm})$
1.965	12.5	0.2154	0.0062
1.965	13.5	0.2323	0.0034
1.965	14.5	0.2337	0.0028
1.965	15.5	0.2468	0.0028
1.965	16.5	0.256	0.0029
1.965	17.5	0.2636	0.003
1.965	18.5	0.2749	0.0031
1.965	19.5	0.2789	0.0032
1.965	20.5	0.2835	0.0033
1.965	21.5	0.2926	0.0034
1.965	22.5	0.3001	0.0036
1.965	23.5	0.3098	0.004
1.965	24.5	0.3142	0.0041
1.965	25.5	0.3126	0.0042
1.965	26.5	0.3185	0.0045

TABLE B.10: Analysing power in  $\vec{p}p$  elastic scattering at  $T_p = 1.965$  GeV, calculated from FD data.

$T_p$ [GeV]	$\theta_{cm}$ [°]	$A_y(\theta_{cm})$	$\Delta A_y(\theta_{cm})$
2.157	13.5	0.1874	0.0026
2.157	14.5	0.1998	0.0021
2.157	15.5	0.2066	0.002
2.157	16.5	0.2137	0.002
2.157	17.5	0.2226	0.0021
2.157	18.5	0.2265	0.0022
2.157	19.5	0.2302	0.0023
2.157	20.5	0.2373	0.0024
2.157	21.5	0.2438	0.0025
2.157	22.5	0.242	0.0026
2.157	23.5	0.2548	0.0028
2.157	24.5	0.2487	0.003
2.157	25.5	0.2559	0.0032
2.157	26.5	0.2637	0.0035
2.157	27.5	0.2639	0.0036

TABLE B.11: Analysing power in  $\vec{p}p$  elastic scattering at  $T_p = 2.157$  GeV, calculated from FD data.

$T_p$ [GeV]	$\theta_{cm}$ [°]	$A_y(\theta_{cm})$	$\Delta A_y(\theta_{cm})$
2.368	13.5	0.1641	0.0033
2.368	14.5	0.1764	0.0024
2.368	15.5	0.1743	0.0023
2.368	16.5	0.1865	0.0023
2.368	17.5	0.1916	0.0024
2.368	18.5	0.1966	0.0025
2.368	19.5	0.2018	0.0026
2.368	20.5	0.206	0.0028
2.368	21.5	0.2066	0.0029
2.368	22.5	0.2157	0.003
2.368	23.5	0.2195	0.0033
2.368	24.5	0.2147	0.0035
2.368	25.5	0.2135	0.0037
2.368	26.5	0.2215	0.004
2.368	27.5	0.2237	0.0043
2.368	28.5	0.2209	0.0046

TABLE B.12: Analysing power in  $\vec{p}p$  elastic scattering at  $T_p = 2.368$  GeV, calculated from FD data.



## Appendix C

Numerical values of the differential  
cross section in pp elastic scattering

$T_p$ [GeV]	$\theta_{cm}$ [°]	$d\sigma/d\Omega(\theta_{cm})$ [mb]	$-t$ (GeV/c) <sup>2</sup>	$d\sigma/dt$ [mb/(GeV/c) <sup>2</sup> ]
1.0	12.25	17.72	0.02136	118.7
1.0	12.75	17.64	0.02314	118.1
1.0	13.25	17.36	0.02498	116.2
1.0	13.75	16.98	0.02689	113.7
1.0	14.25	16.78	0.02887	112.4
1.0	14.75	16.49	0.03092	110.5
1.0	15.25	16.41	0.03304	109.9
1.0	15.75	16.18	0.03523	108.4
1.0	16.25	15.87	0.03748	106.2
1.0	16.75	15.67	0.03981	105.0
1.0	17.25	15.47	0.04220	103.6
1.0	17.75	15.17	0.04467	101.6
1.0	18.25	14.98	0.04720	100.3
1.0	18.75	14.71	0.04979	98.50
1.0	19.25	14.55	0.05246	97.44
1.0	19.75	14.39	0.05519	96.33
1.0	20.25	14.03	0.05799	93.96
1.0	20.75	13.66	0.06086	91.50
1.0	21.25	13.45	0.06380	90.08
1.0	21.75	13.38	0.06680	89.60
1.0	22.25	12.94	0.06986	86.66
1.0	22.75	12.88	0.07300	86.28
1.0	23.25	12.53	0.07620	83.89
1.0	23.75	12.32	0.07946	82.48
1.0	24.25	11.90	0.08279	79.70

TABLE C.1: Differential cross section in pp elastic scattering at  $T_p = 1$  GeV.

$T_p$ [GeV]	$\theta_{cm}$ [°]	$d\sigma/d\Omega(\theta_{cm})$ [mb]	$-t$ (GeV/c) <sup>2</sup>	$d\sigma/dt$ [mb/(GeV/c) <sup>2</sup> ]
1.6	13.75	23.17	0.04302	96.98
1.6	14.25	22.58	0.04619	94.51
1.6	14.75	21.91	0.04947	91.7
1.6	15.25	21.45	0.05286	89.76
1.6	15.75	20.59	0.05636	86.18
1.6	16.25	20.59	0.05997	86.18
1.6	16.75	19.95	0.06370	83.51
1.6	17.25	19.18	0.06753	80.27
1.6	17.75	19.01	0.07147	79.58
1.6	18.25	18.49	0.07551	77.38
1.6	18.75	17.69	0.07967	74.05
1.6	19.25	17.33	0.08394	72.53
1.6	19.75	16.83	0.08831	70.43
1.6	20.25	16.18	0.09279	67.72
1.6	20.75	15.88	0.09738	66.47
1.6	21.25	15.33	0.1021	64.16
1.6	21.75	14.68	0.1069	61.43
1.6	22.25	14.38	0.1118	60.16
1.6	22.75	13.79	0.1168	57.72
1.6	23.25	13.20	0.1219	55.26
1.6	23.75	12.90	0.1271	53.98
1.6	24.25	12.23	0.1325	51.18
1.6	24.75	12.18	0.1379	50.99
1.6	25.25	11.54	0.1434	48.32
1.6	25.75	11.07	0.1491	46.33
1.6	26.25	10.81	0.1548	45.26

TABLE C.2: Differential cross section in pp elastic scattering at  $T_p = 1.6$  GeV.

$T_p$ [GeV]	$\theta_{cm}$ [°]	$d\sigma/d\Omega(\theta_{cm})$ [mb]	$-t$ (GeV/c) <sup>2</sup>	$d\sigma/dt$ [mb/(GeV/c) <sup>2</sup> ]
1.8	14.25	23.43	0.05197	87.16
1.8	14.75	22.97	0.05566	85.47
1.8	15.25	22.17	0.05947	82.47
1.8	15.75	21.62	0.06341	80.42
1.8	16.25	20.78	0.06747	77.31
1.8	16.75	20.39	0.07166	75.86
1.8	17.25	19.83	0.07597	73.78
1.8	17.75	19.24	0.08040	71.56
1.8	18.25	18.56	0.08495	69.05
1.8	18.75	17.96	0.08963	66.81
1.8	19.25	17.40	0.09443	64.73
1.8	19.75	16.70	0.09935	62.14
1.8	20.25	16.04	0.1044	59.67
1.8	20.75	15.83	0.1095	58.90
1.8	21.25	15.07	0.1148	56.08
1.8	21.75	14.36	0.1202	53.43
1.8	22.25	14.21	0.1258	52.87
1.8	22.75	13.59	0.1314	50.56
1.8	23.25	12.84	0.1372	47.77
1.8	23.75	12.34	0.1430	45.89
1.8	24.25	11.95	0.1490	44.45
1.8	24.75	11.60	0.1551	43.16
1.8	25.25	11.05	0.1614	41.09
1.8	25.75	10.48	0.1677	39.00
1.8	26.25	10.18	0.1742	37.86
1.8	26.75	9.678	0.1807	36.01
1.8	27.25	9.457	0.1874	35.18

TABLE C.3: Differential cross section in *pp* elastic scattering at  $T_p = 1.8$  GeV.

$T_p$ [GeV]	$\theta_{cm}$ [°]	$d\sigma/d\Omega(\theta_{cm})$ [mb]	$-t$ (GeV/c) <sup>2</sup>	$d\sigma/dt$ [mb/(GeV/c) <sup>2</sup> ]
2.0	14.25	24.5061	0.0577396	82.05
2.0	14.75	23.87	0.06184	79.94
2.0	15.25	23.17	0.06608	77.57
2.0	15.75	22.55	0.07045	75.5
2.0	16.25	21.67	0.07497	72.57
2.0	16.75	20.83	0.07962	69.75
2.0	17.25	20.43	0.08441	68.42
2.0	17.75	19.58	0.08933	65.56
2.0	18.25	18.83	0.09439	63.05
2.0	18.75	18.18	0.09959	60.86
2.0	19.25	17.51	0.1049	58.63
2.0	19.75	17.01	0.1104	56.97
2.0	20.25	16.18	0.116.	54.19
2.0	20.75	15.3.	0.1217	51.24
2.0	21.25	15.04	0.1276	50.36
2.0	21.75	14.38	0.1336	48.15
2.0	22.25	13.43	0.1397	44.98
2.0	22.75	13.21	0.146.	44.23
2.0	23.25	12.67	0.1524	42.44
2.0	23.75	12.01	0.1589	40.20
2.0	24.25	11.35	0.1656	38.00
2.0	24.75	10.74	0.1724	35.95
2.0	25.25	10.47	0.1793	35.04
2.0	25.75	9.949	0.1863	33.31
2.0	26.25	9.499	0.1935	31.8.
2.0	26.75	9.036	0.2008	30.26
2.0	27.25	8.484	0.2083	28.41
2.0	27.75	8.287	0.2158	27.75

TABLE C.4: Differential cross section in *pp* elastic scattering at  $T_p = 2.0$  GeV

$T_p$ [GeV]	$\theta_{cm}$ [°]	$d\sigma/d\Omega(\theta_{cm})$ [mb]	$-t$ (GeV/c) <sup>2</sup>	$d\sigma/dt$ [mb/(GeV/c) <sup>2</sup> ]
2.2	14.75	23.17	0.06802	70.54
2.2	15.25	22.33	0.07269	67.98
2.2	15.75	21.87	0.07750	66.58
2.2	16.25	20.74	0.08247	63.14
2.2	16.75	19.87	0.08758	60.47
2.2	17.25	19.26	0.09285	58.64
2.2	17.75	18.35	0.09826	55.87
2.2	18.25	17.89	0.1038	54.46
2.2	18.75	17.12	0.1095	52.12
2.2	19.25	16.26	0.1154	49.51
2.2	19.75	15.69	0.1214	47.76
2.2	20.25	14.89	0.1276	45.32
2.2	20.75	13.91	0.1339	42.33
2.2	21.25	13.76	0.1403	41.89
2.2	21.75	13.03	0.1470	39.67
2.2	22.25	12.35	0.1537	37.58
2.2	22.75	11.87	0.1606	36.13
2.2	23.25	11.11	0.1676	33.81
2.2	23.75	10.81	0.1748	32.89
2.2	24.25	10.24	0.1821	31.18
2.2	24.75	9.573	0.1896	29.14
2.2	25.25	9.204	0.1972	28.02
2.2	25.75	8.527	0.2050	25.96
2.2	26.25	8.194	0.2129	24.94
2.2	26.75	7.755	0.2209	23.6
2.2	27.25	7.201	0.2291	21.92
2.2	27.75	6.867	0.2374	20.9
2.2	28.25	6.436	0.2459	19.59

TABLE C.5: Differential cross section in pp elastic scattering at  $T_p = 2.2$  GeV

$T_p$ [GeV]	$\theta_{cm}$ [°]	$d\sigma/d\Omega(\theta_{cm})$ [mb]	$-t$ (GeV/c) <sup>2</sup>	$d\sigma/dt$ [mb/(GeV/c) <sup>2</sup> ]
2.4	15.25	23.11	0.0793	64.5
2.4	15.75	21.91	0.0846	61.14
2.4	16.25	21.35	0.08996	59.56
2.4	16.75	20.35	0.09554	56.77
2.4	17.25	19.15	0.1013	53.42
2.4	17.75	18.60	0.1072	51.89
2.4	18.25	17.77	0.1133	49.57
2.4	18.75	17.06	0.1195	47.61
2.4	19.25	16.23	0.1259	45.29
2.4	19.75	15.30	0.1325	42.68
2.4	20.25	14.93	0.1392	41.67
2.4	20.75	14.17	0.1461	39.52
2.4	21.25	13.12	0.1531	36.62
2.4	21.75	12.76	0.1603	35.61
2.4	22.25	11.87	0.1677	33.12
2.4	22.75	11.45	0.1752	31.95
2.4	23.25	10.81	0.1829	30.17
2.4	23.75	10.16	0.1907	28.33
2.4	24.25	9.786	0.1987	27.31
2.4	24.75	9.043	0.2068	25.23
2.4	25.25	8.573	0.2152	23.92
2.4	25.75	8.060	0.2236	22.49
2.4	26.25	7.604	0.2322	21.22
2.4	26.75	7.213	0.2410	20.12
2.4	27.25	6.702	0.2499	18.7
2.4	27.75	6.441	0.2590	17.97
2.4	28.25	5.983	0.2682	16.7
2.4	28.75	5.671	0.2776	15.82
2.4	29.25	5.392	0.2871	15.05

TABLE C.6: Differential cross section in *pp* elastic scattering at  $T_p = 2.4$  GeV

$T_p$ [GeV]	$\theta_{cm}$ [°]	$d\sigma/d\Omega(\theta_{cm})$ [mb]	$-t$ (GeV/c) <sup>2</sup>	$d\sigma/dt$ [mb/(GeV/c) <sup>2</sup> ]
2.6	15.75	21.58	0.0916	55.57
2.6	16.25	20.63	0.0975	53.12
2.6	16.75	19.82	0.1035	51.06
2.6	17.25	18.88	0.1097	48.64
2.6	17.75	17.61	0.1161	45.36
2.6	18.25	17.24	0.1227	44.40
2.6	18.75	16.35	0.1295	42.11
2.6	19.25	15.56	0.1364	40.08
2.6	19.75	14.83	0.1435	38.20
2.6	20.25	13.85	0.1508	35.66
2.6	20.75	13.41	0.1582	34.54
2.6	21.25	12.50	0.1659	32.18
2.6	21.75	11.79	0.1737	30.36
2.6	22.25	11.26	0.1816	29.00
2.6	22.75	10.45	0.1898	26.92
2.6	23.25	10.04	0.1981	25.86
2.6	23.75	9.354	0.2066	24.09
2.6	24.25	8.864	0.2153	22.83
2.6	24.75	8.381	0.2241	21.59
2.6	25.25	7.735	0.2331	19.92
2.6	25.75	7.377	0.2422	19.00
2.6	26.25	6.740	0.2516	17.36
2.6	26.75	6.518	0.2611	16.79
2.6	27.25	6.064	0.2707	15.62
2.6	27.75	5.608	0.2806	14.44
2.6	28.25	5.324	0.2906	13.71
2.6	28.75	4.88	0.3007	12.57
2.6	29.25	4.615	0.311	11.89
2.6	29.75	4.348	0.3215	11.2

TABLE C.7: Differential cross section in *pp* elastic scattering at  $T_p = 2.6$  GeV

$T_p$ [GeV]	$\theta_{cm}$ [°]	$d\sigma/d\Omega(\theta_{cm})$ [mb]	$-t$ (GeV/c) <sup>2</sup>	$d\sigma/dt$ [mb/(GeV/c) <sup>2</sup> ]
2.8	16.25	20.12	0.1049	48.13
2.8	16.75	19.10	0.1115	45.67
2.8	17.25	17.84	0.1182	42.66
2.8	17.75	17.11	0.1251	40.93
2.8	18.25	16.16	0.1321	38.65
2.8	18.75	15.48	0.1394	37.01
2.8	19.25	14.56	0.1469	34.83
2.8	19.75	13.71	0.1545	32.80
2.8	20.25	13.07	0.1624	31.26
2.8	20.75	12.17	0.1704	29.11
2.8	21.25	11.81	0.1786	28.24
2.8	21.75	10.89	0.1870	26.04
2.8	22.25	10.09	0.1956	24.13
2.8	22.75	9.771	0.2044	23.37
2.8	23.25	8.991	0.2133	21.50
2.8	23.75	8.505	0.2225	20.34
2.8	24.25	7.938	0.2318	18.98
2.8	24.75	7.452	0.2413	17.82
2.8	25.25	7.020	0.2510	16.79
2.8	25.75	6.449	0.2609	15.42
2.8	26.25	6.015	0.2709	14.39
2.8	26.75	5.586	0.2812	13.36
2.8	27.25	5.278	0.2916	12.62
2.8	27.75	4.915	0.3022	11.76
2.8	28.25	4.633	0.3129	11.08
2.8	28.75	4.251	0.3239	10.17
2.8	29.25	3.900	0.3350	9.326
2.8	29.75	3.749	0.3463	8.966
2.8	30.25	3.425	0.3577	8.191

TABLE C.8: Differential cross section in *pp* elastic scattering at  $T_p = 2.8$  GeV



## Appendix D

### Numerical values of the analysing power in $pd$ elastic scattering

$T_p$ [GeV]	$\theta_{cm}$ [°]	$A_y(\theta_{cm})$	$\Delta A_y(\theta_{cm})$
0.796	7.5	0.263009	0.0116205
0.796	8.5	0.273881	0.0040296
0.796	9.5	0.299352	0.00322963
0.796	10.5	0.322533	0.0028564
0.796	11.5	0.347553	0.00287911
0.796	12.5	0.366042	0.00275279
0.796	13.5	0.386115	0.00236104
0.796	14.5	0.40091	0.0026661
0.796	15.5	0.418881	0.0028934
0.796	16.5	0.424433	0.00314449
0.796	17.5	0.431879	0.00338627
0.796	18.5	0.434628	0.00366794
0.796	19.5	0.436552	0.00398735
0.796	20.5	0.443078	0.00436351
0.796	21.5	0.443576	0.00488554
0.796	22.5	0.439858	0.00565274
0.796	23.5	0.434506	0.00655225
0.796	24.5	0.420296	0.00764164
0.796	25.5	0.414288	0.00898069
0.796	26.5	0.433489	0.0109752
0.796	27.5	0.407203	0.0164406
0.796	28.5	0.414443	0.0904038

TABLE D.1: Analysing power in  $\vec{p}d$  elastic scattering at  $T_p = 0.796$  GeV.

Appendix D. *Numerical values of the analysing power in  $pd$  elastic scattering* 100

$T_p$ [GeV]	$\theta_{cm}$ [°]	$A_y(\theta_{cm})$	$\Delta A_y(\theta_{cm})$
1.6	5.5	0.0957251	0.0054474
1.6	6.5	0.0916527	0.00278479
1.6	7.5	0.10736	0.00233907
1.6	8.5	0.116182	0.0024903
1.6	9.5	0.123965	0.00215339
1.6	10.5	0.134105	0.00254911
1.6	11.5	0.143505	0.00282113
1.6	12.5	0.143702	0.00321747
1.6	13.5	0.149931	0.0036815
1.6	14.5	0.149845	0.00422813
1.6	15.5	0.151055	0.00488859
1.6	16.5	0.158704	0.00575297
1.6	17.5	0.148795	0.00684865
1.6	18.5	0.151461	0.0087816
1.6	19.5	0.115061	0.0237576

TABLE D.2: Analysing power in  $\bar{p}d$  elastic scattering at  $T_p = 1.6$  GeV.

$T_p$ [GeV]	$\theta_{cm}$ [°]	$A_y(\theta_{cm})$	$\Delta A_y(\theta_{cm})$
1.8	5.5	0.109371	0.00246849
1.8	6.5	0.118918	0.00168386
1.8	7.5	0.129229	0.00140982
1.8	8.5	0.139699	0.00127214
1.8	9.5	0.1496	0.0013163
1.8	10.5	0.162585	0.00151674
1.8	11.5	0.168233	0.00171027
1.8	12.5	0.172569	0.00196232
1.8	13.5	0.182555	0.00226907
1.8	14.5	0.189876	0.00266811
1.8	15.5	0.183029	0.00319076
1.8	16.5	0.179209	0.00389827
1.8	17.5	0.179281	0.00534402
1.8	18.5	0.185194	0.0307236

TABLE D.3: Analysing power in  $\bar{p}d$  elastic scattering at  $T_p = 1.8$  GeV.

$T_p$ [GeV]	$\theta_{cm}$ [°]	$A_y(\theta_{cm})$	$\Delta A_y(\theta_{cm})$
1.965	4.5	0.103755	0.0109747
1.965	5.5	0.10013	0.00242958
1.965	6.5	0.111362	0.00193356
1.965	7.5	0.127183	0.00166453
1.965	8.5	0.136882	0.00139161
1.965	9.5	0.145783	0.00157882
1.965	10.5	0.157591	0.00179283
1.965	11.5	0.167153	0.00203506
1.965	12.5	0.170078	0.00233355
1.965	13.5	0.172224	0.00271707
1.965	14.5	0.17978	0.00321046
1.965	15.5	0.165606	0.00387635
1.965	16.5	0.167518	0.00488782
1.965	17.5	0.161354	0.0126552

TABLE D.4: Analysing power in  $\bar{p}d$  elastic scattering at  $T_p = 1.965$  GeV.

$T_p$ [GeV]	$\theta_{cm}$ [°]	$A_y(\theta_{cm})$	$\Delta A_y(\theta_{cm})$
2.157	4.5	0.0884989	0.00742026
2.157	5.5	0.0946571	0.00284687
2.157	6.5	0.108095	0.00244463
2.157	7.5	0.115644	0.00200043
2.157	8.5	0.129691	0.00188169
2.157	9.5	0.136451	0.00218152
2.157	10.5	0.145238	0.0024905
2.157	11.5	0.152605	0.00286126
2.157	12.5	0.15902	0.00331179
2.157	13.5	0.164784	0.00392873
2.157	14.5	0.164469	0.00473993
2.157	15.5	0.157244	0.00586484
2.157	16.5	0.153914	0.010714

TABLE D.5: Analysing power in  $\bar{p}d$  elastic scattering at  $T_p = 2.157$  GeV.

$T_p$ [GeV]	$\theta_{cm}$ [°]	$A_y(\theta_{cm})$	$\Delta A_y(\theta_{cm})$
2.368	4.5	0.0821758	0.00446351
2.368	5.5	0.0910888	0.00232888
2.368	6.5	0.0994296	0.00213613
2.368	7.5	0.113342	0.0016571
2.368	8.5	0.118115	0.00176567
2.368	9.5	0.124953	0.00204504
2.368	10.5	0.132086	0.00237079
2.368	11.5	0.135738	0.00277393
2.368	12.5	0.143188	0.00329013
2.368	13.5	0.147642	0.00401655
2.368	14.5	0.135902	0.00497647
2.368	15.5	0.133483	0.00815986

TABLE D.6: Analysing power in  $\vec{p}d$  elastic scattering at  $T_p = 2.368$  GeV.

## Appendix E

### Numerical values of the analysing power in pn quasi-free elastic scattering

$T_p$ [GeV]	$\theta_{cm}$ [°]	$A_y(\theta_{cm})$	$\Delta A_y(\theta_{cm})$
0.796	18	0.27	0.018
0.796	20	0.29	0.018
0.796	22	0.278	0.016
0.796	24	0.328	0.022

TABLE E.1: Analysing power in  $\vec{p}n$  quasi-free elastic scattering at  $T_p = 0.796$  GeV.

$T_p$ [GeV]	$\theta_{cm}$ [°]	$A_y(\theta_{cm})$	$\Delta A_y(\theta_{cm})$
1.6	14	0.137	0.018
1.6	17	0.151	0.015
1.6	20	0.153	0.015
1.6	23	0.170	0.016
1.6	26	0.169	0.018

TABLE E.2: Analysing power in  $\vec{p}n$  quasi-free elastic scattering at  $T_p = 1.6$  GeV.

$T_p$ [GeV]	$\theta_{cm}$ [°]	$A_y(\theta_{cm})$	$\Delta A_y(\theta_{cm})$
1.8	13.5	0.125	0.011
1.8	16.5	0.145	0.008
1.8	19.5	0.152	0.008
1.8	22.5	0.148	0.009
1.8	25.5	0.158	0.01

TABLE E.3: Analysing power in  $\vec{p}n$  quasi-free elastic scattering at  $T_p = 1.8$  GeV.

$T_p$ [GeV]	$\theta_{cm}$ [°]	$A_y(\theta_{cm})$	$\Delta A_y(\theta_{cm})$
1.965	13.5	0.108	0.016
1.965	16.5	0.119	0.011
1.965	19.5	0.138	0.011
1.965	22.5	0.112	0.012
1.965	25.5	0.141	0.013
1.965	28.5	0.127	0.022

TABLE E.4: Analysing power in  $\vec{p}n$  quasi-free elastic scattering at  $T_p = 1.965$  GeV.

$T_p$ [GeV]	$\theta_{cm}$ [°]	$A_y(\theta_{cm})$	$\Delta A_y(\theta_{cm})$
2.157	14	0.091	0.016
2.157	17	0.103	0.013
2.157	20	0.111	0.013
2.157	23	0.143	0.014
2.157	26	0.115	0.017
2.157	29	0.141	0.026

TABLE E.5: Analysing power in  $\vec{p}n$  quasi-free elastic scattering at  $T_p = 2157$  GeV.

$T_p$ [GeV]	$\theta_{cm}$ [°]	$A_y(\theta_{cm})$	$\Delta A_y(\theta_{cm})$
2.368	17	0.085	0.011
2.368	20	0.102	0.012
2.368	23	0.102	0.013
2.368	26	0.122	0.016
2.368	29	0.100	0.021

TABLE E.6: Analysing power in  $\vec{p}n$  quasi-free elastic scattering at  $T_p = 2.368$  GeV.

## List of Figures

1.1	The Standard Model of elementary particles (more schematic depiction), with the three generations of matter, gauge bosons in the fourth column, and the Higgs boson in the fifth. . . . .	2
1.2	Abundance plots of c.m. scattering angle ( $\theta_{cm}$ ) versus beam energy ( $T_{lab}$ ) for experiments on the analysing power $A_y$ (left) and for cross-section $d\sigma/d\Omega$ (right) in proton-proton elastic scattering. Source: <a href="http://nn-online.org">http://nn-online.org</a> . . . . .	5
1.3	Abundance plot of c.m. scattering angle ( $\theta_{cm}$ ) versus beam energy ( $T_{lab}$ ) for experiments on the analysing power $A_y$ in proton-neutron scattering. Source: <a href="http://nn-online.org">http://nn-online.org</a> . . . . .	6
2.1	Madison convention for the definition of the laboratory-coordinate system. The $z$ axis is along the incident beam momentum. The scattering is in the $xz$ plane. . . . .	9
2.2	Two-detector idealistic symmetric arrangement . . . . .	11
3.1	The COSY accelerator facility. The positions of the ANKE spectrometer and the EDDA polarimeter are shown. . . . .	16
3.2	Set-up of the polarised ion source at COSY. . . . .	17
3.3	Schematic diagram of the EDDA detector. . . . .	21
3.4	The ANKE spectrometer setup (top view), showing the positions of the hydrogen cluster-jet target, the silicon tracking telescopes (STT), and the forward detector (FD). . . . .	22
3.5	The cluster-jet target installed at ANKE. . . . .	23
3.6	Cluster production at the Laval-nozzle. . . . .	24
3.7	Silicon Tracking Telescope. . . . .	25
4.1	The polarisation values, calculated ring by ring, are shown versus corresponding laboratory polar angles (according to Appendix A). The sample plots are shown for beam kinetic energy $T_p = 1.8$ GeV and $T_p = 2.2$ GeV. . . . .	31
4.2	Difference between the angle reconstructed from the energy $\theta(E)$ and directly reconstructed angle of the track $\theta$ . The example plot is shown at $T_p = 2.368$ GeV. . . . .	33
4.3	Missing mass $M_X(pp \rightarrow pX)$ spectrum obtained for a beam energy of 1.6 GeV showing the clear proton peak when detecting one proton in the STT. . . . .	34

4.4	Missing mass $M_X(pp \rightarrow pX)$ spectrum obtained from the particles detected in forward detector at the beam kinetic energy of 1.6 GeV.	36
4.5	Forward detector angular acceptance for $pp \rightarrow pp$ at the beam kinetic energy of 1.6 GeV.	36
4.6	Luminosity ratios with different angular cuts. Example plots are shown for $T_p = 1.8$ GeV (left panel) and 2.368 GeV (right panel).	37
4.7	Difference of scattering angle reconstructed in FD and STT. Example plots are shown for $T_p = 0.796$ GeV (left panel) and 2.157 GeV (right panel).	39
4.8	Systematic error due to the shift of the scattering angle. Example plots are shown for the beam kinetic energies $T_p = 0.796$ GeV (left panel) and 2.368 GeV (right panel).	40
4.9	The instability factor $r_{\uparrow}/r_{\downarrow}$ angular dependences at the beam energies of 0.796 GeV (left panel) and 1.8 GeV (right panel).	40
4.10	Efficiency of the elastic event reconstruction in FD in the cycles with the beam polarisation mode up (left panel) and beam polarisation mode down (right panel).	41
4.11	Comparison of the ANKE measurements of the proton analysing power in $pp$ elastic scattering using the STT (red filled circles) and FD (blue filled triangles) systems with the curves corresponding to the SAID 2007 (solid black line) [5] and the revised fit (dashed red) solutions. Only statistical errors are shown so that the systematic uncertainties arising, for example, from the calibration of the EDDA polarimeter have not been included. Also shown are selected results from EDDA (black crosses) [10] at the energies different by no more than 7 MeV and, at 0.796 GeV, LAMPF [26–28], and SATURNE [29] (black open symbols).	42
4.12	Phase shift parameters for ${}^3F_2$ and ${}^3F_4$ partial waves from the 2014 SAID solution, in comparison with the older solution from 2007.	43
5.1	Beam Current Transformer (BCT) typical raw signal, recorded during the experiment.	47
5.2	Calibration of Beam Current Transformer signal via applying different current $I$ to the wire inserted into the beamline.	47
5.3	Schottky power spectra obtained during one 300 s cycle and scaled to harmonic number 1 for 1.0 GeV (a) and 2.0 GeV (b). The mean frequencies are indicated by the vertical (red) lines.	50
5.4	Typical mean frequency shift derived from the Schottky power spectra of the type illustrated in Figure 5.3 for 1.0 GeV (left panel) and 2.0 GeV (right panel)	51
5.5	Average frequency shifts within the cycle duration, measured by new (blue) and old (green) spectrum analysers at 1.0 and 2.0 GeV.	51
5.6	Example of frequency shift caused by the background when the target is on $(\frac{df}{dt})_{bg}$ (left) and when the target is off $(\frac{df}{dt})_{rg}$ (right) compared to the total frequency shift $(\frac{df}{dt})_{tot}$ with the beam incident on the target (middle).	52

5.7	Variation of the mean revolution frequency with the field strength in the bending magnets for 2.0 GeV . . . . .	53
5.8	Combined ANKE data set of differential cross sections with respect to the four-momentum transfer $t$ compared to fits made on the basis of Equation 5.12. Systematic errors are not shown. The correct values are shown at 1.0 GeV but, for clarity of presentation, the other data are scaled down sequentially in energy by factors of 1.2. The true numerical values of the cross section and fit parameters are given in Appendix C and Table 5.2, accordingly. . . . .	56
5.9	Invariant differential cross section for $pp$ elastic scattering. The ANKE data at 1 GeV with statistical errors (blue squares) are compared to the IKAR (LNPI) hydrogen data at 992 MeV (green circles) [35] scaled by a factor of 1.085 and methane results at 991 MeV (red triangles) [37] scaled by a factor of 1.04. At very small values of $ t $ there is a rise caused mainly by Coulomb-nuclear interference. . . . .	57
5.10	The ANKE $pp$ differential cross section data at 2.2 GeV (closed blue circles) and 2.8 GeV (closed blue triangles) compared to the ANL results [38] at 2.2 GeV (open red circles) and 2.83 GeV (open red triangles). Systematic errors are not shown. For presentational purposes, both higher energy data sets have been scaled downwards by a common factor of 1.5. . . . .	58
5.11	Scaled ANKE proton-proton elastic differential cross sections at 1.0, 2.0, and 2.8 GeV with statistical errors compared to the SAID 2007 solution [6] and a modified (“new”) partial wave solution where the ANKE data have been taken into account. For presentational reasons the 2.0 and 2.8 GeV data and curves have been reduced by factors of 0.5 and 0.25, respectively. The best agreement with the new partial wave data was achieved by scaling the ANKE data with factors 0.97, 0.96, and 1.03 at the three energies. Such factors are within the uncertainties given in Table 5.1. . . . .	59
5.12	The predictions of Grein and Kroll [40] for the values of the forward $pp$ elastic differential cross section (solid line), the corresponding lower limit provided by the spin-independent optical theorem of (Equation 5.13) being indicated by the broken line. The extrapolated ANKE data, corresponding to the $A(\text{Corr.})$ parameter of Table 5.2, are shown with their quoted errors by the (blue) circles, whereas the (red) squares are the published IKAR values [35]. . . . .	61
5.13	Phase shifts for $^1S_0$ and $^1D_2$ partial waves from the 2015 SAID solution [30], in comparison with the older solution from 2007 [5]. . . . .	62
6.1	The acceptance $pd \rightarrow ppn_{sp}$ (black histograms) and $pd \rightarrow pnp_{sp}$ (red histograms) reactions simulated in the framework of spectator model at $T_p = 0.796$ GeV. One proton is detected in the FD and other one in the STT1 (left panel) or in the STT2 (right panel). . . . .	65
6.2	Missing-mass $M_X(pp \rightarrow ppX)$ spectra obtained for a beam energy of 2.157 GeV. The peak is consistent with the neutron mass value. . . . .	66

6.3	Comparison of the $pd$ elastic scattering asymmetries at $T_p = 1.965$ GeV obtained in two different ways: blue triangles stand for the cross-ratio method; red squares correspond to the simple left-right asymmetry, using the normalisation procedure described in the text.	68
6.4	Analysing power in $pd$ elastic scattering, along with the existing experimental data from SATURN at 0.796 GeV [43]. ANKE results include statistical errors only.	68
6.5	The difference of normalised missing mass distributions for two polarisation modes at 1.8 GeV.	70
6.6	The sum of normalised missing mass spectra at 1.8 GeV (blue points), fit with Gaussian and background of different shapes (black curve). Red dashed curves represent the polynomial approximation for the background, the green dashed curve represents the polynomial + Gaussian with $m_x \approx 0.86$ GeV/ $c^2$ .	70
6.7	The ANKE acceptance in terms of the $P_{sp}/P_t$ ratio dependence on c.m. the scattering angle at the beam energy of $T_p = 796$ GeV.	71
6.8	Analysing power dependence on the $P_{sp}/P_t$ ratio at the kinetic beam energy $T_p = 0.796$ GeV.	72
6.9	Analysing power in $pp$ quasi-free elastic scattering without any cuts (red points), with the same cuts as for $pn$ quasi-free elastic scattering (green triangles), compared to the analysing power obtained from free proton-proton elastic scattering at ANKE: FD (blue empty squares) and STT (blue empty circles). The results are shown at 0.796 GeV (upper panel) and 1.6 GeV (lower panel).	73
6.10	ANKE measurements of the analysing power in $pn$ quasi-elastic scattering (filled circles). The results at 0.796 GeV (upper panel) are compared with the curves corresponding to the SAID 2007 prediction (solid black line) [6] and other existing measurements (black open symbols) [44–47] The preliminary SAID solution for analysing power in $pn$ quasi-free elastic scattering at beam kinetic energy $T_p = 1.6$ GeV is shown in the middle panel in red dashed curve along with the ANKE and SATURN measurements at this energy. For the ease of presentation, the scaled ANKE data at other 4 energies are given in the lower panel. Also shown are the results from Argonne National Laboratory at 2.2 GeV energy [48, 49] (black open symbols). Only statistical errors are shown.	74

# List of Tables

3.1	Resonance strength $\epsilon_r$ and the ratio of preserved polarisation $P_f/P_i$ at imperfection resonances for a typical vertical orbit deviation $y_{co}^{rms}$ , without considering synchrotron oscillation. . . . .	19
3.2	Resonance strength $\epsilon_r$ of intrinsic resonances for a normalized emittance of $1\pi$ mm mrad and vertical betatron tune of $Q_y = 3.61$ for different superperiodicities $P$ . . . . .	20
4.1	The values of the mean polarisations $P$ determined with the EDDA polarimeter averaged over all the data at the beam energy $T_p$ . Only statistical errors are given in the table. . . . .	31
4.2	The normalisation factors $N$ obtained in a partial wave fit [30] to the current STT data. . . . .	44
5.1	Percentage contributions to the total systematic uncertainty at different proton beam energies $T_p$ . $E_1$ reflects the statistical and systematic effects in the determination of the Schottky $\eta$ parameter. $E_2$ arises from the rest gas effect (including direct measurement errors as well as possible instabilities). $E_3$ is a measure of the density instability through the 300 s cycle. These contributions have been added in quadrature with the accuracy of the stopping powers and the precision of the FD analysis to give the total percentage uncertainty in the last column. . . . .	55
5.2	Parameters of the fits of (Equation 5.12) to the differential cross sections measured in this experiment. In addition to the statistical errors shown, the second uncertainty in the value of $A$ in the second column represents the combined systematic effects summarised in Table 5.1. The corrected values of the forward cross section, $A(\text{Corr.})$ , were obtained using the SAID fit discussed in the text, the associated error bars being purely the systematic ones listed in Table 5.1. These values, which were not subjected to the SAID normalisation factors applied in Figure 5.11, may be compared with those of $A(\text{GK})$ , which were determined using the Grein and Kroll forward amplitudes [40]. . . . .	60
6.1	The values of the mean polarisations $P$ determined with the EDDA polarimeter averaged over all the data at the beam energy $T_p$ . . . . .	64

A.1	Laboratory angle ranges, corresponding to EDDA rings, in the coordinate system, associated with the detector. . . . .	79
B.1	Analysing power in $\vec{p}p$ elastic scattering at $T_p = 0.796$ GeV, calculated from STT data. . . . .	81
B.2	Analysing power in $\vec{p}p$ elastic scattering at $T_p = 1.6$ GeV, calculated from STT data. . . . .	82
B.3	Analysing power in $\vec{p}p$ elastic scattering at $T_p = 1.8$ GeV, calculated from STT data. . . . .	82
B.4	Analysing power in $\vec{p}p$ elastic scattering at $T_p = 1.965$ GeV, calculated from STT data. . . . .	83
B.5	Analysing power in $\vec{p}p$ elastic scattering at $T_p = 2.157$ GeV, calculated from STT data. . . . .	83
B.6	Analysing power in $\vec{p}p$ elastic scattering at $T_p = 2.368$ GeV, calculated from STT data. . . . .	84
B.7	Analysing power in $\vec{p}p$ elastic scattering at $T_p = 0.796$ GeV, calculated from FD data. . . . .	84
B.8	Analysing power in $\vec{p}p$ elastic scattering at $T_p = 1.6$ GeV, calculated from FD data. . . . .	85
B.9	Analysing power in $\vec{p}p$ elastic scattering at $T_p = 1.8$ GeV, calculated from FD data. . . . .	85
B.10	Analysing power in $\vec{p}p$ elastic scattering at $T_p = 1.965$ GeV, calculated from FD data. . . . .	86
B.11	Analysing power in $\vec{p}p$ elastic scattering at $T_p = 2.157$ GeV, calculated from FD data. . . . .	86
B.12	Analysing power in $\vec{p}p$ elastic scattering at $T_p = 2.368$ GeV, calculated from FD data. . . . .	87
C.1	Differential cross section in pp elastic scattering at $T_p = 1$ GeV. . .	90
C.2	Differential cross section in pp elastic scattering at $T_p = 1.6$ GeV. . .	91
C.3	Differential cross section in pp elastic scattering at $T_p = 1.8$ GeV. . .	92
C.4	Differential cross section in pp elastic scattering at $T_p = 2.0$ GeV . .	93
C.5	Differential cross section in pp elastic scattering at $T_p = 2.2$ GeV . .	94
C.6	Differential cross section in pp elastic scattering at $T_p = 2.4$ GeV . .	95
C.7	Differential cross section in pp elastic scattering at $T_p = 2.6$ GeV . .	96
C.8	Differential cross section in pp elastic scattering at $T_p = 2.8$ GeV . .	97
D.1	Analysing power in $\vec{p}d$ elastic scattering at $T_p = 0.796$ GeV. . . . .	99
D.2	Analysing power in $\vec{p}d$ elastic scattering at $T_p = 1.6$ GeV. . . . .	100
D.3	Analysing power in $\vec{p}d$ elastic scattering at $T_p = 1.8$ GeV. . . . .	100
D.4	Analysing power in $\vec{p}d$ elastic scattering at $T_p = 1.965$ GeV. . . . .	101
D.5	Analysing power in $\vec{p}d$ elastic scattering at $T_p = 2.157$ GeV. . . . .	101
D.6	Analysing power in $\vec{p}d$ elastic scattering at $T_p = 2.368$ GeV. . . . .	102
E.1	Analysing power in $\vec{p}n$ quasi-free elastic scattering at $T_p = 0.796$ GeV.	103
E.2	Analysing power in $\vec{p}n$ quasi-free elastic scattering at $T_p = 1.6$ GeV.	103

- E.3 Analysing power in  $\vec{p}n$  quasi-free elastic scattering at  $T_p = 1.8$  GeV. 104
- E.4 Analysing power in  $\vec{p}n$  quasi-free elastic scattering at  $T_p = 1.965$  GeV.104
- E.5 Analysing power in  $\vec{p}n$  quasi-free elastic scattering at  $T_p = 2157$  GeV.104
- E.6 Analysing power in  $\vec{p}n$  quasi-free elastic scattering at  $T_p = 2.368$ GeV.104



## Bibliography

- [1] M. Gell-Mann. A schematic model of baryons and mesons. *Physics Letters*, 8(3):214 – 215, 1964. ISSN 0031-9163. doi: [http://dx.doi.org/10.1016/S0031-9163\(64\)92001-3](http://dx.doi.org/10.1016/S0031-9163(64)92001-3). URL <http://www.sciencedirect.com/science/article/pii/S0031916364920013>.
- [2] G. Zweig. An SU(3) model for strong interaction symmetry and its breaking. Version 1. 1964.
- [3] E. D. Bloom, D. H. Coward, H. DeStaebler, J. Drees, G. Miller, L. W. Mo, R. E. Taylor, M. Breidenbach, J. I. Friedman, G. C. Hartmann, and H. W. Kendall. High-energy inelastic  $e - p$  scattering at  $6^\circ$  and  $10^\circ$ . *Phys. Rev. Lett.*, 23:930–934, Oct 1969. doi: 10.1103/PhysRevLett.23.930. URL <http://link.aps.org/doi/10.1103/PhysRevLett.23.930>.
- [4] M. Breidenbach, J. I. Friedman, H. W. Kendall, E. D. Bloom, D. H. Coward, H. DeStaebler, J. Drees, L. W. Mo, and R. E. Taylor. Observed behavior of highly inelastic electron-proton scattering. *Phys. Rev. Lett.*, 23:935–939, Oct 1969. doi: 10.1103/PhysRevLett.23.935. URL <http://link.aps.org/doi/10.1103/PhysRevLett.23.935>.
- [5] R. A. Arndt, W. J. Briscoe, I. I. Strakovsky, and R. L. Workman. Updated analysis of  $nn$  elastic scattering to 3 GeV. *Phys. Rev. C*, 76:025209, Aug 2007. doi: 10.1103/PhysRevC.76.025209. URL <http://link.aps.org/doi/10.1103/PhysRevC.76.025209>.
- [6] Richard A. Arndt, Igor I. Strakovsky, and Ron L. Workman. Nucleon-nucleon elastic scattering to 3 GeV. *Phys. Rev. C*, 62:034005, Aug 2000. doi:

- 10.1103/PhysRevC.62.034005. URL <http://link.aps.org/doi/10.1103/PhysRevC.62.034005>.
- [7] Scattering Analysis Interactive Dialin. URL <http://gwdac.phys.gwu.edu>.
- [8] D. Albers, J. Bisplinghoff, R. Bollmann, K. Büßer, P. Cloth, R. Daniel, O. Diehl, F. Dohrmann, H. P. Engelhardt, J. Ernst, P. D. Eversheim, M. Gasthuber, R. Gebel, J. Greiff, A. Groß, R. Groß-Hardt, S. Heider, A. Heine, F. Hinterberger, M. Igelbrink, R. Jahn, M. Jeske, U. Lahr, R. Langkau, J. Lindlein, R. Maier, R. Maschuw, T. Mayer-Kuckuk, F. Mosel, M. Müller, M. Münstermann, D. Prasuhn, H. Rohdjeß, D. Rosendaal, U. Roß, P. von Rossen, H. Scheid, N. Schirm, M. Schulz-Rojahn, F. Schwandt, V. Schwarz, W. Scobel, G. Sterzenbach, H. J. Trelle, A. Wellinghausen, W. Wiedmann, K. Woller, and R. Ziegler. Proton-proton elastic scattering excitation functions at intermediate energies. *Phys. Rev. Lett.*, 78: 1652–1655, Mar 1997. doi: 10.1103/PhysRevLett.78.1652. URL <http://link.aps.org/doi/10.1103/PhysRevLett.78.1652>.
- [9] M. Altmeier, F. Bauer, Bisplinghoff, et al. Excitation functions of the analyzing power in pp scattering from 0.45 to 2.5 GeV. *Phys. Rev. Lett.*, 85:1819–1822, Aug 2000. doi: 10.1103/PhysRevLett.85.1819. URL <http://link.aps.org/doi/10.1103/PhysRevLett.85.1819>.
- [10] M. Altmeier, F. Bauer, J. Bisplinghoff, K. Büßer, M. Busch, T. Colberg, L. Demirörs, H.P. Engelhardt, P.D. Eversheim, K.O. Eysler, O. Felden, R. Gebel, M. Glende, J. Greiff, F. Hinterberger, E. Jonas, H. Krause, T. Lindemann, J. Lindlein, B. Lorentz, R. Maier, R. Maschuw, A. Meinerzhagen, D. Prasuhn, H. Rohdjeß, D. Rosendaal, P. von Rossen, N. Schirm, V. Schwarz, W. Scobel, H.-J. Trelle, K. Ulbrich, E. Weise, A. Wellinghausen, and R. Ziegler. Excitation functions of the analyzing power in elastic proton-proton scattering from 0.45 to 2.5 GeV. *The European Physical Journal A - Hadrons and Nuclei*, 23(2):351–364, 2005. ISSN 1434-6001. doi: 10.1140/epja/i2004-10081-1. URL <http://dx.doi.org/10.1140/epja/i2004-10081-1>.

- [11] F. Bauer, J. Bisplinghoff, K. Büßer, M. Busch, T. Colberg, L. Demirörs, C. Dahl, P. D. Eversheim, O. Eysler, O. Felden, R. Gebel, J. Greiff, F. Hinterberger, E. Jonas, H. Krause, C. Lehmann, J. Lindlein, R. Maier, A. Meinerzhagen, C. Pauly, D. Prasuhn, H. Rohdjeß, D. Rosendaal, P. von Rossen, N. Schirm, W. Scobel, K. Ulbrich, E. Weise, T. Wolf, and R. Ziegler. Measurement of spin-correlation parameters  $A_{NN}$ ,  $A_{SS}$ , and  $A_{SL}$  at 2.1 GeV in proton-proton elastic scattering. *Phys. Rev. Lett.*, 90:142301, Apr 2003. doi: 10.1103/PhysRevLett.90.142301. URL <http://link.aps.org/doi/10.1103/PhysRevLett.90.142301>.
- [12] J. Bystricky, F. Lehar, and P. Winternitz. Formalism of nucleon-nucleon elastic scattering experiments. *Journal de Physique*, 39(1):1–32, 1978. doi: 10.1051/jphys:019780039010100. URL <https://hal.archives-ouvertes.fr/jpa-00208735>.
- [13] Catherine Lechanoine-LeLuc and Francois Lehar. Nucleon-nucleon elastic scattering and total cross sections. *Rev. Mod. Phys.*, 65:47–86, Jan 1993. doi: 10.1103/RevModPhys.65.47. URL <http://link.aps.org/doi/10.1103/RevModPhys.65.47>.
- [14] Hans Paetz gen. Schieck. *Nuclear Reactions. An Introduction*, volume 882. Springer-Verlag Berlin Heidelberg, 2014. doi: 10.1007/978-3-642-53986-2. URL <http://www.springer.com/gp/book/9783642539855>.
- [15] R. Maier. Cooler synchrotron COSY — performance and perspectives. *Nuclear Instruments and Methods in Physics Research Section A: Accelerators, Spectrometers, Detectors and Associated Equipment*, 390(1–2):1 – 8, 1997. ISSN 0168-9002. doi: [http://dx.doi.org/10.1016/S0168-9002\(97\)00324-0](http://dx.doi.org/10.1016/S0168-9002(97)00324-0). URL <http://www.sciencedirect.com/science/article/pii/S0168900297003240>.
- [16] P. D. Eversheim, M. Altmeier, O. Felden, R. Gebel, M. Krekel, M. Schak, W. Kretschmer, A. Glombik, K. Mümmler, P. Nebert, G. Suft, R. Weidmann, H. Paetz gen. Schieck, M. Eggert, S. Lemaître, H. Patberg, R. Reckenfelderbäumer, and C. Schneider. Status of the polarized source for the cooler

- synchrotron cosy julich. *AIP Conference Proceedings*, 293(1):92–96, 1993. doi: <http://dx.doi.org/10.1063/1.45153>. URL <http://scitation.aip.org/content/aip/proceeding/aipcp/10.1063/1.45153>.
- [17] E. Weise. *Anregungsfunktionen der Analysierstärke der elastischen Proton-Proton-Streuung*. PhD thesis, University of Bonn, 2000.
- [18] S Barsov, U Bechstedt, W Bothe, N Bongers, G Borchert, W Borgs, W Bräutigam, M Büscher, W Cassing, V Chernyshev, B Chiladze, J Dietrich, M Drochner, S Dymov, W Erven, R Esser, A Franzen, Ye Golubeva, D Gotta, T Grande, D Grzonka, A Hardt, M Hartmann, V Hejny, L.v Horn, L Jarczyk, H Junghans, A Kacharava, B Kamys, A Khoukaz, T Kirchner, F Klehr, W Klein, H.R Koch, V.I Komarov, L Kondratyuk, V Koptev, S Kopyto, R Krause, P Kravtsov, V Kruglov, P Kulesa, A Kulikov, N Lang, N Langenhagen, A Leppes, J Ley, R Maier, S Martin, G Macharashvili, S Merzliakov, K Meyer, S Mikirtychians, H Müller, P Munhofen, A Mussgiller, M Nekipelov, V Nelyubin, M Nioradze, H Ohm, A Petrus, D Prasuhn, B Prietzsch, H.J Probst, K Pysz, F Rathmann, B Rimarzig, Z Rudy, R Santo, H Paetz gen. Schieck, R Schleichert, A Schneider, Chr Schneider, H Schneider, U Schwarz, H Seyfarth, A Sibirtsev, U Sieling, K Sistemich, A Selikov, H Stechemesser, H.J Stein, A Strzalkowski, K.-H Watzlawik, P Wüstner, S Yashenko, B Zalikhanov, N Zhuravlev, K Zwill, I Zychor, O.W B. Schult, and H Ströher. ANKE, a new facility for medium energy hadron physics at COSY-Jülich. *Nuclear Instruments and Methods in Physics Research Section A: Accelerators, Spectrometers, Detectors and Associated Equipment*, 462(3):364 – 381, 2001. ISSN 0168-9002. doi: [http://dx.doi.org/10.1016/S0168-9002\(00\)01147-5](http://dx.doi.org/10.1016/S0168-9002(00)01147-5). URL <http://www.sciencedirect.com/science/article/pii/S0168900200011475>.
- [19] A. Khoukaz, T. Lister, C. Quentmeier, R. Santo, and C. Thomas. Systematic studies on hydrogen cluster beam production. *The European Physical Journal D - Atomic, Molecular, Optical and Plasma Physics*, 5(2):275–281, 1999. ISSN

- 1434-6060. doi: 10.1007/PL00021595. URL <http://dx.doi.org/10.1007/PL00021595>.
- [20] S. Dymov, W. Erven, A. Kacharava, R. Koch, V. Komarov, A. Kulikov, V. Kurbatov, G. Macharashvili, H. Ohm, A. Ptrus, F. Rathmann, H. Seyfarth, H. Ströher, S. Yaschenko, B. Zalikhanov, and K. Zvoll. The forward detector of the ANKE spectrometer. Tracking system and its use in data analysis. *Particles and Nuclei, Letters*, 2:40, 2004. URL [http://wwinfo.jinr.ru/publish/Pepan\\_letters/panl\\_2\\_2004/2\\_2004\\_05\\_dym.pdf](http://wwinfo.jinr.ru/publish/Pepan_letters/panl_2_2004/2_2004_05_dym.pdf).
- [21] S. Dymov. *Investigation of the deuteron breakup by protons of 0.6-0.9 GeV with emission of a forward proton pair*. PhD thesis, JINR, 2007. URL [http://collaborations.fz-juelich.de/ikp/anke/theses/S.Dymov\\_PhD.pdf](http://collaborations.fz-juelich.de/ikp/anke/theses/S.Dymov_PhD.pdf).
- [22] R. Schleichert, T. Krings, S. Merzliakov, A. Mussgiller, and D. Protic. A self-triggering silicon-tracking telescope for spectator proton detection. *Nuclear Science, IEEE Transactions on*, 50(3):301–306, June 2003. ISSN 0018-9499. doi: 10.1109/TNS.2003.812431.
- [23] G. Macharashvili. The software development for the silicon detector data analysis at ANKE-COSY. Technical Note. URL <http://apps.fz-juelich.de/pax/paxwiki/images/6/6c/TechNote15.pdf>.
- [24] G. Macharashvili. A neural network concept for event reconstruction at ANKE. Technical Note, 2000.
- [25] S. Yaschenko, S. Dymov, A. Kacharava, V. Komarov, G. Macharashvili, F. Rathmann, S. Barsov, R. Gebel, M. Hartmann, A. Khoukaz, P. Kulesa, A. Kulikov, V. Kurbatov, N. Lang, I. Lehmann, B. Lorentz, T. Mersmann, S. Merzliakov, S. Mikirtytchians, A. Mussgiller, M. Nioradze, H. Ohm, D. Prasuhn, R. Schleichert, H. Seyfarth, E. Steffens, H. J. Stein, H. Ströher, Yu. Uzikov, B. Zalikhanov, and N. Zhuravlev. Measurement of the analyzing power in  $\vec{p} d \rightarrow (pp)n$  with a fast forward  $^1S_0$  proton pair. *Phys. Rev. Lett.*, 94:072304, Feb 2005. doi: 10.1103/PhysRevLett.94.072304. URL <http://link.aps.org/doi/10.1103/PhysRevLett.94.072304>.

- [26] M. W. McNaughton, P. R. Bevington, H. B. Willard, E. Winkelmann, E. P. Chamberlin, F. H. Cverna, N. S. P. King, and H. Willmes. Polarization analyzing power  $A(\theta)$  in pp elastic scattering at 796 MeV. *Phys. Rev. C*, 23:1128–1133, Mar 1981. doi: 10.1103/PhysRevC.23.1128. URL <http://link.aps.org/doi/10.1103/PhysRevC.23.1128>.
- [27] F. Irom, G. J. Igo, J. B. McClelland, and C. A. Whitten. Elastic  $p - p$  scattering at 796 MeV in the coulomb-nuclear interference region. *Phys. Rev. C*, 25:373–386, Jan 1982. doi: 10.1103/PhysRevC.25.373. URL <http://link.aps.org/doi/10.1103/PhysRevC.25.373>.
- [28] P. R. Bevington, M. W. McNaughton, H. B. Willard, H. W. Baer, E. Winkelmann, F. Cverna, E. P. Chamberlin, N. S. P. King, R. R. Stevens, H. Wilmes, and M. A. Schardt. Polarization analyzing power  $A_y(\theta)$  in pp elastic scattering at 643, 787, and 796 MeV. *Phys. Rev. Lett.*, 41:384–387, Aug 1978. doi: 10.1103/PhysRevLett.41.384. URL <http://link.aps.org/doi/10.1103/PhysRevLett.41.384>.
- [29] C.E. Allgower, J. Ball, M. Beddo, Y. Bedfer, A. Boutefnouchet, J. Bystricky, P.-A. Chamouard, Ph. Demierre, J.-M. Fontaine, V. Ghazikhanian, D. Grosnick, R. Hess, Z. Janout, Z.F. Janout, V.A. Kalinnikov, T.E. Kasprzyk, B.A. Khachaturov, R. Kunne, F. Lehar, A. de Lesquen, D. Lopiano, V.N. Matafonov, I.L. Oisarev, A.A. Popov, A.N. Prokofiev, D. Rapin, J.-L. Sans, H.M. Spinka, A. Teglia, Yu.A. Usov, V.V. Vikhrov, B. Vuaridel, C.A. Whitten, and A.A. Zhdanov. The pp elastic scattering analyzing power measured with the polarized beam and the unpolarized target between 1.98 and 2.80 GeV. *Nuclear Physics A*, 637(2):231 – 242, 1998. ISSN 0375-9474. doi: [http://dx.doi.org/10.1016/S0375-9474\(98\)00216-4](http://dx.doi.org/10.1016/S0375-9474(98)00216-4). URL <http://www.sciencedirect.com/science/article/pii/S0375947498002164>.
- [30] Communication with R. Workman and I. Strokovsky. (The paper with the modified SAID solution is being prepared), 2015.

- [31] H. J. Stein, M. Hartmann, I. Keshelashvili, Y. Maeda, C. Wilkin, S. Dymov, A. Kacharava, A. Khoukaz, B. Lorentz, R. Maier, T. Mersmann, S. Mikirtychians, D. Prasuhn, R. Stassen, H. Stockhorst, H. Ströher, Yu. Valdau, and P. Wüstner. Determination of target thickness and luminosity from beam energy losses. *Phys. Rev. ST Accel. Beams*, 11:052801, May 2008. doi: 10.1103/PhysRevSTAB.11.052801. URL <http://link.aps.org/doi/10.1103/PhysRevSTAB.11.052801>.
- [32] Kirsten Zapfe, W. Brückner, H.-G. Gaul, M. Grieser, M.T. Lin, Z. Moroz, B. Povh, M. Rall, B. Stechert, E. Steffens, J. Stenger, F. Stock, J. Tonhäuser, Ch. Montag, F. Rathmann, D. Fick, B. Braun, G. Graw, and W. Haeberli. Detailed studies of a high-density polarized hydrogen gas target for storage rings. *Nuclear Instruments and Methods in Physics Research Section A: Accelerators, Spectrometers, Detectors and Associated Equipment*, 368(2):293 – 306, 1996. ISSN 0168-9002. doi: [http://dx.doi.org/10.1016/0168-9002\(95\)00608-7](http://dx.doi.org/10.1016/0168-9002(95)00608-7). URL <http://www.sciencedirect.com/science/article/pii/0168900295006087>.
- [33] NIST-PML database. URL <http://nist.gov/pml/data/star/>.
- [34] W. Schottky. Zur theorie des elektronenrauschens in mehrgitterröhren. *Annalen der Physik*, 424(1-2):195–204, 1938. ISSN 1521-3889. doi: 10.1002/andp.19384240122. URL <http://dx.doi.org/10.1002/andp.19384240122>.
- [35] A.V. Dobrovolsky, A.V. Khanzadeev, G.A. Korolev, E.M. Maev, V.I. Medvedev, G.L. Sokolov, N.K. Terentyev, Y. Terrien, G.N. Velichko, A.A. Vorobyov, and Yu.K. Zalite. Small angle pp scattering at energies from 650 to 1000 MeV. *Nuclear Physics B*, 214(1):1 – 20, 1983. ISSN 0550-3213. doi: [http://dx.doi.org/10.1016/0550-3213\(83\)90163-3](http://dx.doi.org/10.1016/0550-3213(83)90163-3). URL <http://www.sciencedirect.com/science/article/pii/0550321383901633>.
- [36] B.H. Silverman, J.C. Lugol, J. Saudinos, Y. Terrien, F. Wellers, A.V. Dobrovolsky, A.V. Khanzadeev, G.A. Korolev, G.E. Petrov, E.M. Spiridenkov, and A.A. Vorobyov. Differential cross sections and analyzing powers for small

- angle neutron-proton elastic scattering between 378 and 1135 MeV. *Nuclear Physics A*, 499(4):763 – 788, 1989. ISSN 0375-9474. doi: [http://dx.doi.org/10.1016/0375-9474\(89\)90062-6](http://dx.doi.org/10.1016/0375-9474(89)90062-6). URL <http://www.sciencedirect.com/science/article/pii/0375947489900626>.
- [37] A. V. Dobrovolsky, A. V. Khanzadeev, G. A. Korolev, G. N. Velichko, A. A. Vorobyov, J. Saudinos, B. H. Silverman, Y. Terrien, and F. Wellers. Experimental data on elastic pp, np, pd, and p $\alpha$  forward scattering at intermediate energies. Technical Report LENINGRAD-INST-YAD-FIZ-1454. LIYF-1454, Akad. Nauk St. Petersburg. Inst. Yarn. Fiz., St. Petersburg, Nov 1988. URL <https://cds.cern.ch/record/195992>.
- [38] I. Ambats, D. S. Ayres, R. Diebold, A. F. Greene, S. L. Kramer, A. Lesnik, D. R. Rust, C. E. W. Ward, A. B. Wicklund, and D. D. Yovanovitch. Systematic study of  $\pi^\pm p$ ,  $K^\pm p$ , pp, and  $\bar{p}p$  forward elastic scattering from 3 to 6 GeV/c. *Phys. Rev. D*, 9:1179–1209, Mar 1974. doi: 10.1103/PhysRevD.9.1179. URL <http://link.aps.org/doi/10.1103/PhysRevD.9.1179>.
- [39] A precision measurement of pp elastic scattering cross-sections at intermediate energies. *The European Physical Journal A - Hadrons and Nuclei*, 22(1):125–148, 2004. ISSN 1434-6001. doi: 10.1140/epja/i2004-10011-3. URL <http://dx.doi.org/10.1140/epja/i2004-10011-3>.
- [40] W. Grein and P. Kroll. Amplitude analysis of forward nucleon-nucleon scattering. *Nuclear Physics A*, 377(2):505 – 517, 1982. ISSN 0375-9474. doi: [http://dx.doi.org/10.1016/0375-9474\(82\)90052-5](http://dx.doi.org/10.1016/0375-9474(82)90052-5). URL <http://www.sciencedirect.com/science/article/pii/0375947482900525>.
- [41] Richard A. Arndt, L. David Roper, Ronald A. Bryan, Robert B. Clark, Bruce J. VerWest, and Peter Signell. Nucleon-nucleon partial-wave analysis to 1 GeV. *Phys. Rev. D*, 28:97–122, Jul 1983. doi: 10.1103/PhysRevD.28.97. URL <http://link.aps.org/doi/10.1103/PhysRevD.28.97>.
- [42] C. Lechanoine, F. Lehar, F. Perrot, and P. Winternitz. Polarization phenomena in nucleon-nucleon forward scattering. *Il Nuovo Cimento A Series*

- 11, 56(2):201–228, 1980. ISSN 0369-3546. doi: 10.1007/BF02730164. URL <http://dx.doi.org/10.1007/BF02730164>.
- [43] F. Irom, G. J. Igo, J. B. McClelland, C. A. Whitten, and M. Bleszynski. Measurements of small angle elastic  $\vec{p}$ -d scattering at 796 MeV using a recoil method. *Phys. Rev. C*, 28:2380–2385, Dec 1983. doi: 10.1103/PhysRevC.28.2380. URL <http://link.aps.org/doi/10.1103/PhysRevC.28.2380>.
- [44] M. L. Barlett, G. W. Hoffmann, J. A. McGill, B. Hoistad, L. Ray, R. W. Ferguson, E. C. Milner, J. A. Marshall, J. F. Amann, B. E. Bonner, J. B. McClelland, G. S. Blanpied, and R. A. Arndt. Forward-angle elastic and quasielastic proton-nucleon cross sections and analyzing powers at 0.8 GeV. *Phys. Rev. C*, 27:682–696, Feb 1983. doi: 10.1103/PhysRevC.27.682. URL <http://link.aps.org/doi/10.1103/PhysRevC.27.682>.
- [45] J. Ball, Ph. Chesny, M. Combet, J.M. Fontaine, C.D. Lac, J.L. Sans, J. Bystricky, F. Lehar, A. de Lesquen, M. de Mali, F. Perrot-Kunne, L. van Rossum, A. Ahmidouch, P. Bach, Ph. Demierre, G. Gaillard, R. Hess, R. Kunne, D. Rapin, Ph. Sormani, J.P. Goudour, R. Binz, A. Klett, E. Rössle, H. Schmitt, D. Lopiano, and H. Spinka. Angular dependence of analyzing power in np elastic scattering between 0.312 and 1.10 GeV. *Nuclear Physics A*, 559(4):489 – 510, 1993. ISSN 0375-9474. doi: [http://dx.doi.org/10.1016/0375-9474\(93\)90257-X](http://dx.doi.org/10.1016/0375-9474(93)90257-X). URL <http://www.sciencedirect.com/science/article/pii/037594749390257X>.
- [46] G. Glass, T. S. Bhatia, J. C. Hiebert, R. A. Kenefick, S. Nath, L. C. Northcliffe, K. F. Johnson, H. Spinka, R. Stanek, M. W. Rawool, J. A. Faucett, R. H. Jeppesen, G. E. Tripard, and C. R. Newsom. Analyzing power measurement for forward angle  $n - p$  scattering at 790 MeV. *Phys. Rev. C*, 41:2732–2736, Jun 1990. doi: 10.1103/PhysRevC.41.2732. URL <http://link.aps.org/doi/10.1103/PhysRevC.41.2732>.
- [47] G. Glass, T. S. Bhatia, J. C. Hiebert, R. A. Kenefick, S. Nath, L. C. Northcliffe, W. B. Tippens, and J. E. Simmons. Forward angle analyzing power

- in  $p \rightarrow n$  and  $p \rightarrow p$  quasifree scattering at 643 and 797 mev. *Phys. Rev. C*, 47:1369–1375, Apr 1993. doi: 10.1103/PhysRevC.47.1369. URL <http://link.aps.org/doi/10.1103/PhysRevC.47.1369>.
- [48] R. Diebold, D. S. Ayres, S. L. Kramer, A. J. Pawlicki, and A. B. Wicklund. Measurement of the proton-neutron elastic-scattering polarization from 2 to 6 GeV/c. *Phys. Rev. Lett.*, 35:632–635, Sep 1975. doi: 10.1103/PhysRevLett.35.632. URL <http://link.aps.org/doi/10.1103/PhysRevLett.35.632>.
- [49] Y. Makdisi, M. L. Marshak, B. Mossberg, E. A. Peterson, K. Ruddick, J. B. Roberts, and R. D. Klem. Analyzing power in large-angle proton-neutron elastic scattering. *Phys. Rev. Lett.*, 45:1529–1533, Nov 1980. doi: 10.1103/PhysRevLett.45.1529. URL <http://link.aps.org/doi/10.1103/PhysRevLett.45.1529>.
- [50] Z. Bagdasarian, D. Chiladze, S. Dymov, A. Kacharava, G. Macharashvili, S. Barsov, R. Gebel, B. Gou, M. Hartmann, I. Keshelashvili, A. Khoukaz, P. Kulesa, A. Kulikov, A. Lehrach, N. Lomidze, B. Lorentz, R. Maier, D. Mchedlishvili, S. Merzliakov, S. Mikirtychyants, M. Nioradze, H. Ohm, M. Papenbrock, D. Prasuhn, F. Rathmann, V. Serdyuk, V. Shmakova, R. Stassen, H. Stockhorst, I.I. Strakovsky, H. Ströher, M. Tabidze, A. Täschner, S. Trusov, D. Tsirkov, Yu. Uzikov, Yu. Valdau, C. Wilkin, and R.L. Workman. Measurement of the analysing power in proton–proton elastic scattering at small angles. *Physics Letters B*, 739:152 – 156, 2014. ISSN 0370-2693. doi: <http://dx.doi.org/10.1016/j.physletb.2014.10.054>. URL <http://www.sciencedirect.com/science/article/pii/S0370269314007874>.
- [51] G. G. Ohlsen and Jr. P. W. Keaton. Techniques for measurement of spin 1/2 and spin 1 polarization analyzing tensors. *Nuclear Instruments and Methods*, 109(8):41 –59, January 1973. URL <http://www.sciencedirect.com/science/article/pii/0029554X73904503>.
- [52] A. Lehrach, U. Bechstedt, J. Dietrich, R. Gebel, B. Lorentz, et al. Acceleration of polarized protons and deuterons at COSY. *AIP Conf.Proc.*, 675:153–165, 2003. doi: 10.1063/1.1607127.

- [53] J. H. Parry, N. E. Booth, G. Conforto, R. J. Esterling, J. Scheid, D. J. Sherden, and A. Yokosawa. Measurements of the polarization in proton-proton elastic scattering from 2.50 to 5.15 GeV/ $c$ . *Phys. Rev. D*, 8:45–63, Jul 1973. doi: 10.1103/PhysRevD.8.45. URL <http://link.aps.org/doi/10.1103/PhysRevD.8.45>.
- [54] A.V. Dobrovolsky, A.V. Khanzadeev, G.A. Korolev, G.N. Velichko, A.A. Vorobyov, J. Saudinos, B.H. Silverman, Y. Terrien, and F. Wellers. Experimental data on elastic pp, np, pd, and p $\alpha$  forward scattering at intermediate energies. report LNPI-1454, 1988.
- [55] V. S. Morozov, A. D. Krisch, M. A. Leonova, R. S. Raymond, D. W. Sivers, V. K. Wong, R. Gebel, A. Lehrach, B. Lorentz, R. Maier, D. Prasuhn, A. Schnase, H. Stockhorst, D. Eversheim, F. Hinterberger, H. Rohd-jeß, K. Ulbrich, and K. Yonehara. Spin manipulating stored 1.85 GeV/ $c$  vector and tensor polarized spin-1 bosons. *Phys. Rev. ST Accel. Beams*, 8:061001, Jun 2005. doi: 10.1103/PhysRevSTAB.8.061001. URL <http://link.aps.org/doi/10.1103/PhysRevSTAB.8.061001>.
- [56] The Standard Model of Elementary Particles. URL [https://en.wikipedia.org/wiki/Standard\\_Model#/media/File:Standard\\_Model\\_of\\_Elementary\\_Particles.svg](https://en.wikipedia.org/wiki/Standard_Model#/media/File:Standard_Model_of_Elementary_Particles.svg).
- [57] G. Macharashvili.  $A_y$  measurement in  $pp$  elastic scattering. Systematic uncertainties. Technical Note, 2013.
- [58] S. Dymov.  $A_y$  in  $pp$  measured with forward detector. Technical Note, 2014.
- [59] S. Dymov. The proton-proton elastic scattering count rates from the ANKE Forward Detector: Systematic uncertainties.



## *Erklärung*

Ich versichere, dass ich die von mir vorgelegte Dissertation selbständig angefertigt, die benutzten Quellen und Hilfsmittel vollständig angegeben und die Stellen der Arbeit – einschliesslich Tabellen, Karten und Abbildungen –, die anderen Werken im Wortlaut oder dem Sinn nach entnommen sind, in jedem Einzelfall als Entlehnung kenntlich gemacht habe; dass diese Dissertation abgesehen von Tiflis Universität noch keiner anderen Fakultät oder Universität zur Prüfung vorgelegen hat; dass sie – abgesehen von unten angegebenen Teilpublikationen – noch nicht veröffentlicht worden ist, sowie, dass ich eine solche Veröffentlichung vor Abschluss des Promotionsverfahrens nicht vornehmen werde. Die Bestimmungen der Promotionsordnung sind mir bekannt. Die von mir vorgelegte Dissertation ist von Herr Prof. Dr. Hans Ströher und Dr. Nodar Lomidze betreut worden.

## *Teilpublikationen*



# Lebenslauf

## Persönliche Daten

---

Name:	Zara Bagdasarian
Geburtsdatum:	04.10.1989
Geburstort:	Tiflis, Georgien
Staatsangehörigkeit:	georgisch
Familienstand:	verheiratet

## Studium

---

Oktober 2010 - Juli 2012	Master der Physik der Staatlichen Iwane-Dschawachischwili-Universität Tiflis, Georgien Gesamtnote: "mit Auszeichnung"
--------------------------	---

Master Thesis

Oktober 2006 - Juli 2010	Bachelor der Physik der Staatlichen Iwane-Dschawachischwili-Universität Tiflis, Georgien Gesamtnote: "mit Auszeichnung"
--------------------------	---

## Schulbildung

---

September 1996 - Juni 2006	Schule #9, Tiflis, Georgien Gesamtnote: "mit Auszeichnung"
----------------------------	---